To the Graduate Council:

I am submitting herewith a thesis written by Yinghui Lu entitled "Instantaneous Torque Control of Switched Reluctance Motors." I have examined the final paper copy of this thesis for form and content and recommend that it be accepted in partial fulfillment of the requirements for the degree of Master of Science, with a major in Electrical Engineering.

John Chiasson

John N. Chiasson, Major Professor

We have read this thesis
and recommend its acceptance:

Leon M Tolbert

Leon M. Tolbert

Jack S. Lawler

Accepted for the Council:

Vice Provost and
Dean of Graduate Studies

INSTANTANEOUS TORQUE CONTROL OF SWITCHED RELUCTANCE MOTORS

A Thesis
Presented for the
Master of Science
Degree
The University of Tennessee, Knoxville

Yinghui Lu
August 2002

Abstract

The Switched Reluctance (SR) motor is an old member of the electric machine family. Its simple structure, ruggedness, and inexpensive manufacturability make them attractive for industrial applications. However, these merits are overshadowed by its inherently high torque ripple, acoustic noise, and difficulty to control [1]. This thesis investigated the implementation of an instantaneous torque control method reported in the literature. The simulation and experimental results illustrate the capability of SR motors being used in servo systems. Based on experimental data, the advantages of this control method and its disadvantages in practical implementation were studied.

Table of Contents

List of Figures

Chapter 1 Introduction

1.1 Introduction to Switched Reluctance Motors

The Switched Reluctance (SR) motor is an old member of the electric machine family. The first SR motor can be traced back to the early 19th century [2]. The main advantages of SR motors are their simple structure, ruggedness, and that they are relatively inexpensive to manufacture. However, the primary disadvantages, such as the torque ripple, acoustic noise, and the difficulty in controlling, prevent it from being accepted by the industry extensively.

During the past two decades, researches have been done to reduce the torque ripple and acoustic noise. Several rather complicated control methods, motor designs, and power electronics inverter topologies have been proposed which now make the SR motor a possible candidate for many drive applications, such as servo drives and traction drives of Hybrid Electric Vehicles (HEVs) [3] [4] [5] [6] [7] [8].

This thesis investigates the implementation of advanced control methods for the SR motor. A real-time control platform was set up and a trajectory tracking controller for a 3-phase 12/8 SR motor was implemented.

1.1.1 Basic Structure

The basic structure of a Switched Reluctance (SR) motor is shown in Figure 1 which is an illustrative cross sectional view of a three phase 6/4 SR motor. As shown in the figure, the SR motor has salient poles on both the rotor and the stator, making it a double salient machine. The machine has 4 rotor poles and 6 stator poles, which is referred to as a 6/4 SR motor. Each stator pole has a concentrated coil wound on it (not shown in the figure). Two coils on the opposite stator poles are connected in serial or parallel, making one stator phase. There are no windings on the rotor, nor does the rotor have any permanent magnetic material.

The stator and rotor are usually both made of laminated silicon steel in order to diminish eddy currents. Although the generally used Steinmetz equation for core loss calculation under sinusoidal current excitation is not strictly applicable to SR motors (due to the non-sinusoidal flux waveforms in the SR motor), it is can be used to indicate the nature of the core loss of SR motors [2]. The Steinmetz equation is given by

$$P_{Fe} = C_h f B_{pk}^{a+bB_{pk}} + C_e f^2 B_{pk}^2 \tag{1.1}$$

where P_{Fe} stands for the core loss, C_h and C_e are the coefficients of hysteresis and eddy current loss, a and b are empirically determined constants, f is the current excitation frequency, and B_{pk} is the peak value of the flux density.

Equation 1.1 shows that, like induction motors, the dominant core loss of the SR motor at high frequency is the eddy current loss. Therefore, a thinner lamination is desirable for high speed design.

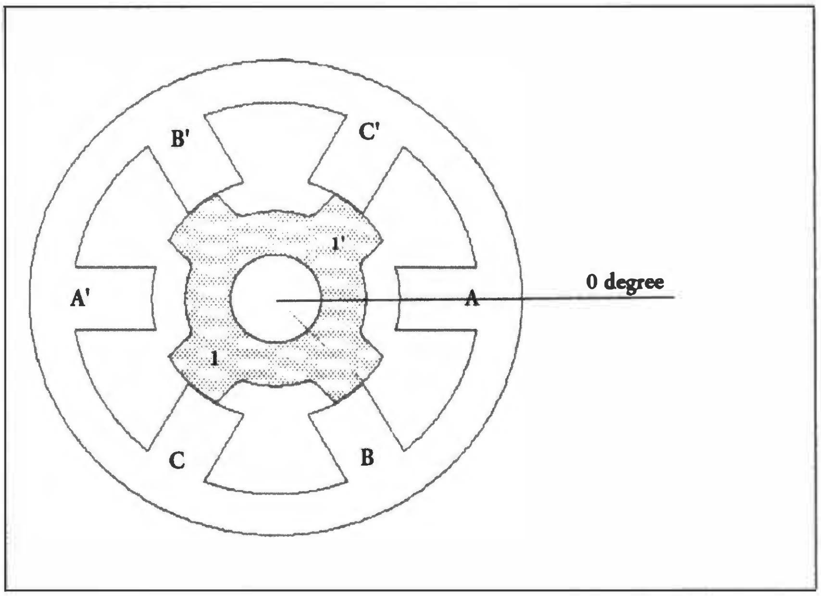

Figure 1. Cross section of a 6/4 SR motor (Phase A is at Unaligned Position) Courtesy Magna Physics Publishing

In Figure 1, when the stator phase $C - C'$ is excited, the phase current magnetizes the stator poles creating a magnetic field. This magnetic field magnetizes the rotor pole pair $1 - 1,'$ attracting it to rotate counter-clockwise towards the excited stator poles of phase$C - C'$. During the movement, the reluctance of the closed flux path decreases and reaches its minimum value when the rotor pole is aligned to the stator pole, i.e., the axis of the rotor pole $1 - 1'$ is aligned to the stator pole axis $C - C'$. The change of reluctance during the rotation is why the term *variable reluctance* motor is also used for switched reluctance motors.

If three phases are excited in sequence, that is, phase $C - C'$, then $A - A'$, then $B - B'$, then $C - C'$, then the rotor will rotate in step. The step angle is given by

$$\theta_s = \frac{2\pi}{qn_R}$$

where q is the number of phases and n_R is the number of rotor poles. For the 6/4 SR motor shown in Figure 1, $\theta_s = 30°$.

Figure 2 illustrates a 6/4 SR motor with a rotor tooth pair aligned with stator phase $A - A'$. In Figure 2, the rotor is aligned with stator phase $A - A'$ and this is said to be at the *aligned* position for stator phase $A - A'$. In contrast, with respect to phase $A - A'$, the rotor is said to be at the *unaligned* position in Figure 1, as the interpolar axis of the rotor is aligned with it. The aligned position is a stable equilibrium point in that the phase current can not produce any torque at this position,but a small deviation of the rotor away from this point will produce a torque to push the rotor back. In contrast, the unaligned position is an unstable equilibrium point because any small displacement of the rotor away from that point results in the rotor moving away.

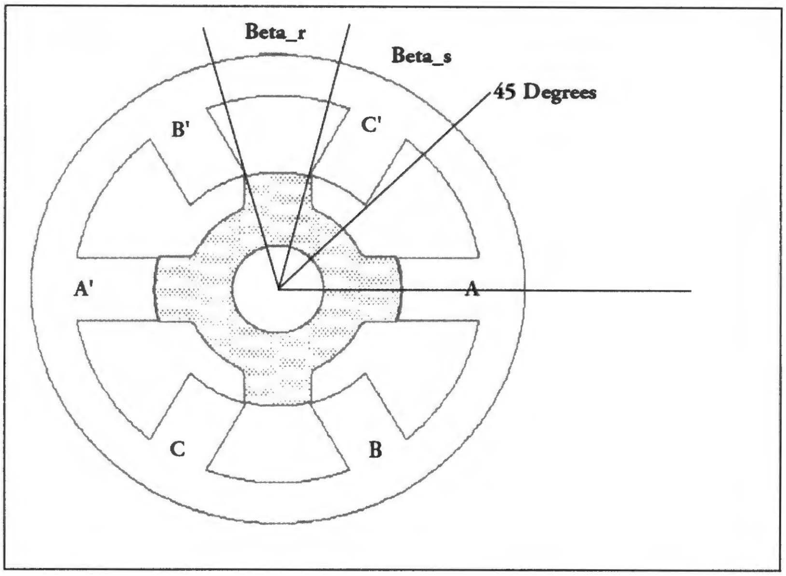

Figure 2. Cross section of a 6/4 SR motor (Phase A is at Aligned Position) Courtesy Magna Physics Publishing

Throughout this paper, unaligned position for phase A is defined to be $\theta = 0°$ and counterclockwise rotation is defined to be the positive rotating direction.

1.1.2 Torque Ripple and Its Reduction Through Control Approaches

Torque ripple is the main disadvantage of SR motors and limits their applications. The doubly salient structure of the machine introduced in the previous section is the inherent reason for the torque ripple. Because the torque production mechanism of SR motors is basically successive excitations of each stator phase, the doubly salient structure inevitably results in the torque pulsations between two successive excitations.

Although much work has been done in the motor design to reduce the torque ripple, advanced control methods are needed to reduce torque ripple.

A general trajectory tracking control block diagram is shown in Figure 3. The position and speed feedback control determines the reference torque, T_ref. The mapping between the reference torque T_ref and the reference phase currents, i_ref, is represented by the *Reduced Torque Ripple Controller* block, in which a torque ripple reduction method is implemented. The generated phase reference currents are fed into the current controller which regulates the actual phase currents through a PWM controller. The *Reduced Torque Ripple Controller* is the topic investigated in this thesis. Very recently, in [9], several promising control methods are presented. This thesis discusses and implements one of these control methods, specifically, that given by Taylor in [10].

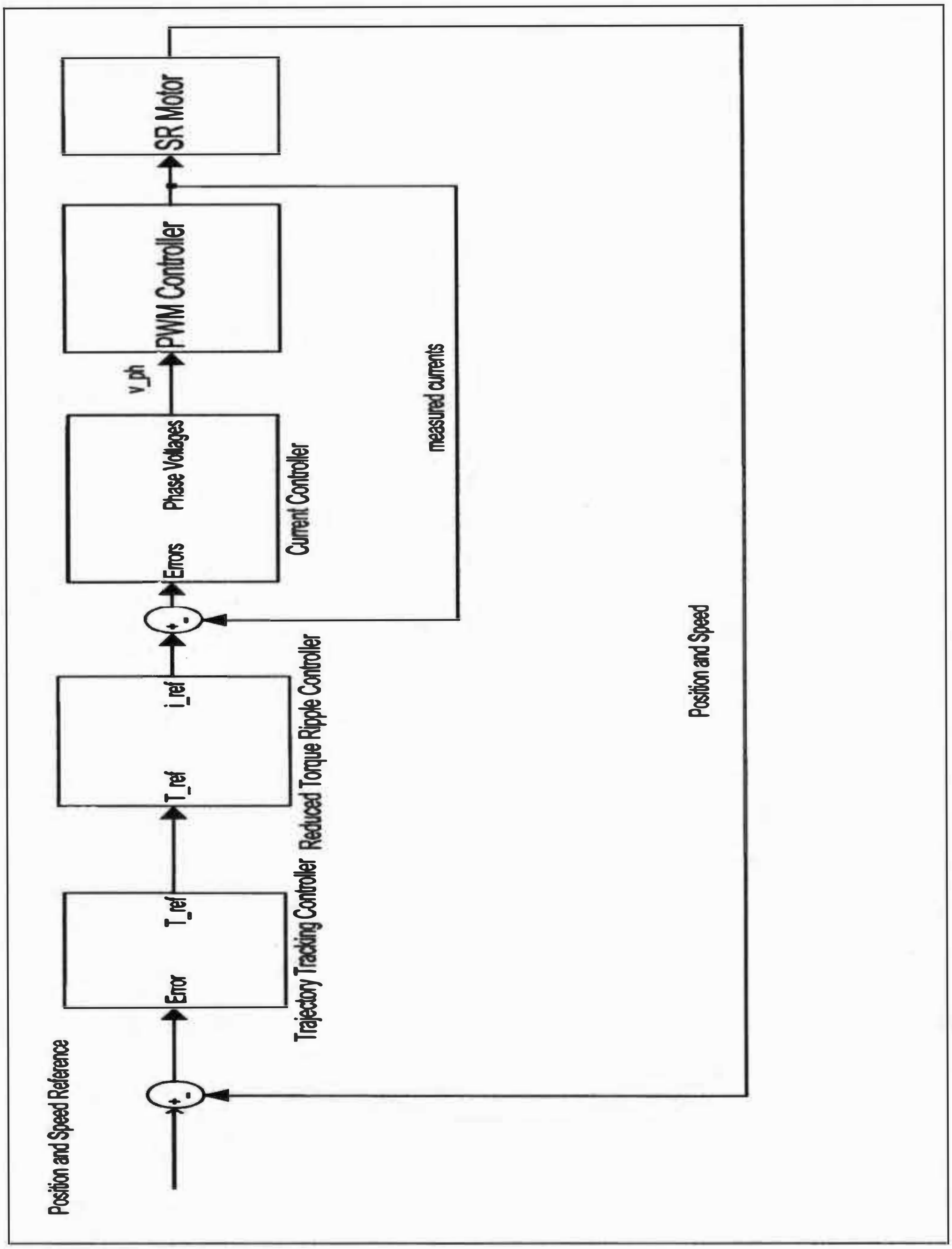

Figure 3. Trajectory tracking control blocks of the SR motor

1.2 Outline of Thesis

Chapter 2 discusses the basic operation and the mathematical model of SR motors. Properties, such as its magnetic field, energy conversion, and the phase currents of SR motors are described and demonstrated by simulations.

Chapter 3 introduces traditional variable speed control methods and advanced instantaneous torque control methods. The reduced torque ripple controller presented by Taylor in 1992 in [10] and its implementation is introduced in detail in this chapter.

In Chapter 4, the real-time control platform set up for the implementation of the SR motor controller is presented. On that control platform, a 3-phase 12/8 SR motor was tested to obtain the torque profile and motor parameters.

In Chapter 5, a SR motor model and an instantaneous torque controller based on the control method [10] are constructed in Matlab/Simulink. A trajectory tracking control is simulated in Simulink. Torque ripple is also analyzed by tracking a constant torque command.

In Chapter 6, based on the obtained experimental data in Chapter 4, the implementation of the torque controller designed in Chapter 5 is discussed. The trajectory tracking and constant torque command tracking experiment are done to analyze the performance of the implemented reduced torque control method.

Chapter 2
Fundamental of The Switched Reluctance Motors

In this chapter, the principles of operation and the mathematical model of the SR motor are presented. Due to the doubly salient structure of the SR motor, its normal mode of operation requires the stator and rotor iron to be in magnetic saturation. As a result, the mathematical model of the SR motor is nonparametric and can only be established with experimental data, instead of an analytical representation. Based on the mathematical model described in section 2.2, simulations are presented to illustrate the operation of the SR motor.

2.1 Physical Principle

2.1.1 Variable Reluctance

As mentioned in section 1.1.1, the reluctance of the flux path varies with rotor position. Specifically, the reluctance of any magnetic circuit is given by

$$\Re = \frac{F}{\Phi} = \frac{Hl}{BS} = \frac{l}{\mu S} \tag{2.2}$$

where $\Re$ is the reluctance, F is the magnetomotive force (mmf), Φ is the flux, H is the magnetizing force in the air gap, l is the length of magnetic path, B is the flux density, S is the cross section area of the magnetic path, and μ is the permeability of the magnetic material.

The three parameters l, S, and μ contribute to the variation of the magnetic circuit reluctance as the angular position of the rotor changes. Before the stator yoke and the rotor yoke overlap, the permeability μ is essentially equal to the permeability of free space μ_0, which is very small compared to the permeability of the core material. Therefore, the reluctance $\Re$ is maximum at the unaligned position and does not vary in the range where no overlapping occurs as the length of the magnetic path l is constant. From the position where the overlapping occurs to the aligned position, permeability μ increases substantially as the overlapping area increases. At the aligned position, the overlapping area reaches the maximum value. Therefore, the permeability μ is maximum at the aligned position, or the reluctance $\Re$ reaches its minimum value at that position.

Because of the small value of the reluctance $\Re$ at the unaligned position, the flux Φ is not saturated. At the beginning of overlap, due to the substantial increase of the reluctance, the flux Φ starts to saturate with the heaviest saturation occurring at the aligned position.

In SR motors, the inductance L is more often used instead of the reluctance $\Re$, in representing the model or equations of the motor (although such kind of motors are termed switched *reluctance* motors). The relationship between reluctance and inductance is given by

$$L = \frac{\lambda}{i} = \frac{N\Phi}{i} = \frac{N^2}{\Re} \tag{2.3}$$

where λ is the flux linkage, i is the phase current, and N is the number of turns per phase.

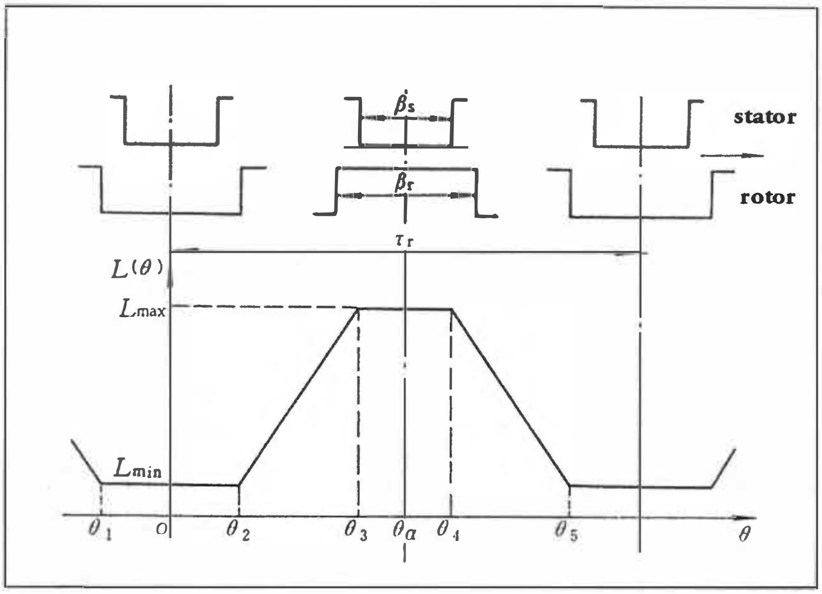

Figure 4. Inductance vs Rotor Position for a constant current (From [1])

Figure 4 illustrates the periodic change of inductance versus rotor position assuming that no saturation exists (A linear magnetics model). β_s denotes the stator pole-arc and β_r denotes the rotor pole-arc. The abscissa of Figure 4 is the mechanical rotor position. τ_r denotes the absolute torque zone within which a phase can produce non-zero torque. The angles β_s, β_r are also indicated in Figure 2, which gives a more geometric view of these definitions.

In Figure 4, θ_2 is the angle where the overlapping of the stator and rotor poles occurs. Before this position, the phase inductance keeps its minimum value $L_{\min}$. θ_3 is the position where the stator pole-arc β_s becomes fully overlapped with the rotor pole-arc β_r. Between the position θ_2 and θ_3, the phase inductance increases linearly as the rotor moves. From θ_4, the full overlapping of the stator and rotor poles ends and the phase inductance decreases linearly until the rotor reaches the position θ_5 where no overlapping exists and the phase inductance becomes $L_{\min}$ again. The interval between θ_3 and θ_4 is termed "dead zone". During this interval, the phase inductance keeps its maximum value $L_{\max}$. If β_r is equal to β_s, there is no "dead zone". The 6/4 SR motor illustrated in Figure 1 and Figure 2 is of this kind, that is, does not have "dead zone".

2.1.2 Energy Conversion

Because the reluctance varies with rotor position and magnetic saturation is part of the normal operation of SR motors, there is no simple analytical expression for the magnetic field produced by the phase windings. The energy conversion of SR motors is hereby analyzed in this section by a general energy conversion approach presented in [2].

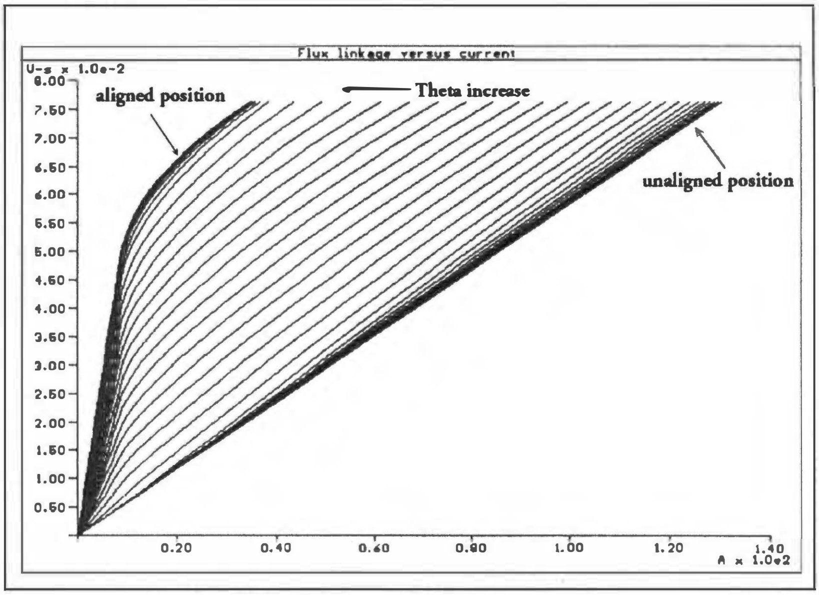

Figure 5. Complete set of magnetization curve. Courtesy Magna Physics Publishing

As shown in Figure 5, the flux linkage is a nonlinear function of both phase current and rotor position. Because of the large air gap, the magnetization is low and does not reach saturation at the unaligned position. Therefore, the magnetization curve is essentially linear as a function of current at $\theta = \theta_{unaligned}$, as indicated in Figure 5. In contrast, the magnetization curve at the aligned position is heavily saturated because of the small air gap.

Figure 6 shows one typical magnetization curve selected from the curve cluster shown in Figure 5. It is the magnetization curve of one phase winding of a SR motor with rotor angle locked somewhere between an aligned position and an unaligned position. At any point of this magnetization curve, the coenergy and stored field energy are defined respectively by

$$W_f = \int_0^{\lambda_0} i d\lambda(\theta, i) \tag{2.4}$$

$$W' = \int_0^{i_0} \lambda(\theta, i) di \tag{2.5}$$

$\lambda(\theta, i)$ represents the flux linkage as a function of both current and position. W_f is termed the stored field energy because its value turns out to be the magnetic energy stored in the rotor/stator iron and in the airgap. With the rotor is locked, it is also equal to the electric energy supplied to the phase winding during the time interval in which the phase flux linkage λ builds up from 0 to λ_0.

If the rotor is the released, it will move towards the aligned position. For an infinitesimal displacement $\Delta\theta$, assuming that the phase current i_0 is kept constant, the flux locus moves from point A to point B as illustrated in Figure 7.

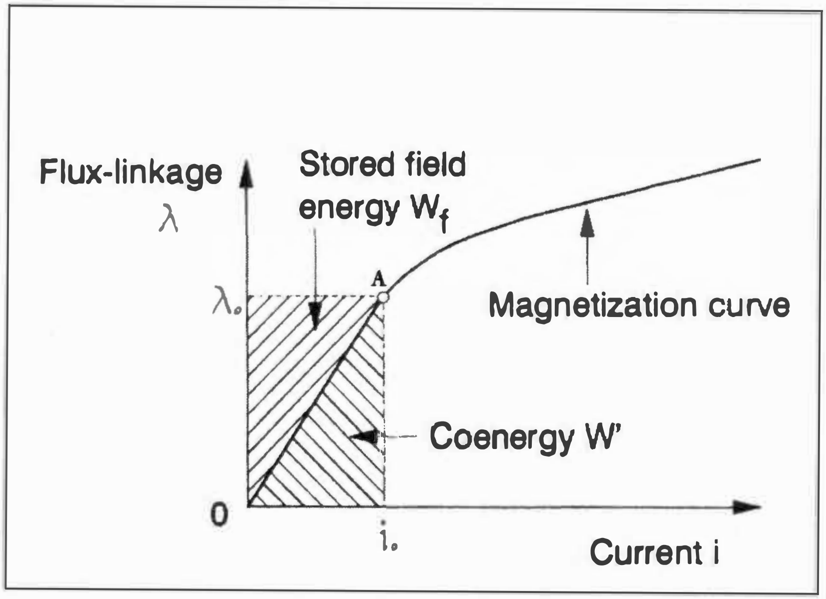

Figure 6. Definition of *coenergy* and *stored field energy* . Courtesy Magna Physics Publishing

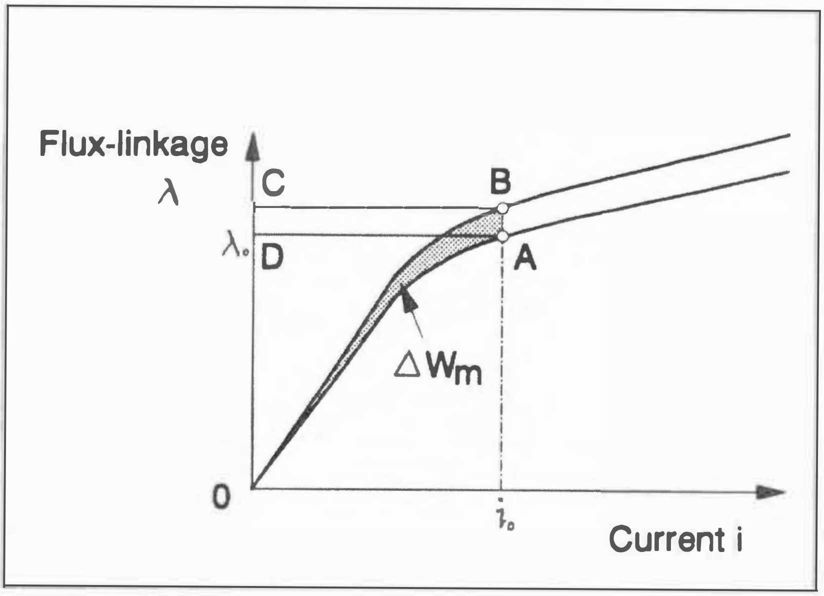

Figure 7. Field Energy, Co-energy, and Mechanical Work. Courtesy Magna Physics Publishing

By conservation of energy, the change in the stored field energy, $\|\Delta W_f\|$, is equal to the mechanical work ΔW_m that is produced by the rotor during the infinitesimal displacement $\Delta\theta$, (ignoring core and copper losses). ΔW_m is labeled in Figure 7 as the cross-hatched area.

By Equation 2.5, the area ΔW_m shown in Figure 7 is equal to the increase of coenergy due to the displacement $\Delta\theta$. Therefore, the mechanical work can be expressed as

$$\Delta W_m = \Delta W' = \int_0^{i_0} \lambda(\theta_B, i)di - \int_0^{i_0} \lambda(\theta_A, i)di$$

By expressing the mechanical work ΔW_m as

$$\Delta W_m = \tau\Delta\theta$$

The mechanical torque can be expressed as

$$\tau = \frac{\Delta W_m}{\Delta\theta} = \frac{\int_0^{i_0} \lambda(\theta_B, i)di - \int_0^{i_0} \lambda(\theta_A, i)di}{\Delta\theta}$$

Taking the limit $\Delta\theta \to 0$ and for any current i, the instantaneous torque of a SR motor then can be defined as

$$\tau = \frac{\partial}{\partial\theta}\int_0^{i} \lambda(\theta, i')di' \tag{2.6}$$

For a linear flux model, i.e., $\lambda(\theta, i) = L(\theta)i$, Equation 2.6 can be rewritten as

$$\tau = \int_0^{i} \frac{\partial\lambda(\theta, i')}{\partial\theta}di' = \int_0^{i} \frac{dL}{d\theta}i'di' = \frac{dL}{d\theta}\int_0^{i} i'di' = \frac{1}{2}i^2\frac{dL}{d\theta} \tag{2.7}$$

Equation 2.7 indicates an interesting property of the SR motors, the torque is independent of the sign of the phase current, but instead is determined by the sign of $dL/d\theta$. Moreover, the absolute value of $dL/d\theta$ contributes to the amount of mechanical torque. Therefore, SR motors are designed to have large $L_{\max}/L_{\min}$ ratio, hence a large absolute value of $dL/d\theta$ to obtain high torque (Refer to Figure 4).

2.1.3 Phase Current

The inductance curve shown in Figure 4 is redrawn in Figure 8. It shows that $dL/d\theta$ is negative for $\theta > \theta_4$. If positive torque is required, Equation 2.7 indicates that the phase current should be regulated to zero before θ_4 to avoid any negative torque. In Figure 8, θ_c is termed the commutation angle and is the angle at which the phase voltage is either turned off or reversed in order to extinguish the phase current. The current shape after commutation is different, depending on when commutation begins. As shown in Figure 8, if one shifts the commutation point ahead to θ_c', then the phase current would go to zero earlier and follow a steeper slope. This is because at θ_c', the inductance is smaller than at θ_c which forces the current to die out more quickly. For high speed operations, the commutation is started earlier in order to have enough time for a given voltage to extinguish the phase current before θ_4.

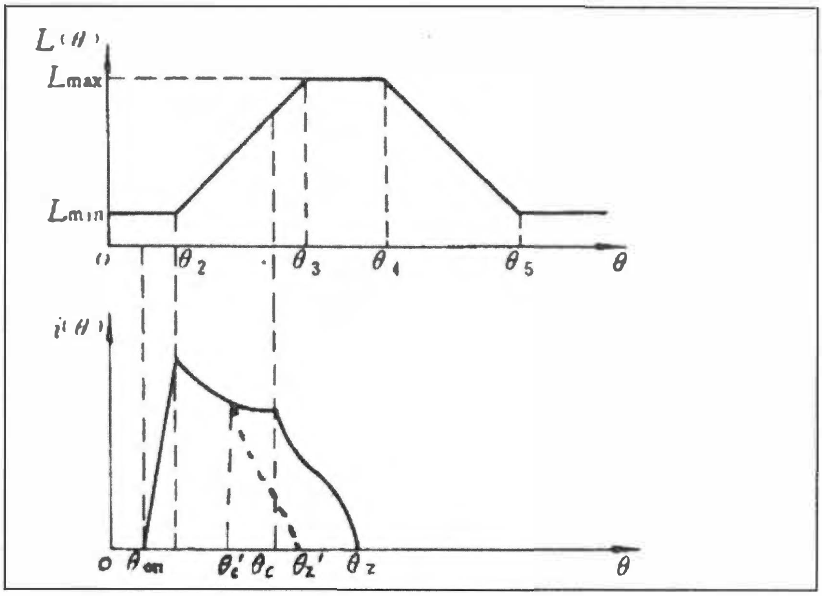

Figure 8. Inductance Curve and Phase Current

On the other hand, according to Equation 2.7, the phase current is expected to reach a high value when inductance begins to increase so that torque could be produced. This means that the stator phase winding should be excited between 0 and θ_2. Because in that region, the inductance is at its minimum value, allowing the phase current to build up quickly. As shown in Figure 8, if the phase winding is excited at θ_{on}, phase current builds up almost linearly and reaches a high value when the rotor enters region $[\theta_2, \theta_3]$ in which effective torque can be produced.

If the "dead zone" does not exist, $dL/d\theta$ turns to be negative immediately after the aligned position. This then requires the commutation to occur earlier to avoid the torque from going negative. This then effectively shortens the distance of the region $[\theta_2, \theta_3]$ that can be used to produce effective torque. From this point of view, the "dead zone" is beneficial in SR motor design. However, a SR motor with "dead zone" would have a higher inherent torque ripple and larger current peaks than a comparable non "dead zone" SR motor [10]. If it is considered from the audible noise point of view, research in [11] suggests that "dead zone" is helpful to reduce vibration noise with a rotor arc that is slightly larger than the stator arc. Therefore, "dead zone" is a compromise between various conflicting requirements.

The shape of phase current before commutation is of interest because it varies widely depending on when the phase winding is excited and what the rotor speed is. To illustrate the effect of the firing angle θ_{on} on the shape of phase current, two step response simulations were done here in Matlab/Simulink. The SR motor model used in these two simulations is a 6/4 linear magnetics model, which is given in detail in section 2.2.2.

For the first simulation, a step voltage is fed into phase A and the initial rotor position is set to be 1° instead of 0° so that the rotor will move in the positive direction (Refer to Figure 1). The top plot in Figure 9 shows that the rotor stops at 45^0 after some oscillation which is the aligned position of phase A, as labeled in Figure 2. The bottom plot in Figure 9 is the corresponding phase current. Plotting this phase current versus rotor position yields Figure 10. To analyze the current shape shown in Figure 10, the electrical equation of the stator phase winding is given here by

$$V = \frac{d\lambda(\theta, i)}{dt} + iR = \frac{\partial\lambda(\theta, i)}{\partial\theta}\omega + \frac{\partial\lambda(\theta, i)}{\partial i}\frac{di}{dt} + iR \tag{2.8}$$

where θ is the mechanical angle, ω is the angular speed, R is the phase resistance, and V is the phase voltage. The mutual flux between the phases is assumed to be zero.

For the linear flux model used in the simulation, ignoring the term iR (the value of iR is small by design because a high value of iR means high energy loss in the stator windings), equation 2.8 can be rewritten as

$$V = i\frac{dL(\theta)}{d\theta}\omega + L\frac{di}{dt} \tag{2.9}$$

where $L(\theta)$ is given in Figure 17.

As is done in section 2.1.2, this simplification helps in doing the analysis without losing the essential characteristics of the motor.

In figure 10, the phase current builds up almost simultaneously with the applied step phase voltage. This is because at the start, the rotor is at the minimum inductance region $L = L_{\text{min}}$ and $dL(\theta)/d\theta = 0$, allowing the current to built up almost immediately. After this period, the rotor moves into the overlapping region where $dL(\theta)/d\theta$ is essentially a constant and greater than zero. Either the high value of $dL(\theta)/d\theta$ during this interval (designed to achieve high output density as discussed in section 2.1.2) or the increasing speed value ω makes the term $i\frac{dL(\theta)}{d\theta}\omega$ greater than the input voltage V which forces di/dt to be negative. Therefore, the phase current decreases as is shown in Figure 10.

After the rotor passes the aligned position, $dL(\theta)/d\theta$ become a negative value, so does the term $i\frac{dL(\theta)}{d\theta}\omega$, which forces di/dt in Equation 1.1 to be positive, i.e., the current increases. This current shape is similar to that illustrated in Figure 8, which is characteristic for SR motors.

The term $i\frac{dL(\theta)}{d\theta}\omega$ is also called back electromotive force (emf). If the commutation was not executed early enough so that phase current still exists when the rotor enters the region where $dL(\theta)/d\theta < 0$, in addition to the negative torque, the phase current can even increase if $\left|i\frac{dL(\theta)}{d\theta}\omega\right|$ is greater than $|V|$, i.e., commutation fails.

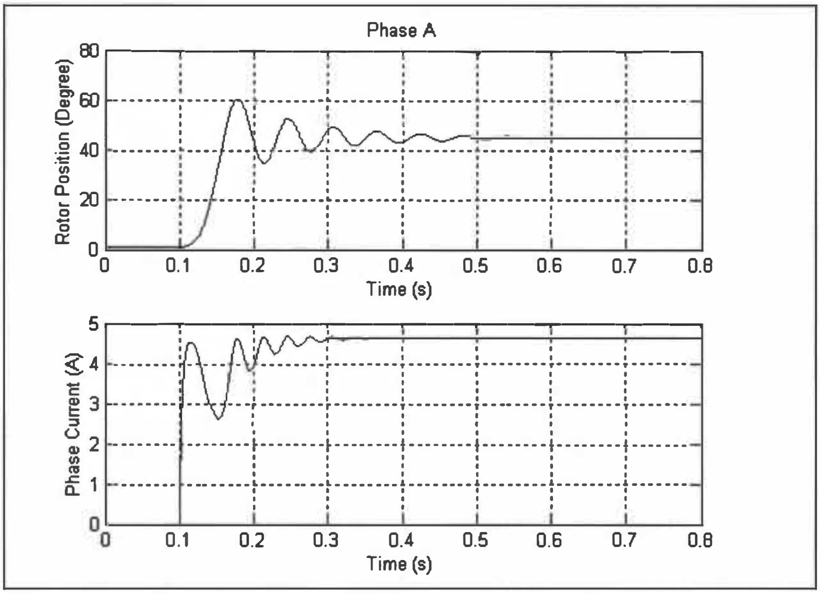

Figure 9. Phase A - Step Response

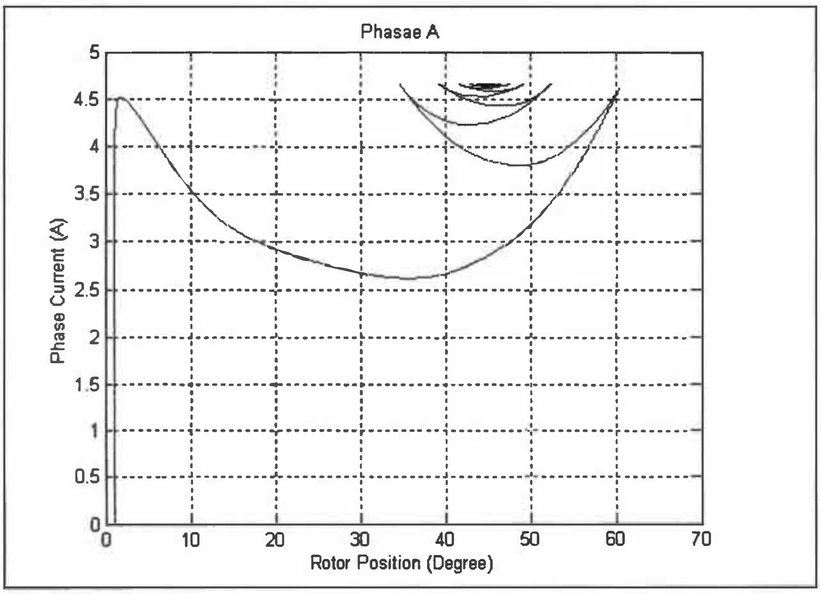

Figure 10. Phase A - Current vs. Position

For the second simulation, a step voltage is fed into phase C. The initial position is 0° (Refer to Figure 1). According to Figure 1, the rotor will move towards the aligned position of phase C, i.e. 15°. Figure 11 shows the rotor position and phase current versus time. In this case, the large value of inductance L at the initial position retarded the increase of phase current, making the step response more like that of a common first-order LR circuit, as is shown in Figure 12.

These two simulations show explicitly that firing angle θ_{on} and commutation angle θ_c effect the phase current directly. Therefore, they are the two fundamental parameters in control of SR motors. As a result, the phase current at the commutation point, at which the phase voltage is turned off or reversed, may not be the maximum current as one may guess. However, the flux linkage does reach its maximum at commutation point as is implied by Equation 2.10.

$$\lambda(\theta, i) = \int_0^t (V - iR)dt \tag{2.10}$$

Figure 13 and Figure 14 show simulation results of two typical current and flux linkage wave forms that produce positive and negative phase torque, respectively. The model used in the simulation is the linear magnetics model described in section 2.2.2, which has the 12/8 structure, the same structure as the experimental SR motor.

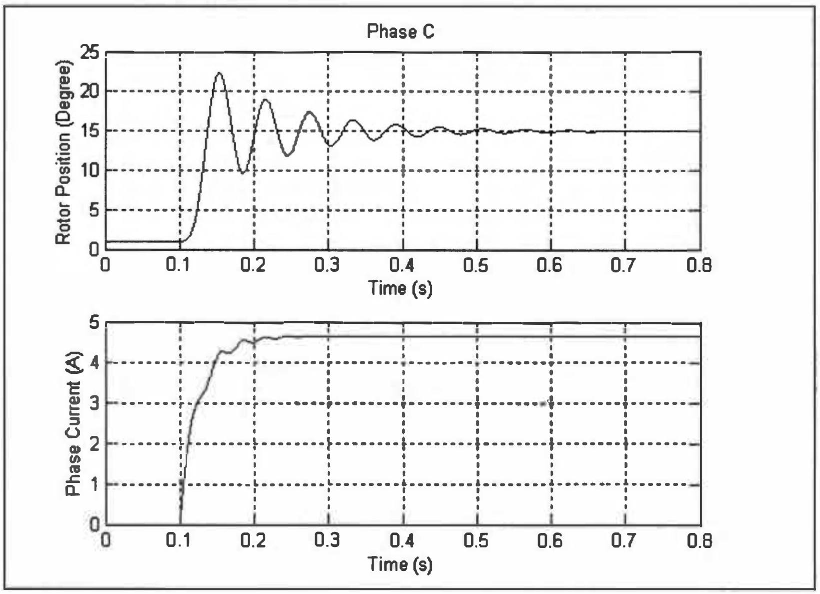

Figure 11. Phase C - Step Response

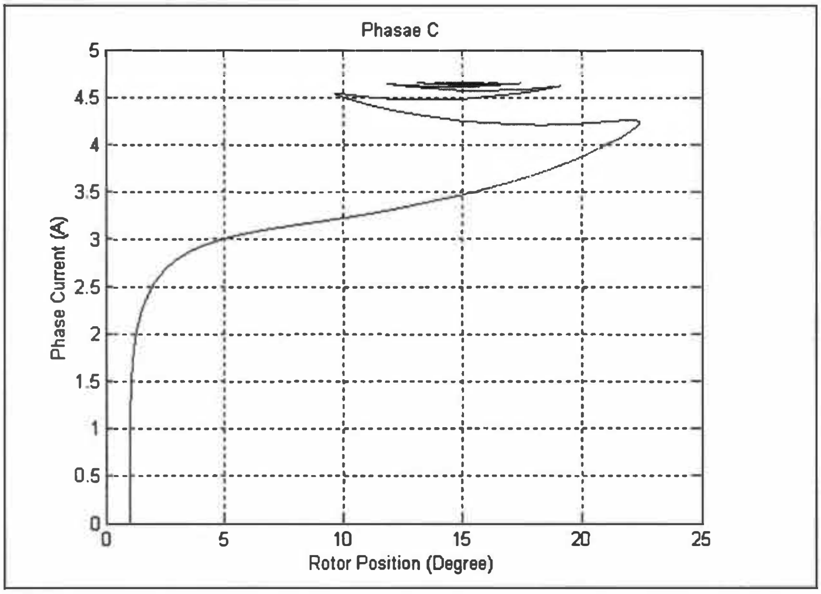

Figure 12. Phase C - Current vs. Position

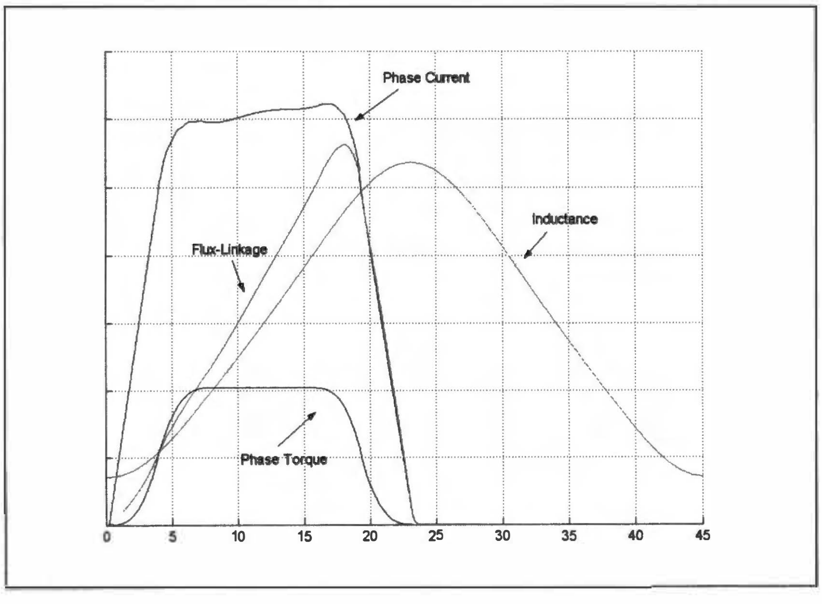

Figure 13. Inductance, phase current, flux-linkage versus rotor position producing positive torque

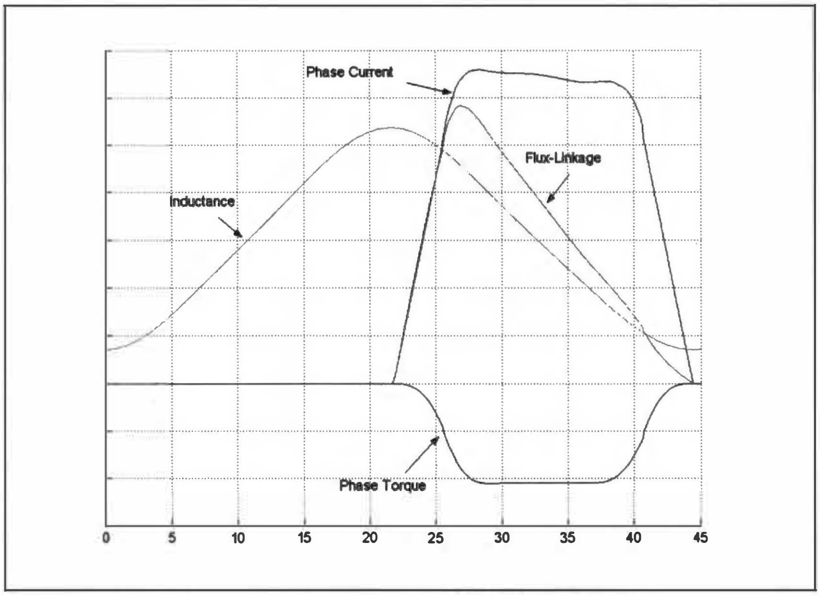

Figure 14. Inductance, phase current, flux-linkage versus rotor position producing negative torque

2.1.4 Energy Ratio and Saturation

According to the energy conversion mechanism described in section 2.1.2, the applied electrical energy is not converted into mechanical work completely. For an entire energy conversion loop, the residual stored field energy after phase current goes to zero feeds back to the power source eventually. The diagonal area labeled **R** in Figure 15 is this residual stored field energy that is not converted to mechanical work.

Lawrenson [2] introduced the concept of *energy ratio* to evaluate the efficiency of energy conversion of SR motors, which is defined as

$$\mathbf{E} = \frac{\mathbf{W}}{\mathbf{W} + \mathbf{R}}$$

where **R** is the residual stored field energy and **W** is the converted energy which is labeled in Figure 15 too.

In Figure 15, as the voltage is applied, the phase current starts to build up from zero. The flux thus moves up along the lower locus from O to C. At point C, phase current is commutated. Flux then comes back along the upper locus from C back to O as the current also goes to zero.

Figure 15 is plotted for a SR motor with saturation, which shows that more than one half of the input electric energy is converted to the mechanical work for a single energy conversion loop. According to [2], an SR motor with saturated flux linkage could have an energy ratio **E** up to 0.65.

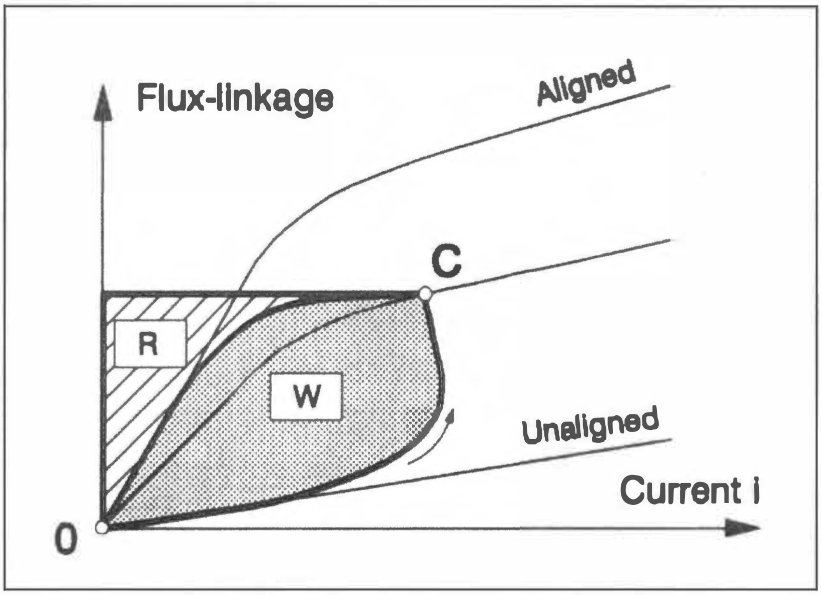

Figure 15. Entire Energy Conversion Loop. Courtesy Magna Physics Publishing

In contrast, a SR motor with linear magnetics will have a substantially lower energy ratio. A linear magnetics SR model will be introduced in section 2.2.2. The energy conversion loop of it is plotted in Figure 16. By discrete integration, the energy ratio **E** was calculated to be 0.507. The stator winding resistance was ignored in the calculation. Therefore, a real linear magnetics SR motor with copper loss will have even lower energy ratio. To obtain a high energy ratio, SR motors are designed to operate under heavy magnetic saturation.

2.2 Mathematical Model

2.2.1 The SR Motor Model

For one phase of a SR motor, assuming the mutual flux between the phases is zero, Faraday's law gives

$$\frac{d\lambda(\theta, i)}{dt} = -iR + v \tag{2.11}$$

By symmetry of the SR motor structure, the flux linkage is periodic in θ with period $2\pi/n_R$. Therefore, one refers to $n_R\theta$ as the electrical angle of a SR motor. With an abuse of notation, Equation 2.11 can be rewritten as

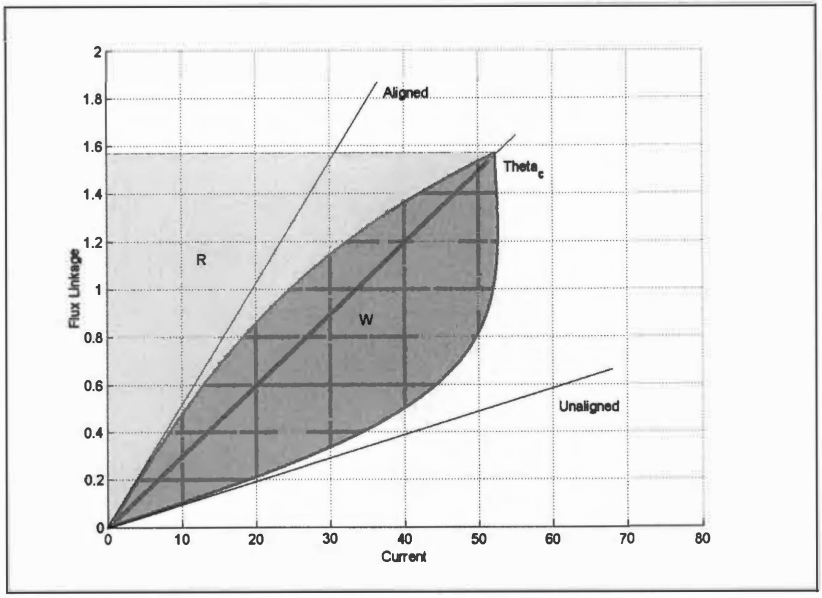

Figure 16. Entire Energy Conversion Loop of a Linear Magnetics SR Model

$$\frac{d}{dt}\lambda(n_R\theta, i) = -iR + v \tag{2.12}$$

In addition, the expressions for the flux linkages of the different phases are just shifted by $\theta_s = 2\pi/qn_R$. For the three-phase SR motor, the electrical equations are given by

$$\begin{aligned} \frac{d}{dt}\lambda(n_R\theta, i_a) &= -i_aR + v_a \\ \frac{d}{dt}\lambda(n_R(\theta-\theta_s), i_b) &= -i_bR + v_b \\ \frac{d}{dt}\lambda(n_R(\theta-2\theta_s), i_c) &= -i_cR + v_c \end{aligned} \tag{2.13}$$

The mechanical equation of the SR motor is

$$J\frac{d\omega}{dt} + B\omega = \tau(n_R\theta, i_a, i_b, i_c) - \tau_L \tag{2.14}$$

where J is the motor inertia, B is the viscous coefficient and τ_L is the load torque and the torque is given by

$$\tau(n_R\theta, i_a, i_b, i_c) = \tau_a(n_R\theta, i_a) + \tau_b(n_R\theta, i_b) + \tau_c(n_R\theta, i_c) \tag{2.15}$$

$$\begin{aligned}
\tau_a(n_R\theta, i_a) &= f(n_R\theta, i_a) \triangleq \frac{\partial}{\partial\theta}\int_0^{i_a} \lambda(n_R\theta, i'_a)di'_a \qquad (2.16)\\
\tau_b(n_R\theta, i_b) &= f(n_R(\theta-\theta_s), i_b) \triangleq \frac{\partial}{\partial\theta}\int_0^{i_b} \lambda(n_R(\theta-\theta_s), i'_b)di'_b\\
\tau_c(n_R\theta, i_c) &= f(n_R(\theta-2\theta_s), i_c) \triangleq \frac{\partial}{\partial\theta}\int_0^{i_c} \lambda(n_R(\theta-2\theta_s), i'_c)di'_c
\end{aligned}$$

Equations 2.13, 2.14,2.15 and 2.16 determine the mathematical model of a SR motor.

Expanding Equations 2.13 gives

$$\begin{aligned}
\frac{di_a}{dt} &= (-i_aR - \frac{\partial}{\partial\theta}\lambda(n_R\theta, i_a)n_R\omega + v_a)/\frac{\partial}{\partial i_a}\lambda(n_R\theta, i_a) \qquad (2.17)\\
\frac{di_b}{dt} &= (-i_bR - \frac{\partial}{\partial\theta}\lambda(n_R(\theta-\theta_s), i_b)n_R\omega + v_b)/\frac{\partial}{\partial i_b}\lambda(n_R(\theta-\theta_s), i_b)\\
\frac{di_c}{dt} &= (-i_cR - \frac{\partial}{\partial\theta}\lambda(n_R(\theta-2\theta_s), i_c)n_R\omega + v_c)/\frac{\partial}{\partial i_c}\lambda(n_R(\theta-2\theta_s), i_c)
\end{aligned}$$

Equation 2.17 shows that if the flux linkage $\lambda(\theta, i)$ is known (for $0 \leqslant \theta \leqslant \pi/n_R$, symmetry of the motor structure is guaranteed), the electrical equations of a SR motor is then determined.

As is the nature of SR motors, $\lambda(n_R\theta, i)$ is a nonlinear function of θ and i which must be found by experiments.

2.2.2 The Linear Magnetics Model

To establish a linear magnetics model, $L(\theta)$ is defined first. As shown in Figure 4, $L(\theta)$ is even symmetric to $\theta = 0°$. Therefore, its Fourier Series representation has the form

$$L(n_R\theta) = a_0 - \sum_{k=1}^{\infty} a_k \cos(kn_R\theta) \qquad (2.18)$$

With $\lambda(\theta, i) = L(\theta)i$, the flux linkage is given by

$$\lambda(n_R\theta, i) = (a_0 - \sum_{k=1}^{\infty} a_k \cos(kn_R\theta))i \qquad (2.19)$$

Substituting Equation 2.19 into Equation 2.17 gives the current equations.

For the instantaneous torque of a linear model, a simpler expression than Equation 2.16 can be derived from Equation 2.7. First, differentiating Equation 2.18 gives

$$\frac{dL(n_R\theta)}{d\theta} = n_R\sum_{k=1}^{\infty} ka_k \sin(kn_R\theta) \tag{2.20}$$

Then, substituting Equation 2.20 into Equation 2.7 gives the instantaneous torque simply as

$$\tau(n_R\theta, i) = \frac{1}{2}i^2\frac{dL(n_R\theta)}{d\theta} = \frac{1}{2}i^2 n_R\sum_{k=1}^{\infty} ka_k \sin(kn_R\theta) \tag{2.21}$$

In [10], a Fourier Series of $L(\theta)$ up to third harmonics is given as

$$L_j(n_R\theta) = a_0 - \sum_{k=1}^{3} a_k \cos[kn_R(\theta - (j-1)\theta_s)] \tag{2.22}$$

$$\lambda_j(n_R\theta) = \{a_0 - \sum_{k=1}^{3} a_k \cos[kn_R(\theta - (j-1)\theta_s)]\}i_j \tag{2.23}$$

$$\tau_j(n_R\theta, i_j) = \frac{1}{2}i_j^2 n_R\sum_{k=1}^{3} ka_k \sin[kn_R(\theta - (j-1)\theta_s)] \tag{2.24}$$

where $j = 1, 2, 3$ stands for phase A, B, C, respectively, and the coefficients are given as

$$\begin{aligned} a_0 &= 0.03 \\ a_1 &= 0.0222 \\ a_2 &= 0.0004 \\ a_3 &= 0.0011 \end{aligned}$$

For the simulations described in section 2.1.3 (see Figure 10 and Figure 12), the number of rotor poles is set as $n_R = 4$ in the two step response to make it coincident with the 6/4 SR motor illustrated in Figure 1 and Figure 2.

The parameter n_R is set to be 8 to plot Figure 13 and Figure 14, because it is the number of rotor poles in the experimental SR motor.

Figure 17 plots the inductance and phase torques of this specific model with $n_R = 8$ between 0°-90°, where the torque is calculated with constant phase current $I = 2.5(A)$.

As discussed in section 2.1.4, the SR motor has a low energy ratio. To illustrate this, an energy conversion loop based on linear magnetics was calculated. The SR motor model used is the linear model with a Fourier Series of $L(\theta)$ up to first harmonics. The equation for the flux linkage is then

$$\lambda(n_R\theta) = [a_0 - a_1 \cos(n_R\theta)]i \tag{2.25}$$

where a_0 and a_1 are given by

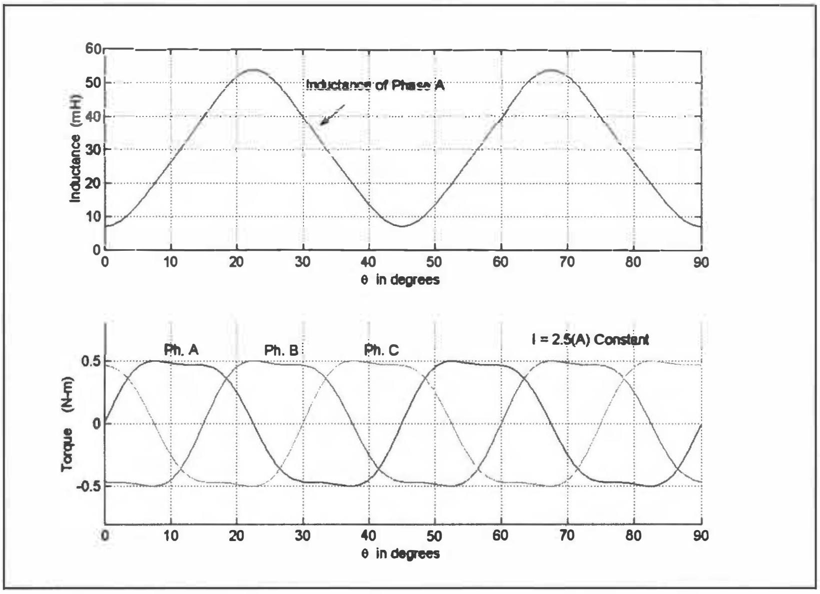

Figure 17. Inductance and Torque vs. Position. (The Linear Model Uses in This Paper)

$$
\begin{aligned}
a_0 &= \frac{1}{2}(L_a + L_u) \\
a_1 &= \frac{1}{2}(L_a - L_u)
\end{aligned}
$$

Here L_a is the inductance at the aligned position and L_u is the inductance at the unaligned position .

Integrating Equation 2.11 with initial condition $\lambda(0) = 0$, assuming a constant speed ω_0 ($\theta(t) = \omega_0 t$) and ignoring the phase resistance R gives

$$
\begin{aligned}
\lambda(\theta) &= Vt = \frac{V}{\omega_0}\theta \quad for \quad 0 \leq \theta \leq \theta_c \\
\lambda(\theta) &= \lambda_c - V(t - t_c) = \lambda_c - V\frac{(\theta - \theta_c)}{\omega_0} = 2\lambda_c - \frac{V}{\omega_0}\theta \quad for \quad \theta_c \leq \theta \leq 2\theta_c
\end{aligned}
\tag{2.26}
$$

were θ_c is the commutation angle indicated in Figure 8 and λ_c is the flux linkage at θ_c.

Solving Equation 2.26 to get θ as a function of λ and substituting into Equation 2.25, the current i as a function of λ is given by

$$
\begin{aligned}
i &= \frac{\lambda}{[a_0 - a_1 \cos(n_R \lambda \omega_0 / V)]} \quad for \quad 0 \leq \theta \leq \theta_c \\
i &= \frac{\lambda}{[a_0 - a_1 \cos(n_R (2\lambda_c - \lambda) \omega_0 / V)]} \quad for \quad \theta_c \leq \theta \leq 2\theta_c
\end{aligned}
\tag{2.27}
$$

Figure 16 is plotted using Equation 2.27 with coefficients and parameters given by

$$
\begin{aligned}
V &= 200(V) \\
\omega_0 &= 50(rad/s) \\
L_a &= 50(mH) \\
L_u &= 10(mH) \\
n_R &= 4 \\
\theta_{on} &= 0^\circ \\
\theta_c &= 22.5^\circ
\end{aligned}
$$

As the speed is assumed to be constant and the initial condition is set to be $\lambda(0) = 0$, from Equation 2.26, one can see that the flux linkage λ goes back to zero at $2\theta_c$. For $n_R = 4$, the rotor is at aligned position at 45°. Therefore, the commutation angle θ_c is chosen to be 22.5° to simulate the operation which utilizes the interval of positive $dL/d\theta$ fully without producing any negative torque, i.e., the operation which yields the most possible mechanical work for such a constant voltage input.

Chapter 3 Control Strategies

If the mutual flux between the stator phases is neglected, the torque of a SR motor is given by Equation 2.15 and Equation 2.16. The torque profile $\tau(\theta, i)$ is a nonlinear function of θ and i, which is obtained as a lookup table by experimental data. If the $\lambda(\theta, i)$ profile is acquired by experiment, then the torque-angle characteristic $\tau(\theta, i)$ can be computed from $\lambda(\theta, i)$ by Equation 2.16. In each case, the obtained profile is related to a specific motor that is identified by experiment. For a given SR motor, with known $\tau(\theta, i)$ or $\lambda(\theta, i)$ profile, the torque control is done by the controlling of the current profile in each phase, which consists of control of firing angle θ_{on}, commutation angle θ_c and shape of the current.

Depending on how the current profile is controlled, torque control is often divided into two categories, average torque control and instantaneous torque control [11]. According to their different applications, these two control concepts are discussed in section 3.1 and section 3.2 below. It is notable that for each of these two types of torque control, torque feedback is not employed because a torque transducer is typically not available.

In this thesis, an instantaneous torque controller is simulated and implemented. This control strategy is from the work of Wallace and Taylor in [10]. Section 3.3 describes this control method in detail.

3.1 Variable Speed Control

Variable speed control applications, such as electric vehicles, require the motor to respond smoothly to varying torque commands. The average torque is defined in [11] as

$$\overline{\tau} = \frac{qn_R W}{2\pi}$$

where q is the number of phases so that qn_R is the number of energy conversions per revolution and W is the converted energy in each energy conversion loop (see Figure 15).

A simple control method that is applicable here is square wave torque control [10]. As shown in Figure 18, the stator phases are excited in sequence by square wave currents. The amplitude of the square wave current is proportional to the desired average torque. Usually, PWM hysteresis control method is used to track the square wave reference currents. Therefore, such a average torque control method is called current hysteresis control.

According to [9], instead of controlling the phase current directly, the average phase voltage could be controlled to produce a given average torque, i.e., square wave phase voltages are fed into the stator phases in sequence and the amplitude of the phase voltage is controlled to produce the desired average torque. The reference voltage is tracked by PWM voltage chopping method. This method is thus termed Voltage_PWM method.

However, the above control methods are valid only at speeds below base speed. Base speed is defined as the speed at which the back emf equals the input voltage. The motor also reaches its rated power at this speed for rated current [12]. If the speed exceeds the base speed, the back emf would be greater than the input voltage V (refer to Equation 2.9), which disqualifies the PWM control method for this region of operation.

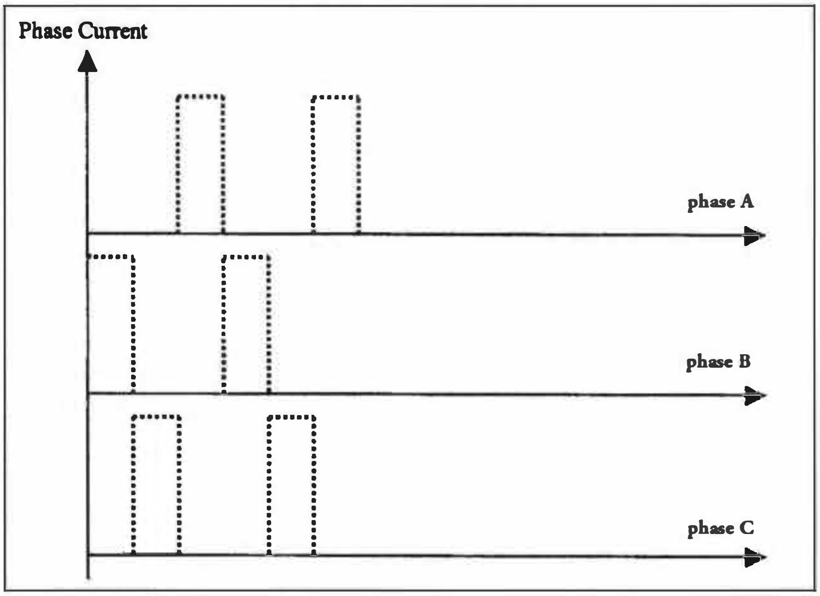

Figure 18. Square wave average torque control

3.2 Servo Control

For the SR motor application in servo systems, one of the control purposes is to reduce the torque ripple that inherently exists in the average torque control. In average torque control, the current references of two subsequent phases are designed independently, i.e., the current profile between two subsequent phase excitations is not controlled. Therefore, high torque ripple will occur during commutation. Also, the flat top of the current shape is expected to produce torque ripple.

To reduce or even eliminate the torque ripple, the control of the torque at each instant in time is considered. Wallace and Taylor [10] presented an instantaneous torque control method which is the control method implemented in this thesis. This control method, like all the other advanced torque control methods, assumes that a perfect current tracking is realized by current tracking loop. Therefore, the task of control is to define the reference current such that the desired torque is tracked instantaneously.

Figure 19 shows a simulation result of this control method tracking a constant torque reference τ^d, where the model is the 3-phase 12/8 SR motor defined in section 2.2.2. As shown in the figure, the commutation angle θ_c is defined as the position where the two adjacent phases can produce the same torque with the same current in their windings. In the interval $[\theta_c^j, \theta_c^j + \theta_s]$, phase j is the *strong* phase that can produce the largest torque of desired polarity for a given current. The current reference of phase $j-1$ is designed to decrease to zero linearly in the interval $[\theta_c^j, \theta_z^{j-1}]$ so that it is brought to zero before it can produce negative torque. The current reference of phase j before θ_c^j is designed to increase linearly from zero to $i_j(\theta_c^j) = g(\frac{1}{2}\tau^d(\theta_c^j), \theta_c^j)$. The function $i = g(\tau, \theta)$ is obtained by inverting experimentally determined function $\tau(\theta, i)$. As the rotor position increases, phase $j+1$ will take the place of phase j to be the *strong* phase at position $\theta_c^j + \theta_s$. Then the reference current of phase j is commutated at $\theta_c^j + \theta_s$ and goes to zero linearly and phase $j+1$ becomes the phase that produces the desired torque. During the *strong* period, e.g., the interval $\theta_c^j \rightarrow \theta_c^j + \theta_s$ for phase j, the current reference is defined by $i_j(\theta) = g(\tau_j^d(\theta), \theta)$, with $\tau_j^d(\theta) = \tau^d(\theta) - \tau_{j-1}(\theta) - \tau_{j+1}(\theta)$, to track the desired torque τ^d instantaneously.

The reference current design of this control method is to have the *strong* phase produce the commanded torque. Thus the torque per ampere ratio of this control method is high. However, it does not reach the maximum torque per ampere ratio because the current changes linearly with respect to θ during the commutation. In [11], a slight modification is made to make this control method so-called maximum torque per ampere control. The difference is that during commutation, instead of building the current or extinguishing it linearly with respect to θ, the current reference is defined indirectly by $d\lambda/d\theta = \pm V_{DC}/\omega$ (winding resistance R is neglected here), which utilizes the maximum voltage available to accelerate the current commutation so that the *strong* phase produces the desired torque, $\tau^d(\theta)$, as much as possible. To realize this modified method, the relationship $\lambda(\theta, i)$ is required in addition to $\tau(\theta, i)$.

Similarly, an alternative instantaneous torque control method is to define θ_c at the position where two adjacent phases produce the same torque with the same flux linkage in their windings. Instead of defining the current reference, flux linkage reference is defined in a similar way to the maximum torque per ampere control. Such a control method is called maximum torque per flux control, which implies that it will reduce the required phase input voltage for the same desired torque, compared to the maximum torque per ampere control [11].

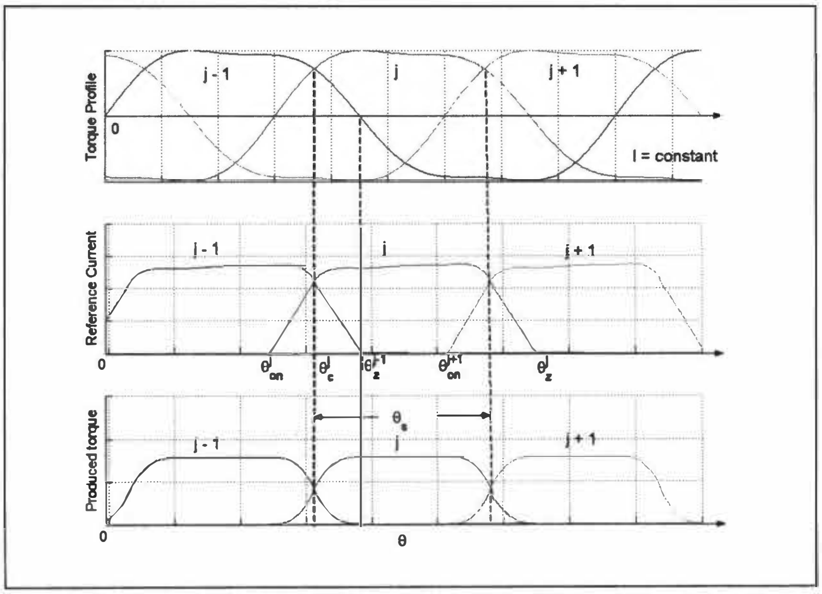

Figure 19. Example of the reduced torque ripple control

3.3 Reduced Torque Ripple Control with A Balanced Commutator

This section describes the detailed algorithm presented by Wallace and Taylor in their paper *A Balanced Commutator for Switched Reluctance Motors to Reduce Torque Ripple* in 1992 [10]. All the algorithms in this section are presented using a 3-phase 12/8 motor structure as this is the type of motor used for the experimental work in this thesis.

The desired torque τ^d at any given time can be represented by the phase torque τ_j^d as

$$\tau^d = \sum_{j=1}^{3} \tau_j^d = \sum_{j=1}^{3} f(n_R(\theta - (j-1)), i_j^d) \tag{3.28}$$

For each phase, the reference current i_j^d that produces the desired phase torque τ_j^d is written as $i_j^d = g(\tau_j^d, \theta)$. The function $i = g(\tau, \theta)$ is formed by inverting the torque function $\tau = f(\theta, i)$, and satisfies

$$f(\theta, g(\tau_j^d, \theta)) = \tau_j^d$$

That is

$$\tau_j^d = f(n_R(\theta - (j-1)), i_j^d) \Leftrightarrow i_j^d = g(\tau_j^d, n_R(\theta - (j-1)))$$

The commutation angle θ_c is defined as the angular position where two consecutive phases can each produce half the desired torque τ^d. That is, θ_c is the solution to

$$g(\theta_c, \frac{1}{2}\left|\tau^d\right|) = g(\theta_c + \theta_s, \frac{1}{2}\left|\tau^d\right|) \tag{3.29}$$

Here, the torque profile $\tau = f(\theta, i)$ is measured for the range $\theta \in [0, \frac{\pi}{n_R}]$ within which only positive torque can be produced, the negative torque profile of the range $\theta \in [-\frac{\pi}{n_R}, 0]$ is obtained by symmetry in θ, i.e., τ is an odd function.

Based on the calculated $\theta_c(\tau^d)$, two conventions for measuring the rotor positions are defined to simplify the expressions

$$\begin{aligned} \theta_+ &= \theta - \theta_c \\ \theta_- &= \theta + \theta_c + \theta_s = \theta - (-\theta_c - \theta_s) \end{aligned}$$

where θ_+ is used for positive τ^d and θ_- is for negative τ^d. The shifted position axes are plotted in Figure 20, where the interval ϕ is the step angle θ_s.

Based on these two definitions a new position reference is defined by

$$\theta_{3\phi} = \begin{cases} \theta_+ \mod 3\phi & for \quad \tau^d > 0 \\ \theta_- \mod 3\phi & for \quad \tau^d < 0 \end{cases}$$

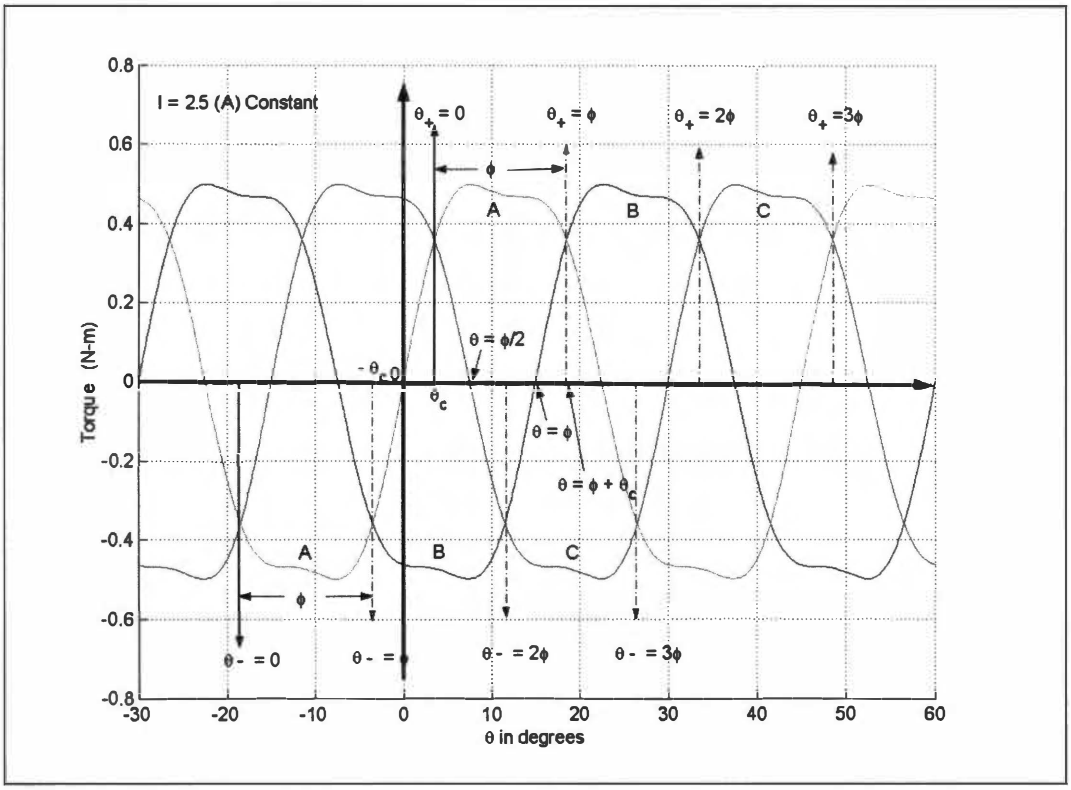

Figure 20. Definition of θ_+ and θ_-

As shown in Figure 20, with respect to the new position reference $\theta_{3\phi}$, a *strong* phase indicator s can be defined by

$$s = \begin{cases} 1 & for \quad \theta \in \Theta_1 \\ 2 & for \quad \theta \in \Theta_2 \\ 3 & for \quad \theta \in \Theta_3 \end{cases} \tag{3.30}$$

where $s = 1, 2, 3$ indicates that the *strong* phase is A, B, C, respectively, and intervals Θ_j is given by

$$\begin{aligned} \Theta_1 &= \{\theta \quad : 0 \leq \theta_{3\phi} < \phi \quad \} \\ \Theta_2 &= \{\theta \quad : \phi \leq \theta_{3\phi} < 2\phi \quad \} \\ \Theta_3 &= \{\theta \quad : 2\phi \leq \theta_{3\phi} < 3\phi \quad \} \end{aligned}$$

During each angular interval Θ_j, the *strong* phase j produces the largest torque component. The current reference of the phase that precedes phase j is designed to decrease linearly in Θ_j, as indicated by *i-falling* in Figure 21. In contrast, the reference current of the phase following phase j is designed to increase linearly in Θ_j (as indicated by *i-rising* in Figure 21), so that it is ready to produce the largest torque component as it becomes the *strong* phase.

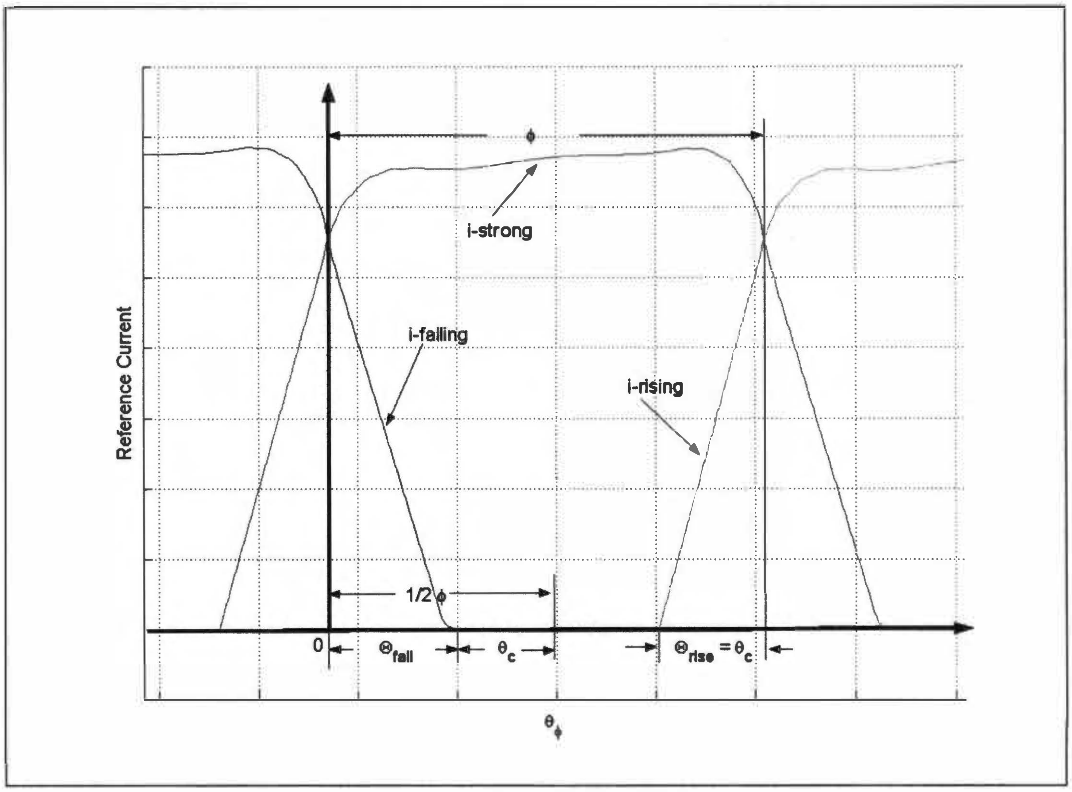

Figure 21. Define the reference current ($\tau^d > 0$)

If r and f are used to indicate the phase whose current is rising or falling during each interval Θ_j, then

$$(s, r, f) = \begin{cases} (1,2,3) & \theta \in \Theta_1 \\ (2,3,1) & \theta \in \Theta_2 \\ (3,1,2) & \theta \in \Theta_3 \end{cases} \tag{3.31}$$

The interval Θ_{rise} and Θ_{fall} indicated in Figure 21 determines the angle θ_{on} and θ_z in Figure 8, the control parameters discussed in section 3.1. In other words, the firing angle θ_{on} and the extinction angle θ_z are actually controlled in this instantaneous torque control method except they are determined implicitly based on the commutation angle θ_c, rather than determined independently for each phase as in the average torque control.

The interval Θ_{rise} is designed to start at the point where the torque-position profile of the rising current phase crosses over the abscissa, and ends coincidently with the end of Θ_j. Therefore, for $\tau^d > 0$, $\Theta_{rise} = \{\theta_+ | \phi - \theta_c \leqslant \theta_+ \leqslant \phi\}$. The interval Θ_{fall} is designed to start coincidently with the start of Θ_j, and is designed to end at the point where the torque-position profile of the falling current phase crosses over abscissa. Therefore, for $\tau^d > 0$, $\Theta_{fall} = \{\theta_+ | 0 \leqslant \theta_+ \leqslant \frac{1}{2}\phi - \theta_c\}$. Figure 21 illustrates these intervals.

For $\tau^d < 0$, the value of Θ_{rise} and Θ_{fall} is reversed because of the symmetry property of the torque profile with respect to the abscissa, as is shown in Figure 22. To express Θ_{rise} and Θ_{fall} by a uniform expression, another position reference θ_ϕ is defined by

$$\theta_\phi = \begin{cases} \theta_+ \mod \phi & for \quad \tau^d > 0 \\ \theta_- \mod \phi & for \quad \tau^d < 0 \end{cases} \tag{3.32}$$

Then, Θ_{rise} and Θ_{fall} are expressed as

For $\tau^d > 0$

$$\begin{aligned} \Theta_{fall} &: \ 0 \le \theta_\phi < \frac{1}{2}\phi - \theta_c \\ \Theta_{rise} &: \ \phi - \theta_c \le \theta_\phi < \phi \end{aligned} \tag{3.33}$$

For $\tau^d < 0$

$$\begin{aligned} \Theta_{fall} &: \ 0 \le \theta_\phi < \theta_c \\ \Theta_{rise} &: \ \frac{1}{2}\phi + \theta_c \le \theta_\phi < \phi \end{aligned}$$

Figure 22 is drawn to illustrate the symmetry of Θ_{rise} and Θ_{fall} with respect to the abscissa for $\tau^d < 0$, while the reference current needs not to go negative for the negative torque as Equation 2.7 indicates. The rising current i_R and the falling current i_F are designed to be linear in the position θ. Therefore,

For $\tau^d > 0$

$$\begin{aligned} i_F(\theta_\phi) &= \frac{g(\theta_c(\tau^d), \frac{1}{2}\tau^d)}{-(\frac{1}{2}\phi - \theta_c)} \cdot (\theta_\phi - (\frac{1}{2}\phi - \theta_c)) \qquad for \qquad \theta_\phi \in \Theta_{fall} \\ i_F(\theta_\phi) &= 0 \qquad otherwise \end{aligned} \tag{3.34}$$

$$\begin{aligned} i_R(\theta) &= \frac{g(\theta_c(\tau^d), \frac{1}{2}\tau^d)}{\theta_c} \cdot (\theta_\phi - (\phi - \theta_c)) \qquad for \qquad \theta_\phi \in \Theta_{rise} \\ i_R(\theta) &= 0 \qquad otherwise \end{aligned}$$

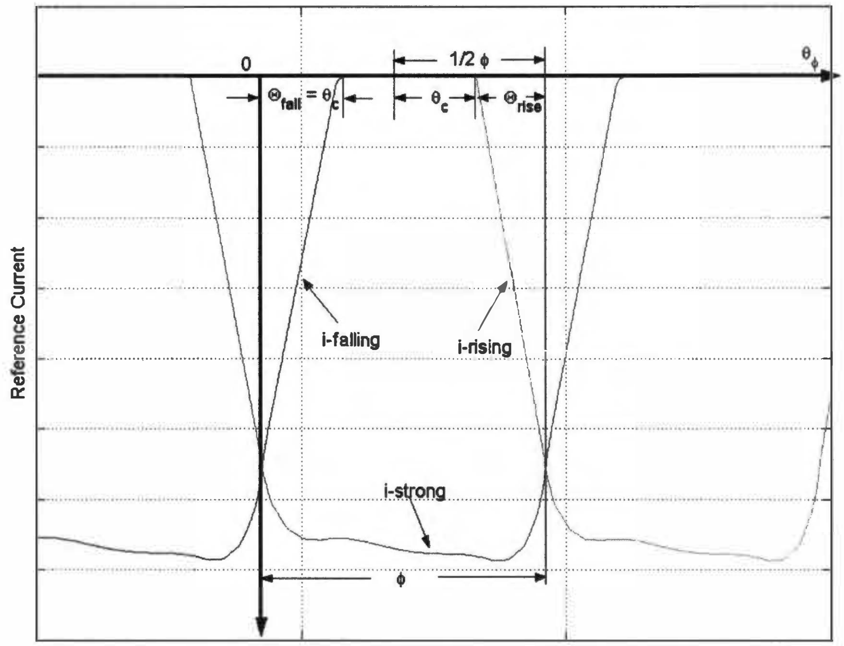

Figure 22. Define the reference current ($\tau^d < 0$)

For $\tau^d < 0$

$$
\begin{aligned}
i_F(\theta_\phi) &= \frac{g(\theta_c(\tau^d), \frac{1}{2}\tau^d)}{-\theta_c} \cdot (\theta_\phi - \theta_c) \qquad for \qquad \theta_\phi \in \Theta_{fall} \\
i_F(\theta_\phi) &= 0 \qquad\qquad\qquad\qquad otherwise
\end{aligned}
$$

$$
\begin{aligned}
i_R(\theta) &= \frac{g(\theta_c(\tau^d), \frac{1}{2}\tau^d)}{\frac{1}{2}\phi - \theta_c} \cdot (\theta_\phi - (\frac{1}{2}\phi + \theta_c)) \qquad for \qquad \theta_\phi \in \Theta_{rise} \\
i_R(\theta) &= 0 \qquad\qquad\qquad\qquad otherwise
\end{aligned}
\tag{3.35}
$$

Here $g(\theta_c(\tau^d), \frac{1}{2}\tau^d)$ is the value of current at the commutation point where two successive phases produce the same torque.

With i_F and i_R, the torque produced by the phases with rising and falling reference currents is given by

$$\tau_f(\theta, i_F) + \tau_r(\theta, i_R)$$

To produce the total desired torque τ^d, under the condition of Equation 3.28, the reference current of the strong phase i_S must be

$$i_S = g(\theta - (s-1)\phi, \tau^d - \tau_f(\theta, i_F) - \tau_r(\theta, i_R) \tag{3.36}$$

where s is the *strong* phase indicator defined by Equation 3.30.

Finally, the phase reference currents i_j^d are assigned according to the indices in Equation 3.31 by

$$i_j^d = \begin{cases} i_S & s = j \\ i_R & r = j \\ i_F & f = j \end{cases} \qquad j = 1, 2, 3 \tag{3.37}$$

Chapter 4
Model Identification of the Experimental SR Motor

A real-time control platform has been developed as a test bench to implement the reduced torque ripple control method. On this platform a three phase SR motor is put through tests to find the torque-angle profile $\tau(\theta, i)$, the flux profile $\lambda(\theta, i)$ and the motor parameters R_s, J and B.

In section 4.1, the real-time control platform is presented in detail. In section 4.2, the identification procedure for $\tau(\theta, i)$, $\lambda(\theta, i)$, R_s, J and B is described.

4.1 Real-time Control Platform

The real-time control platform consists of two personal computers (PCs), one A/D and one D/A interface modules, one timing module, one encoder module and four power electronics drives. Figure 23 illustrates the platform structure.

The host PC shown in Figure 23 runs OS Windows 2000, on which the simulation software Matlab/Simulink and the real-time control integration software RTLAB are installed. The integration software RTLAB is employed to integrate the control algorithms implemented using Simulink blocks with the I/O interface boards. RTLAB provides the A/D, D/A, encoder and timer icons that connect to the drivers corresponding to the A/D, D/A, timing and encoder modules installed on the target PC. By inserting these icons into the Simulink block diagrams, the configuration of the I/O interface is integrated automatically within the Simulink diagrams. These blocks are then converted into C code through RTW (Real Time Workshop). The generated C code is downloaded onto the target PC and is compiled there into executable code. The real-time OS QNX runs on the target PC which executes the code under the control of the RTLAB console block software that is running on the host PC. The command generated by the control algorithms or the data acquired from the A/D module during execution can both be saved on the target PC in real time and transferred onto the host PC for analysis after the execution stops.

As illustrated in Figure 23, on the test bed, a 3-phase SR motor and a load motor are coupled with a torque transducer in between. The load motor is a PM synchronous motor of the BM motor series from Aerotech. A power electronics drive of the BAS drive series from Aerotech is used to control the load motor, which also feedbacks the position signal coming from the encoder that is mounted on the load motor into the encoder module installed on the target PC where the encoded signal is decoded into number of pulses to represent the shaft position. The resolution of the encoder is 4000/rev.

The SR motor is driven by three power amplifiers of the BA series from Aerotech (120VAC, 5Amps continuous) which operates as three current tracking amplifiers.

Three current transducers are used to measure the phase currents. As the amplifiers are in current command, like the torque transducer, they are used only for measurement and not for feedback control. The timer module is used internally by the target PC to synchronize the execution of the software.

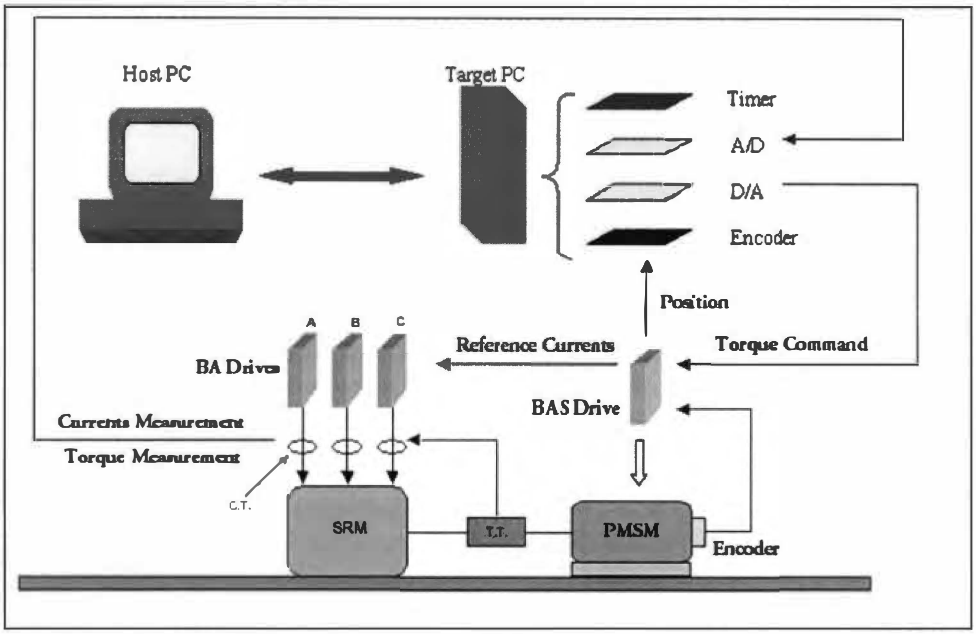

Figure 23. Illustration of the Control Platform

4.2 Motor Identification

The task of identification is to obtain the torque-angle characteristics $\tau(\theta, i)$, $\lambda(\theta, i)$ as well as the system parameters R_s, J and B. The unavailability of the $\tau(\theta, i)$ and $\lambda(\theta, i)$ characteristics from the manufacturer of the SR motor makes motor identification a requisite part of the SR motor control.

4.2.1 Torque-Angle Characteristics $\tau(\theta, i)$

The torque-angle characteristic $\tau(\theta, i)$ is obtained by an automatic identification procedure in which the position of the shaft of the system (see Figure 23) is controlled precisely by the PM synchronous motor to increment in steps of 0.9° for an entire mechanical revolution (360°). With a constant current kept in one phase of the SR motor, the torque is measured by the torque transducer as the motor revolves. The phase current is the increased in steps of $0.24A$ and the above procedure repeated until the current reaches the limit current.

There are several details that are considered in the implementation of such an automatic identification procedure.

1. The torque measurement is based on Newton's second law. Therefore, it gives an exact measurement at the standstill (in which the load motor exerts the same torque as the SR motor). Any small acceleration implies that part of the torque measured at that moment is used for accelerating or decelerating the shaft, which introduces error to the measurement. Therefore, a position trajectory shown in Figure 24 (*d*) is used.

It modifies the trajectory defined by Equation 5.40 and connects them in serial, which provides a still period between two steps to ensure standstill to occur, as is shown in Figure 24 (c).

2. The starting point of the load motor position should be selected, because the encoder uses quadrature counting mode which sets the position to zero at power on. To make the initial position coincident with the SR motor structure, the aligned position for phase A is chosen to be the starting point. To achieve this, a delay time is set before the trajectory starts, during which a constant current is commanded into phase A forcing the rotor to align to it. The delay time is determined by experiment to allow the oscillations to die out so the rotor is aligned to phase A. A special program is written to refresh the encoder so that it starts from 0 when the trajectory starts.

3. Because the position θ is measured in encoder counts ($0 \rightarrow 4000$ for one revolution), the inherent error of θ is $360°/4000 = 0.09°$. It turns out that if the step size of the position reference trajectory is not an integer times 0.09°, the actual shaft trajectory would oscillate between $\pm 0.09^0$. Therefore, the step size of the position reference here is chosen to be 0.9° (or 10 encoder counts). This is shown in Figure 24 (d). The torque is measured at 400 points per revolution.

4. After one mechanical revolution is completed, the position reference is designed to go back to the initial starting point instead of going forward for another revolution. This is to eliminate the accumulative position error that would exist because of the encoder resolution.

5. The position tracking control of the PM synchronous load motor is realized by a PID feedback controller given by

$$i_q = \frac{J}{K_T}\left(\int_0^t k_0(\theta_{ref} - \theta)dt + k_1(\theta_{ref} - \theta) + k_2(\omega_{ref} - \omega)\right) \tag{4.38}$$

where ω_{ref} is computed by the difference equation $\omega_{ref}(nT_s) = [\theta(nT_s) - \theta((n-1)T_s)]/T_s$ online. The current i_q is the desired quadrature current and K_T is the equivalent torque constant of the PM synchronous motor. i_q is fed into the BAS drive through the D/A interface, the torque produced by the PM synchronous motor is given by

$$\tau_L = K_T \cdot i_q \tag{4.39}$$

Equation 4.39 suggests that if the torque transducer is not available, an alternative is to record i_q to calculate the torque.

Following the above procedures, an identification Simulink program was written. By inserting the I/O icons into the block diagram through RTLAB, the automatic torque profile identification is implemented on the control platform. The identification program commands currents into phase A for each revolution from $0 \rightarrow 2.16A$ in steps of $0.24A$. The commanded currents are assumed to be tracked by the power amplifiers.

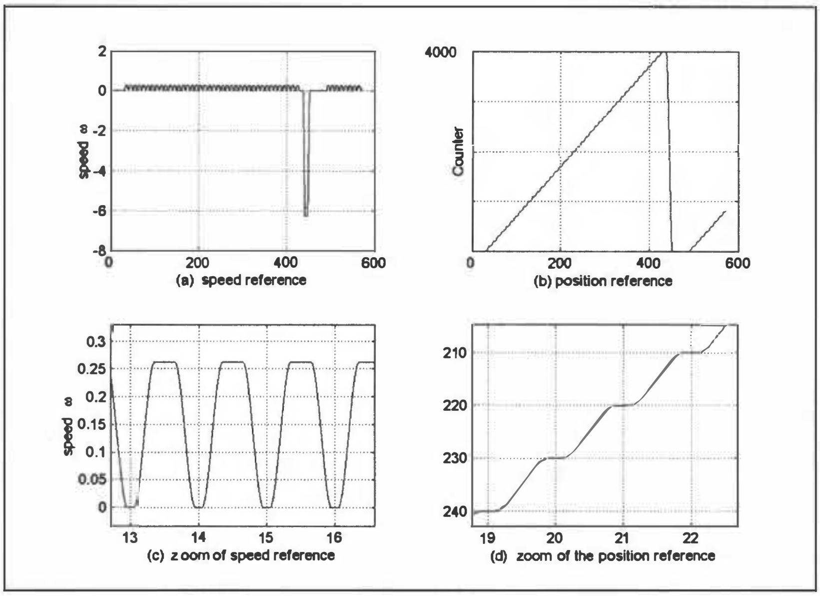

Figure 24. Reference Trajectory of the load motor for identification of $\tau(\theta, i)$

There are steady state errors between the commanded currents and the measured currents due to the accuracy of the amplifiers. The errors are presented below

$Commanded\ Current\ (A)$	$Measured\ Current\ (A)$
0.24	0.181
0.48	0.439
0.72	0.699
0.96	0.961
1.2	1.223
1.44	1.484
1.68	1.744
1.92	2.004
2.16	2.266

where the current is measured by an HP multimeter. To construct the torque-angle characteristic $\tau(\theta, i)$, the measured currents are used.

The maximum commanded current into phase A is chosen to be $2.16A$ because the load motor could not track the reference trajectory when the commanded current exceeds $2.2(A)$ as the BAS drive could not produce enough current.

The measured torque values are stored on the target PC in real time. Then, they are transferred onto the host PC where the raw data is processed. Finally, the torque-angle characteristic is obtained in form of a 9×400 matrix, as is plotted in Figure 25.

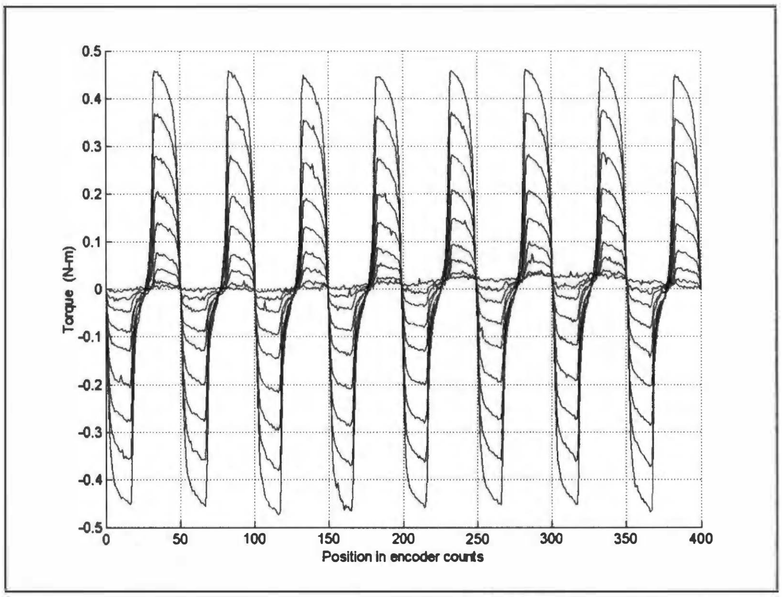

Figure 25. Experimentally Measured Torque as a Function of Position and Current

Figure 25 not only gives the look-up table for $\tau(\theta, i)$, but also indicates that the number of the SR motor rotor poles is 8. According to the design rule of SR motors presented in [2], it is determined that the identified SR motor has a 12/8 structure.

For the 3-phase 12/8 SR motor, the torque-angle characteristic for $\theta \in [0, 22.5°]$ is extracted from Figure 25. The resulting look-up table for $\tau(\theta, i)$ is a 10×25 matrix. Figure 26 and Figure 27 give the 2-D and 3-D plots of this look-up table.

4.2.2 Flux Characteristics $\lambda(\theta, i)$

The flux characteristic $\lambda(\theta, i)$ determines the electric dynamic of the windings of the stator phases. It can be calculated from the obtained look-up table of $\tau(\theta, i)$.

As described in section 2.1.2, the instantaneous toque can be expressed by Equation 2.6, or,

$$\tau(\theta, i) = \frac{\partial}{\partial \theta} \int_0^i \lambda(\theta, i')di'$$

Differentiating the above equation with respect to i gives

$$\frac{\partial \tau(\theta, i)}{\partial i} = \frac{\partial \lambda(\theta, i)}{\partial \theta}$$

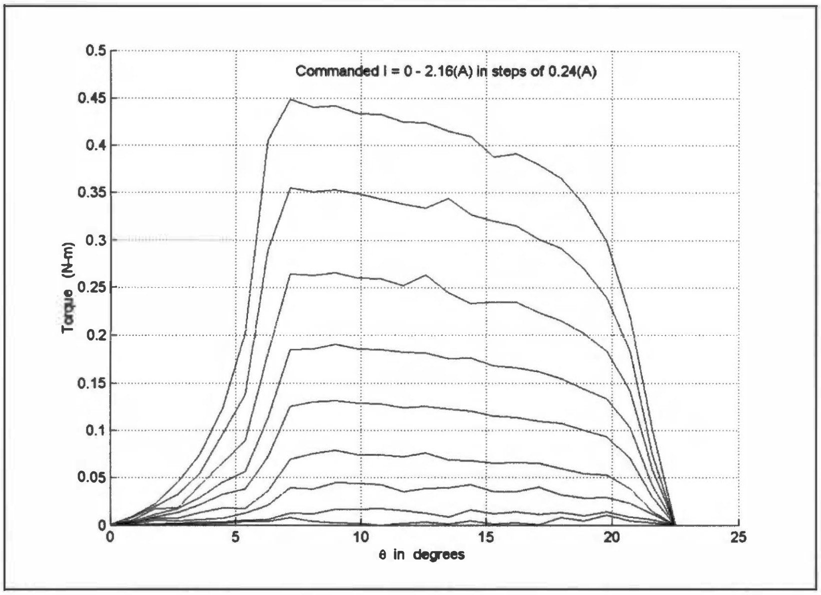

Figure 26. Experimentally Measured $\tau(\theta, i)$ of Phase A for $0° \leqslant \theta \leqslant 22.5°$

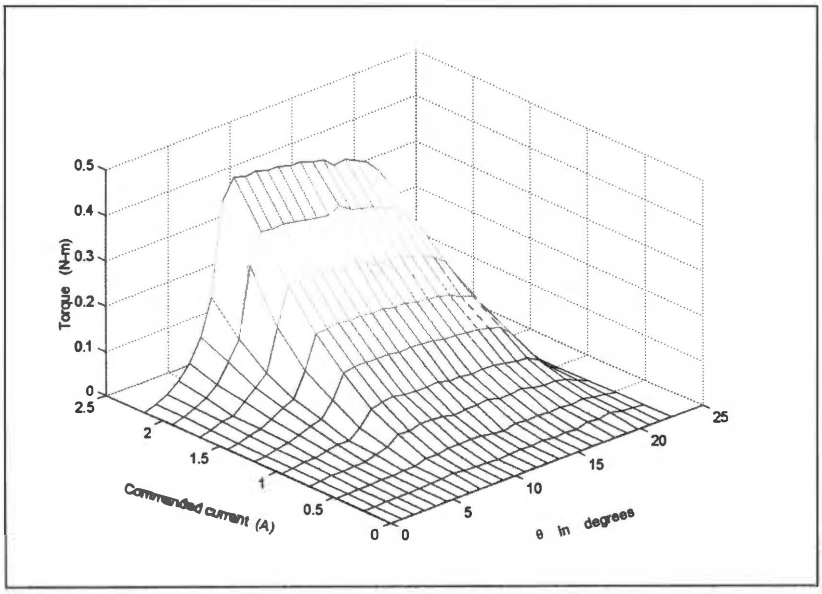

Figure 27. 3D plot of the experimentally measured $\tau(\theta, i)$ of phase A for $0° \leqslant \theta \leqslant 22.5°$

Integrating the above equation with respect to θ gives

$$\lambda(\theta, i) = \int_0^{\theta} \frac{\partial \tau(\theta', i)}{\partial i} d\theta' + \lambda(\theta, i)|_{\theta=0}$$

or

$$\lambda(\theta, i) = \int_0^{\theta} \frac{\partial \tau(\theta', i)}{\partial i} d\theta' + L_u i$$

where L_u is the inductance at the unaligned position.

The calculated look-up table of $\lambda(\theta, i)$ is also a 10×25 matrix. Figure 28 and 29 plots the matrix in 2-D and 3-D, respectively.

4.2.3 B, J and R_s

The viscous coefficient B is identified by driving the system at a constant speed. Under constant speed, the system mechanical equation is simply

$$B\omega = \tau$$

Thus the viscous coefficient is obtained by $B = \tau/\omega$. The PM synchronous motor is forced to track a constant speed trajectory. The torque transducer is used to measure the torque during the constant speed interval. In the experiment, the constant speed ($\omega_{\max}$ in Equation 5.40) is chosen to be 100 (rad/s). The viscous coefficient B is computed to be $6.9803 \times 10^{-5} \frac{N-m}{rad/sec}$.

The inertia of the system which is the combination of the SR motor, the PM synchronous motor and the torque transducer is identified by finding the least-squares estimate based on the mechanical equation

$$J\frac{d\omega}{dt} = \tau - B\omega$$

In the identification experiment, the PM synchronous motor is excited by a varying-frequency sinusoidal quadrature current command, i_q in Equation 4.38. The resulting torque and position are recorded in real time. Then ω and $d\omega/dt$ are computed off-line by backwards differentiation. With the known viscous coefficient B, J is computed by the least-squares approach which in this case is only of one dimension. Figure 30 plots the obtained data. The system inertia J is computed to be $2.9079 \times 10^{-4}\ kg \cdot m^2$, which is approximately two times the inertia of the PM synchronous motor, $1.39 \times 10^{-4}\ kg \cdot m^2$.

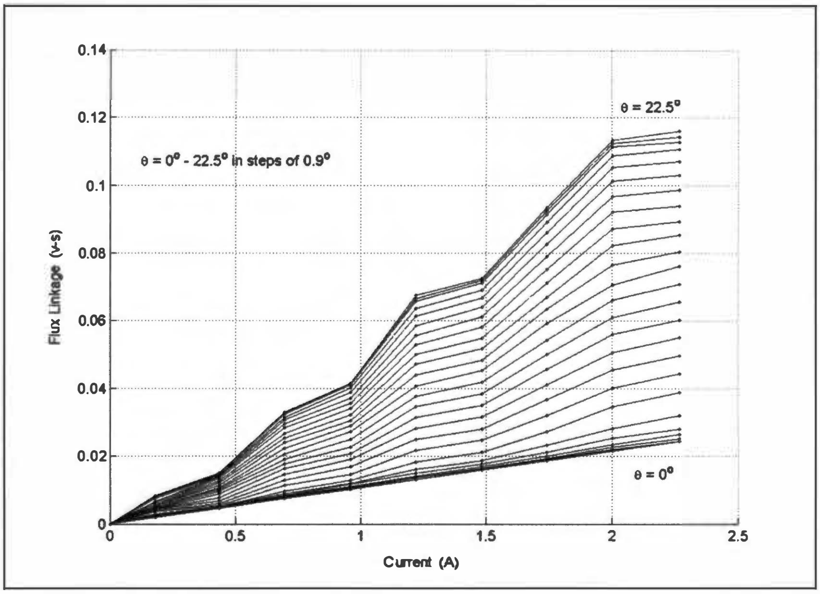

Figure 28. 2D plot of $\lambda(\theta, i)$ of phase A for $0° \leqslant \theta \leqslant 22.5°$

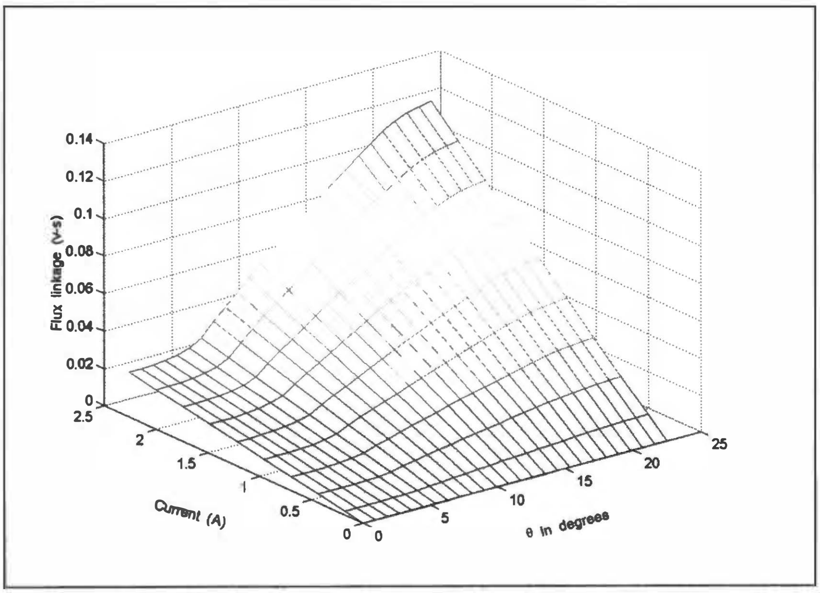

Figure 29. 3D plot of $\lambda(\theta, i)$ of phase A for $0° \leqslant \theta \leqslant 22.5°$

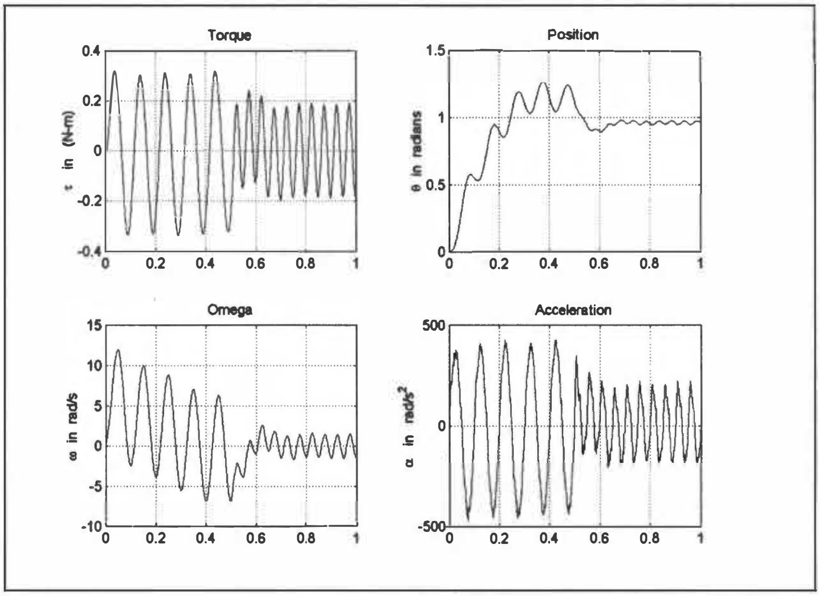

Figure 30. Data obtained for the least-squares estimate of the system inertia J

To complete the SR motor identification, the resistance of the phase winding was measured, which gives $R_s = 2.15\ \Omega$.

Chapter 5
Simulation of The Reduced Torque Ripple Control

In this chapter, the control method proposed by Wallace and Taylor [10] is simulated using the high-level graphic language Simulink. The constructed torque controller is used to control the motor model to track a preset trajectory in the simulation environment and the performance of the control method is examined.

Section 5.1 and section 5.2 introduces the Simulink block diagrams of the motor model and the torque controller, respectively. In section 5.3, the preset trajectory and the whole tracking simulation are described. The simulation results are presented in section 5.4. Finally, in section 5.5, a constant torque command is tracked by the constructed torque controller and the torque ripple is analyzed.

5.1 Motor Model

The SR motor model used here is a 3-phase 12/8 motor model defined by Equations 2.14, 2.16, 2.15 and 2.17. The experimentally obtained look-up table $\tau(\theta, i)$ and $\lambda(\theta, i)$ are used to construct the motor model. As indicated by Equation 2.17, the derivatives of $\lambda(\theta, i)$ with respect to θ and i are required to simulate the electric dynamic of the stator windings. Therefore, two additional look-up tables of $\frac{\partial}{\partial\theta}\lambda(\theta, i)$ and $\frac{\partial}{\partial i}\lambda(\theta, i)$ are calculated from the look-up table of $\lambda(\theta, i)$. Because the look-up table of $\lambda(\theta, i)$ is obtained by mathematical calculation from the look-up table of $\tau(\theta, i)$, it turns out to be insufficient to calculate the look-up tables of $\frac{\partial}{\partial\theta}\lambda(\theta, i)$ and $\frac{\partial}{\partial i}\lambda(\theta, i)$ from it directly (errors introduced by the procedure of calculating $\lambda(\theta, i)$ from $\tau(\theta, i)$ would be enlarged in calculating $\frac{\partial}{\partial\theta}\lambda(\theta, i)$ and $\frac{\partial}{\partial i}\lambda(\theta, i)$ from the look-up table $\lambda(\theta, i)$ directly, which would result in incorrect $\frac{\partial}{\partial\theta}\lambda(\theta, i)$ and $\frac{\partial}{\partial i}\lambda(\theta, i)$). Therefore, the look-up table of $\lambda(\theta, i)$ is first linearly fitted before calculating the look-up table of $\frac{\partial}{\partial\theta}\lambda(\theta, i)$ and $\frac{\partial}{\partial i}\lambda(\theta, i)$. The first order least mean square method is used to fit the look-up table of $\lambda(\theta, i)$, since the calculated $\lambda(\theta, i)$ is fairly linear rather than a saturated one (see Figure 28). It is notable that the SR motor is usually designed to be highly saturated (see Figure 5), while the experimental motor is not. The linearly fitted flux linkage look-up table is plotted in Figure 31.

Then, the look-up table of $\frac{\partial}{\partial\theta}\lambda(\theta, i)$ and $\frac{\partial}{\partial i}\lambda(\theta, i)$ are computed from the fitted look-up table of $\lambda(\theta, i)$ by backward differentiation. Figures 32 and 33 give the plots of the computed $\frac{\partial}{\partial\theta}\lambda(\theta, i)$ and $\frac{\partial}{\partial i}\lambda(\theta, i)$, respectively. Because the linearization of the flux characteristics $\lambda(\theta, i)$, $\frac{\partial}{\partial i}\lambda(\theta, i)$ is simply the inductance $L(\theta)$ which is a function of θ only, as is shown in Figure 33.

To complete the motor model, the stator winding resistance R_s, system inertia J and viscous coefficient B are required. The parameters used in the simulation are

$$\begin{aligned} R_s &= 2.15(\Omega) \\ J &= 2.9e^{-4}(kg \cdot m^2) \\ B &= 6.98e^{-5}(\frac{N-m}{rad/\sec}) \end{aligned}$$

which are the values of the experimental motor obtained in Chapter 4.

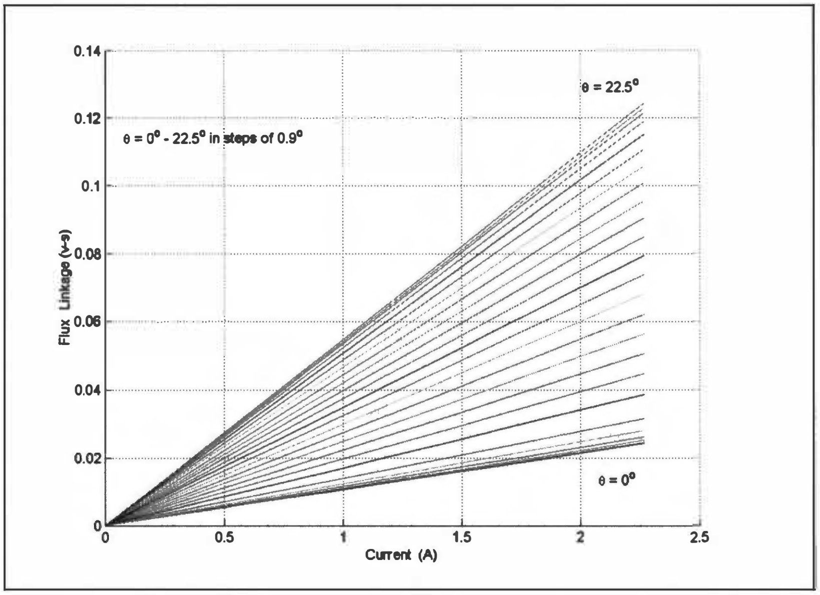

Figure 31. Fitted $\lambda(\theta, i)$ of phase A for $0° \leqslant \theta \leqslant 22.5°$

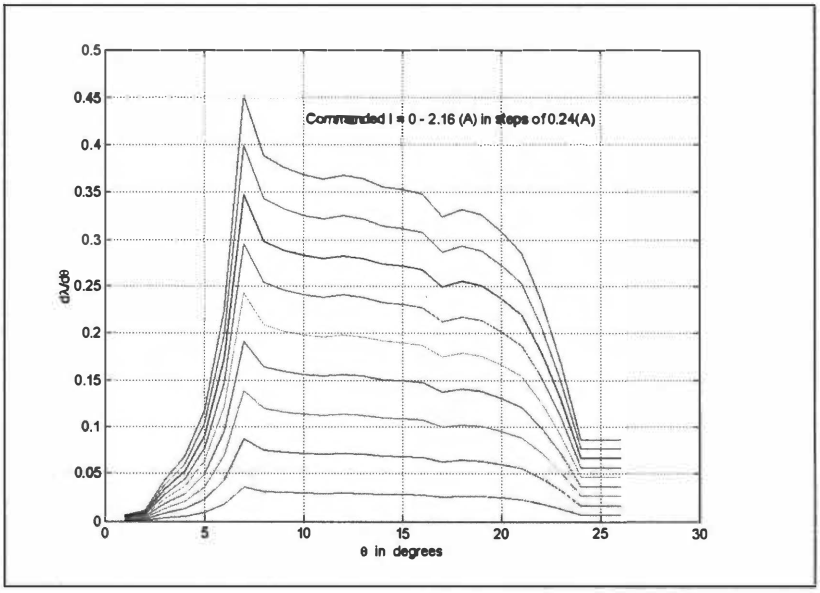

Figure 32. Look-up table of $\frac{\partial}{\partial\theta}\lambda(\theta, i)$ of phase A for $0° \leqslant \theta \leqslant 22.5°$

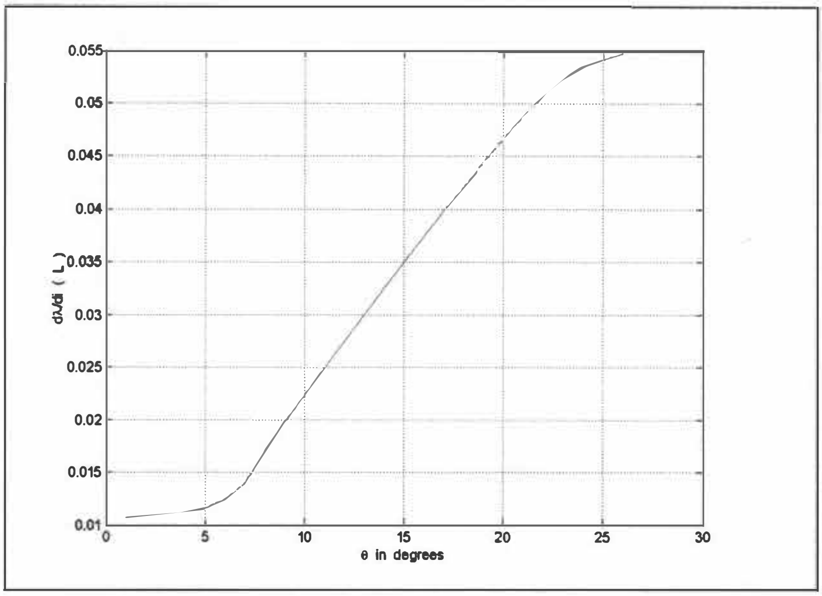

Figure 33. Look-up table of $\frac{\partial}{\partial i}\lambda(\theta, i)$ of phase A for $0° \leqslant \theta \leqslant 22.5°$

With the look-up table for $\tau(\theta, i)$, $\lambda(\theta, i)$, $\frac{\partial}{\partial\theta}\lambda(\theta, i)$, $\frac{\partial}{\partial i}\lambda(\theta, i)$ and the parameters R_s, J, B, the 3-phase 12/8 SR motor model is then constructed as shown in Figure 34. As explained in section 2.2, the expressions for the flux linkages and torques of the different phases are shifted by $\theta_s = 2\pi/(qn_R)(15°$ for the 12/8 SR motor), while the look-up tables calculated above are for phase A only. Therefore, in Figure 34, the absolute rotor position θ from the mechanical equation block that is constructed according to Equation 2.14, is shifted backwards by ϕ and 2ϕ for the phase B and C, respectively, with $\phi = \theta_s$. To use the look-up tables that are computed only for the range $\theta \in [0°, 22.5°]$ for any position , the absolute position θ (shifted for phase B and C) is MOD by 45°. Because $\frac{\partial}{\partial\theta}\lambda(\theta, i)$ and $\frac{\partial}{\partial i}\lambda(\theta, i)$ are even symmetric with respect to $\theta = 22.5°$, if $\theta_{\text{mod}} \leq 22.5°$, it is fed to the look-up tables directly; otherwise, $45^0 - \theta_{\text{mod}}$ is used. The torque profile $\tau(\theta, i)$ is odd symmetric with respect to $\theta = 22.5°$. Therefore, if $\theta_{\text{mod}} > 22.5°$, in addition to inputting $45° - \theta$ to the torque look-up table, the output value of the look-up table $\tau(\theta, i)$ is reversed, as shown in Figure 34.

5.2 Reduced Torque Ripple Controller

To construct the controller proposed in [10], the current manifold $g(\theta, \tau)$ is computed from Figure 26. The commutation angle θ_c as a function of τ^d, $\theta_c(|\tau^d|)$, is obtained from $g(\theta, \tau)$ by Equation 3.29.

Figure 26 shows that the measured maximum torque is $0.45(N-m)$. Therefore, for computing $g(\theta, \tau)$, τ is increased from 0 to $0.45(N-m)$, with step size $0.025(N-m)$. Consequently, the resulting look-up table $g(\theta, \tau)$ is a 18×26 matrix. It is plotted in Figure 35 and Figure 36 in 2-D and 3-D dimensions, respectively.

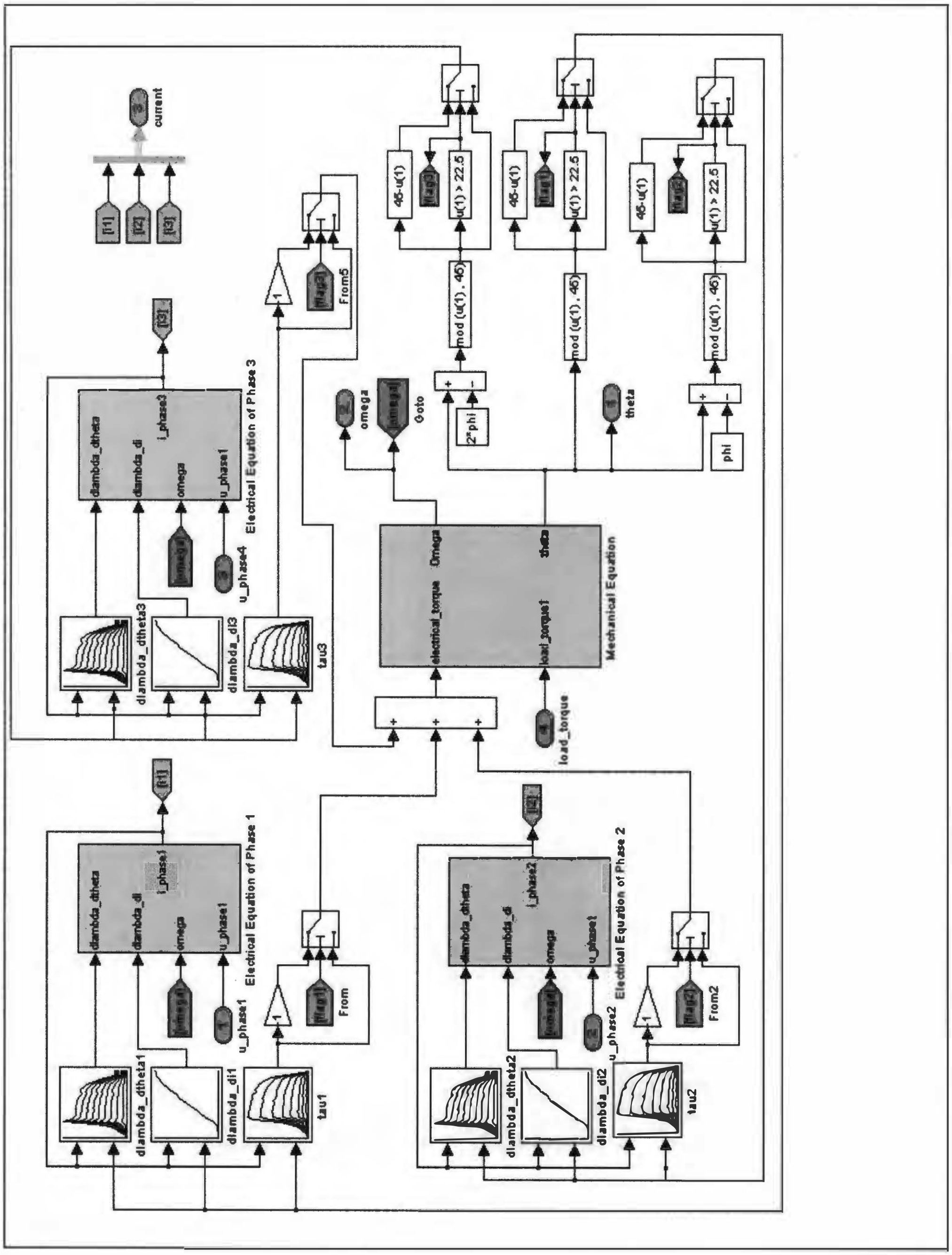

Figure 34. 3-phase 12/8 SR Motor Model

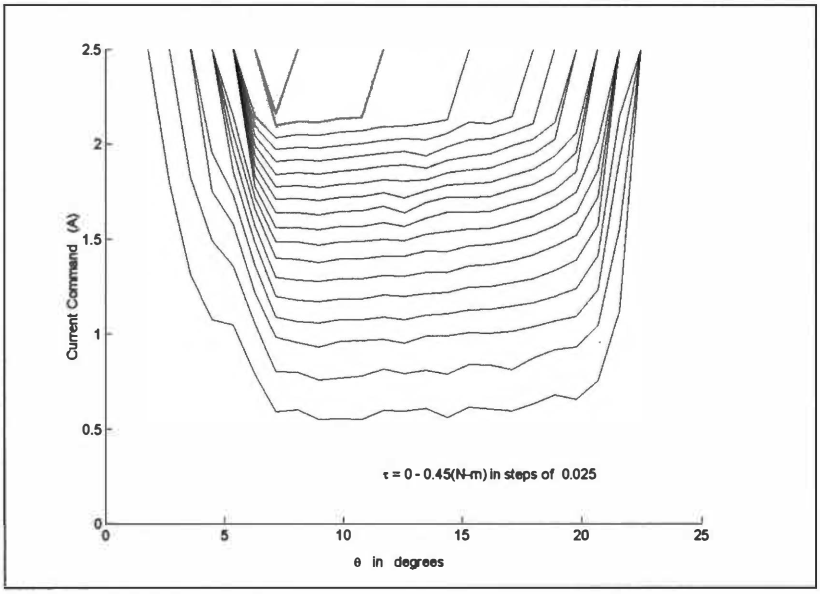

Figure 35. $g(\theta, \tau)$ of Phase A for $0° \leqslant \theta \leqslant 22.5°$ (computerd from the measured $\tau(\theta, i)$)

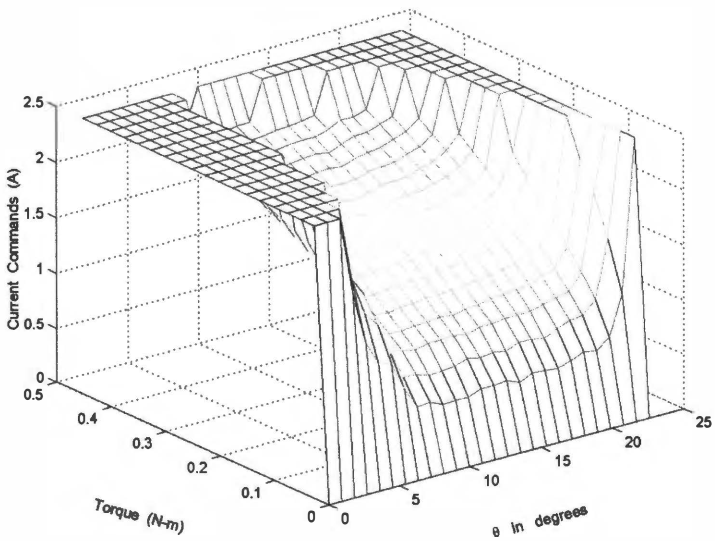

Figure 36. 3D plot of $g(\theta, \tau)$ of phase A for $0° \leqslant \theta \leqslant 22.5°$ (computerd from the measured $\tau(\theta, i)$)

Using $g(\theta,\tau)$, the look-up table for $\theta_c(|\tau|)$ is found by Equation 3.29. This is the third look-up table required by the torque controller. Figure 37 shows the plot.

With the look-up tables for $\tau(\theta,i)$, $g(\theta,\tau)$ and $\theta_c(|\tau^d|)$, the controller is constructed by following the procedure described in section 3.3. Figure 38 shows the Simulink block diagram. In Figure 38, the look-up table for $\theta_c(|\tau^d|)$ is embedded in the *thetac* block whose output θ_c, combined with the rotor position θ and torque command τ^d, is fed to the s,r,f *indices* block. In s,r,f *indices* block, θ_+, θ_- and $\theta_{3\phi}$ are calculated and the *strong, rising* and *falling* phase indices (s,r,f) presented by Equation 3.31 are consequently obtained. The $g(thetac, 1/2tau\_d)$ block calculates the current at commutation point, $i_c = g(\theta_c, \frac{1}{2}\tau^d)$, through its embedded look-up table for $g(\theta,\tau)$. With i_c, the rising current i_R and the falling current i_F are calculated in the *Rising and Falling Phase Currents* block by the procedures presented through Equation 3.32 to Equation 3.35. Then, the rising torque $\tau_r(\theta,i_R)$ and the falling torque $\tau_f(\theta,i_F)$ are obtained through the embedded look-up table for $\tau(\theta,i)$ in the *Rising and Falling Torque* block. Consequently, the *strong* phase current i_S is obtained by Equation 3.36 which is simulated in the *Strong Phase Current* block with the embedded look-up table for $g(\theta,\tau)$. Finally, the rising, falling and strong reference currents, i_R, i_F and i_S are assigned to phase A, B, C in the *Assign Reference Currents to Phases* block according to Equation 3.37.

5.3 Simulation of the Trajectory Tracking Control

To examine the performance of the torque controller constructed in the last section, a trajectory tracking control is simulated using Simulink.

First, a reference trajectory with $(\theta_{ref}(t), \omega_{ref}(t), \alpha_{ref}(t)) = (\int_0^t \omega_{ref}(t), \omega_{ref}(t), \frac{d}{dt}\omega_{ref}(t))$ is preset. The reference speed ω_{ref} is chosen to be a symmetric trajectory given by

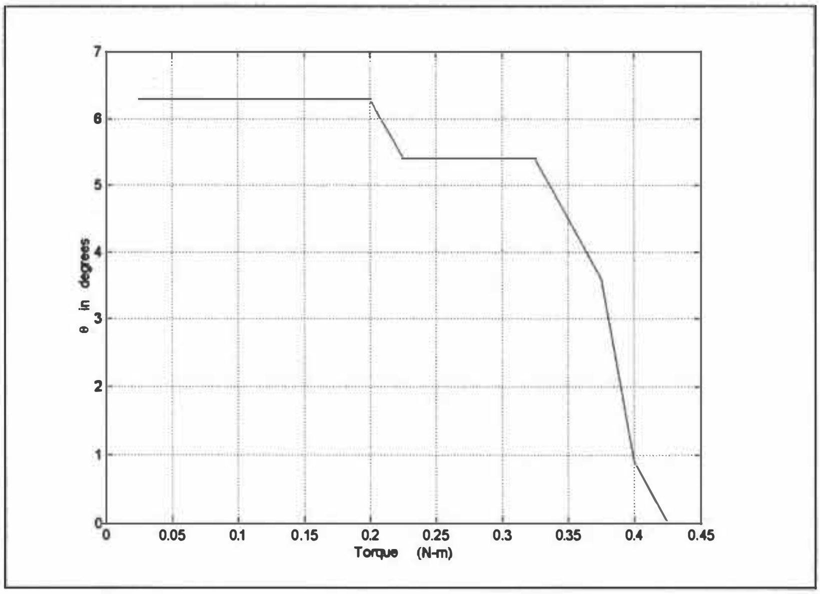

Figure 37. θ_c vs. $|\tau|$

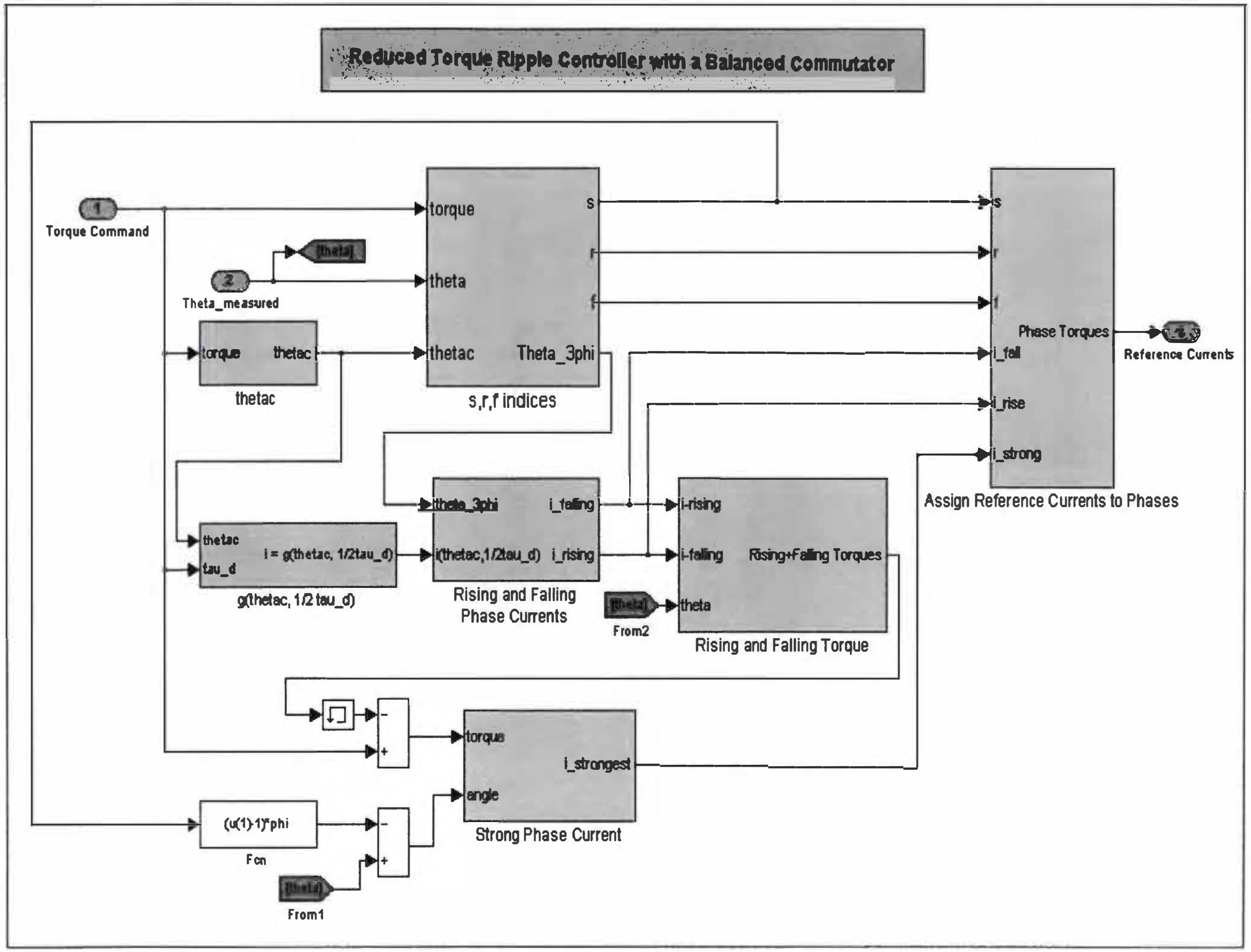

Figure 38. Reduced Torque Ripple Controller

$$\begin{array}{rcll} \omega_{ref}(t) & = & 0 & for \quad 0 \le t \le t_d \\ \omega_{ref}(t) & = & c_1 t^2 + c_2 t^3 & for \quad t_d \le t \le t_1 \\ \omega_{ref}(t) & = & \omega_{\max} & for \quad t_1 \le t \le t_2 \\ \omega_{ref}(t) & = & c_1(t_3 - t)^2 + c_2(t_3 - t)^3 & for \quad t_2 \le t \le t_3 \end{array} \tag{5.40}$$

where t_d, t_1, t_2 and t_3 are indicated in Figure 39 and $t_3 = t_1 + t_2$. The parameter t_d can be arbitrarily set as a time delay, which is useful in experimental implementation of the trajectory tracking, as is discussed in Chapter 6. The coefficients c_1 and c_2 are determined by the conditions

$$\begin{array}{rcl} \omega_{ref}(t_1) & = & \omega_{\max} \\ \dot{\omega}_{ref}(t_1) & = & 0 \end{array}$$

The parameters are given by

$$\begin{array}{rcl} \omega_{max} & = & 50\, rad/\sec. \\ t_1 & = & 0.4 \sec. \\ t_2 & = & 0.5 \sec. \\ t_3 & = & 0.9 \sec. \\ t_d & = & 0.1 \sec. \end{array} \tag{5.41}$$

To track the reference trajectory, a PID feedback controller is employed which is defined by

$$\tau^d(t) = J\left(\int_0^t k_0(\theta_{ref} - \theta)dt + k_1(\theta_{ref} - \theta) + k_2(\omega_{ref} - \omega) + \alpha_{ref}\right) \tag{5.42}$$

where $k_0 = 125000$, $k_1 = 7500$, and $k_2 = 150$.

This PID trajectory tracking function outputs the desired torque τ^d. This desired torque τ^d is then fed into the instantaneous torque controller which computes the reference phase currents i_j^d for each phase.

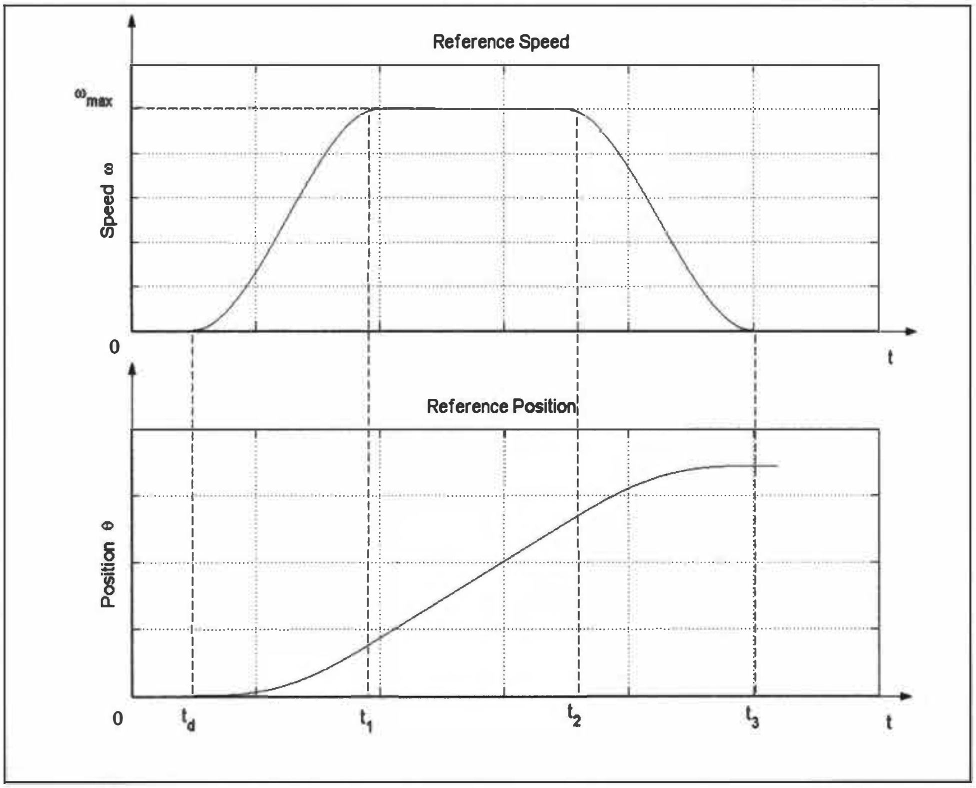

Figure 39. $\omega_{ref}(t)$ and $\theta_{ref}(t)$ VS time in seconds

Finally, the phase voltages v_1,v_2 and v_3 are generated by a high gain feedback controller to track the reference phase currents i_j^d specifically,

$$\begin{aligned} v_1 &= K_P(i_1^d - i_1) \\ v_2 &= K_P(i_2^d - i_2) \\ v_3 &= K_P(i_3^d - i_3) \end{aligned}$$

where $K_P = 1000$ and $j = 1, 2, 3$ represents phase A, B, C, respectively.

Figure 40 shows the top level of the Simulink block diagram for the trajectory tracking simulation.

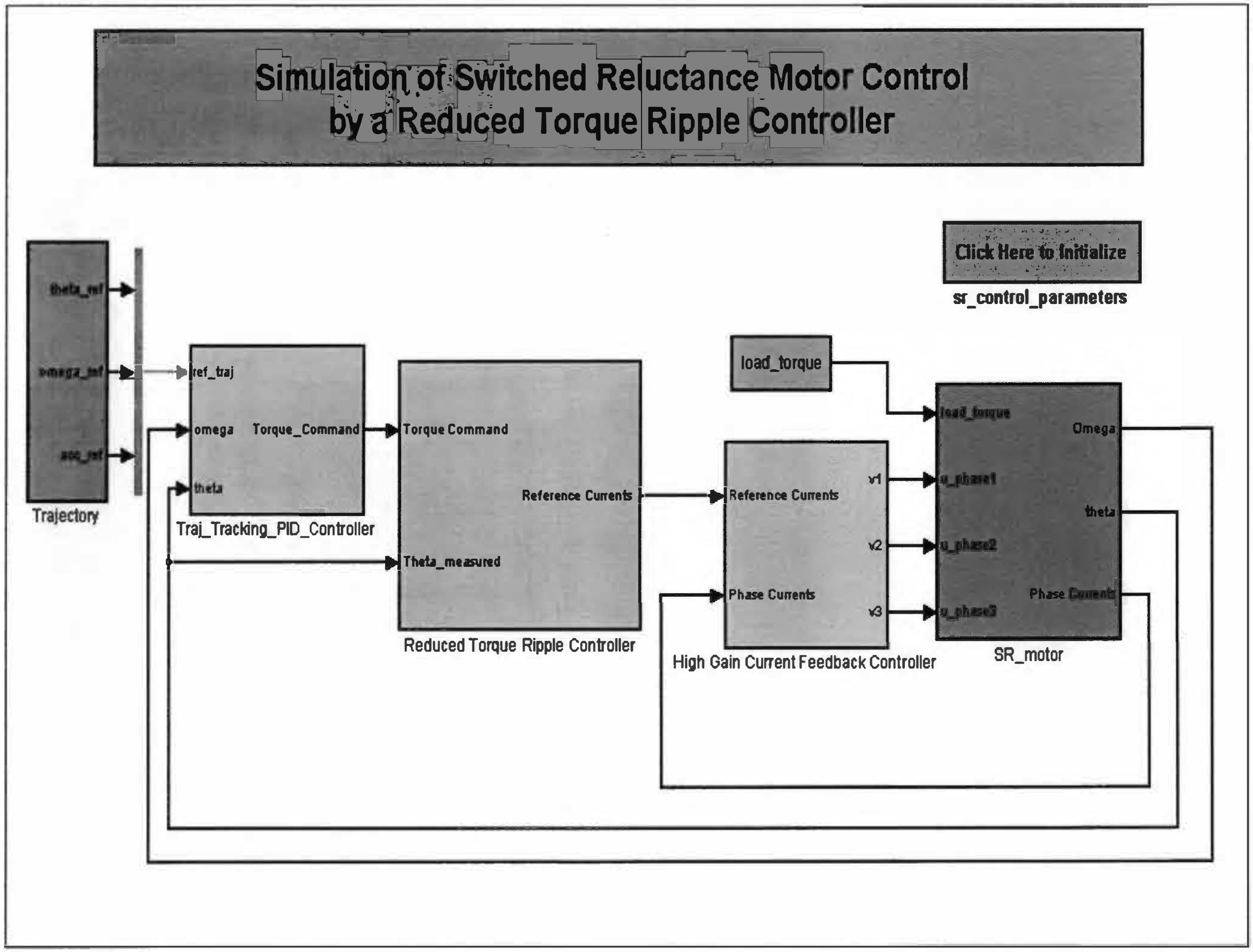

Figure 40. Simulation of Trajectory Tracking Control

5.4 Simulation Results

The simulation shows excellent tracking performance of the reduced torque ripple control, as shown in the top plots of Figure 41 and Figure 42, respectively. The tracking errors are small enough that they are not discernible in the plots. The biggest error of the position tracking and the speed tracking are 2.82×10^{-3} $radians$ and 0.14 rad/s as is shown in the bottom plots of Figure 41 and Figure 42, respectively.

This trajectory tracking performance is achieved by good current tracking performance of the high gain current feedback controller (see Figure 40) and the reduced torque ripple controller. Only the reference current for each phase that is generated by the reduced torque ripple controller can be tracked accurately, can the performance of the trajectory tracking be proved. Figure 43 shows the current tracking result in the simulation. In Figure 43, plot (a) shows the three phase currents of the SR motor model. Plot (b) is a zoomed view of one period of plot (a) to illustrate the current commutation of the three stator phases. In (c), the commanded current and the actual current in phase A are plotted together. Again, the error is small enough that it is not discernible in plot (c). The corresponding tracking error was plotted in (d). The biggest spike of the current tracking in (d) is 0.18 A.

5.5 Torque Ripple Analysis

The trajectory tracking simulation is not suitable for torque ripple analysis because the commanded torque τ^d (output of the *Traj_Tracking_PID_Controller* block in Figure 40) is varying itself when tracking the reference trajectory. Therefore, to assess the torque ripple numerically, instead of the trajectory tracking control, a constant torque command $\tau^d = 0.15\ N-m$ is tracked by the constructed reduced torque ripple controller. In this simulation, referring to Figure 40, the *Trajectory* block and the *Traj_Tracking_PID Controller* block are taken out, and a constant torque command $\tau^d = 0.15\ N-m$ is fed into the *Reduced Torque Ripple Controller* block directly. By adjusting the load torque, the motor speed is controlled to reach a steady-state. The output torque is reconstructed by feeding the phase currents in the motor model and rotor position into the look-up table of the look-up table of $\tau(\theta, i)$ in real time.

Figure 44 plots the reconstructed torque. The average value of the reconstructed torque is 0.149 $N-m$. The average shaft speed is 20.63 rad/sec. The torque ripple is calculated by two different methods. Method I uses the following formula

$$\tau_{ripple} = \frac{1}{\tau^d(t_2 - t_1)} \int_{t_1}^{t_2} |\tau - \tau^d| d\tau$$

where $t_2 - t_1$ is the interval in which the motor reaches steady-state. Here, t_1 and t_2 are chosen to be 1.2 and 1.4 seconds, respectively.

The calculated torque ripple τ_{ripple} is 1.34%.

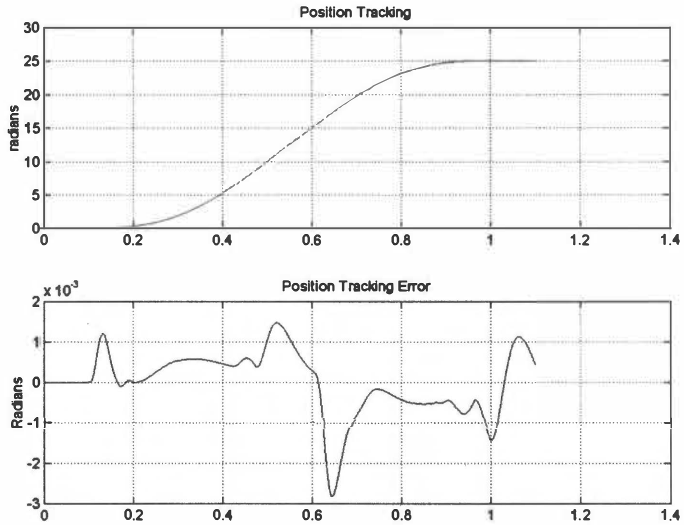

Figure 41. $\theta(t)$ and $\theta_{ref}(t) - \theta(t)$ VS time in seconds

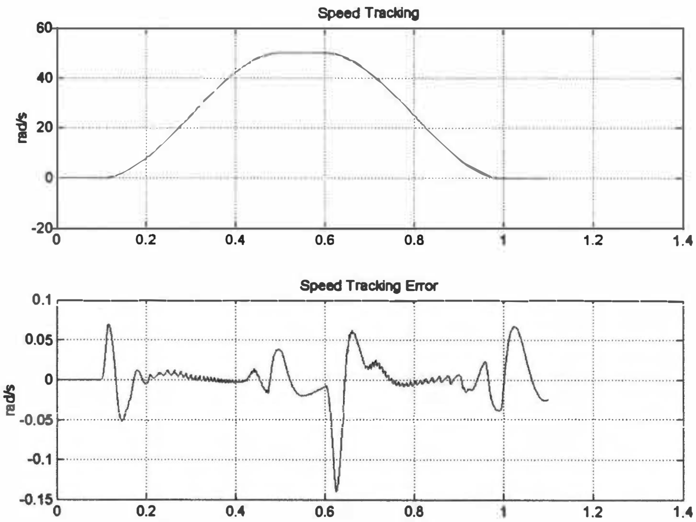

Figure 42. $\omega(t)$ and $\omega_{ref}(t) - \omega(t)$ VS time in seconds

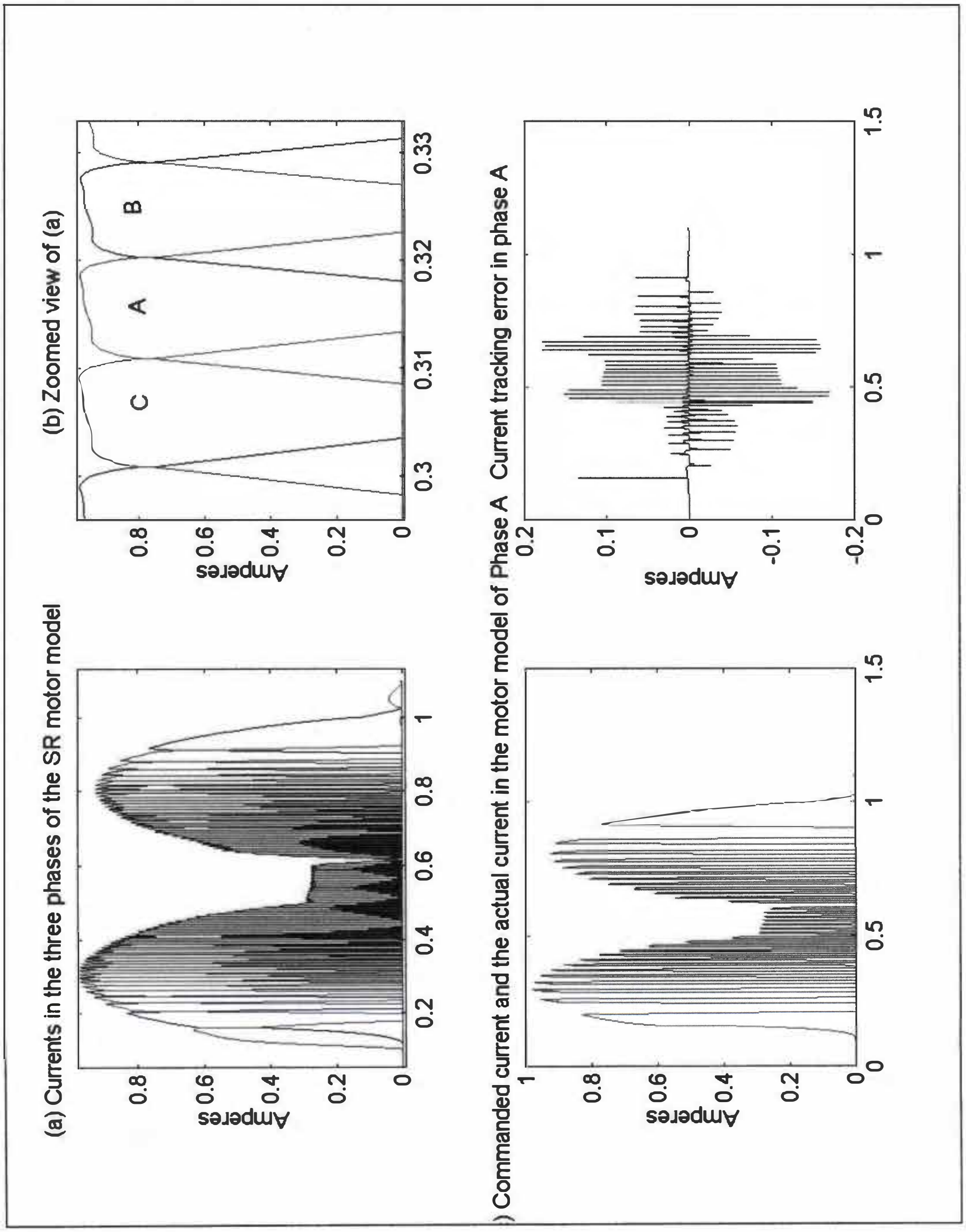

Figure 43. Simulation result of the reference current tracking: (a) i_a,i_b,i_c VS time in seconds (b) i_a,i_b,i_c VS time in seconds (c) $i_a(t)$,$i_{ac}(t)$ VS time in seconds (d) $i_a(t) - i_{ac}(t)$ VS time in seconds

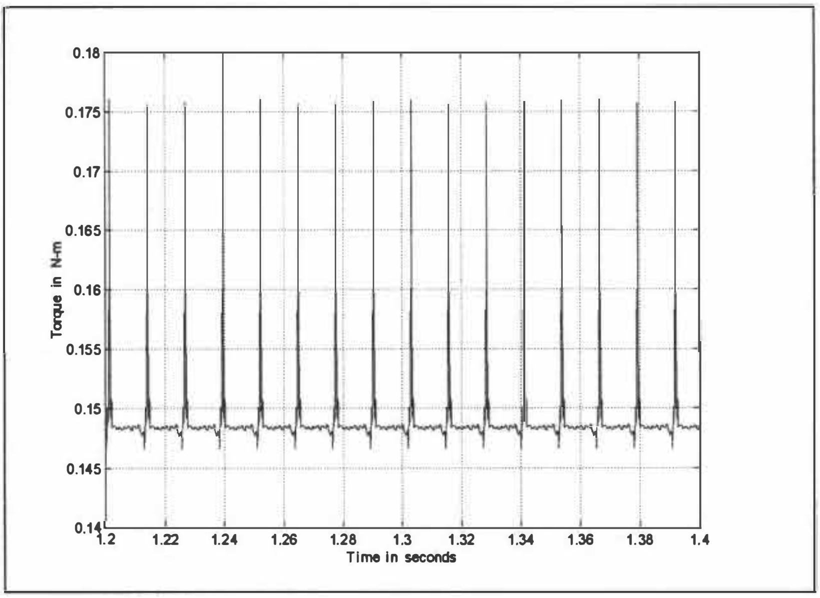

Figure 44. Simulation of tracking of a constant torque command by the reduced torque ripple controller

Method II is introduced in [10] which calculates the torque ripple through the motor speed ripple.

For a commanded constant torque τ^d, define period $T = \phi/\omega_0$, where $\phi = 2\pi/qn_R$ is the step angle and ω_0 is the average speed when the motor reach steady-state.

With system inertia J, fluctuations in speed are given by

$$\omega(t_2) - \omega(t_1) = \frac{1}{J}\int_{t_1}^{t_2} (\tau(t) - \tau_0)dt$$

Then, define the torque ripple index as

$$\tau^* = \frac{1}{\tau_0 T}\int_T |\tau(t) - \tau_0|dt$$

By selecting time interval (t_1, t_2) in which the torque ripple is positive and time interval $(t_2, t_1 + T)$ in which the torque ripple is negative, τ^* can be rewritten as

$$\tau^* = \frac{1}{\tau_0 T}\int_{t_1}^{t_1+T} |\tau(t) - \tau_0|dt = \frac{\omega_0}{\phi\tau_0}\left(\int_{t_1}^{t_2} (\tau(t) - \tau_0)dt - \int_{t_2}^{t_1+T} (\tau(t) - \tau_0)dt\right) = \frac{2J\omega_0}{\phi\tau_0}(\omega_{\max} - \omega_{\min})$$

The calculated torque ripple index τ^* (the symbol τ^* is used to distinguish it from the torque ripple calculated by the first method which is donated as τ_{ripple}) is 0.85%. Figure 45 gives the recorded speed ripple.

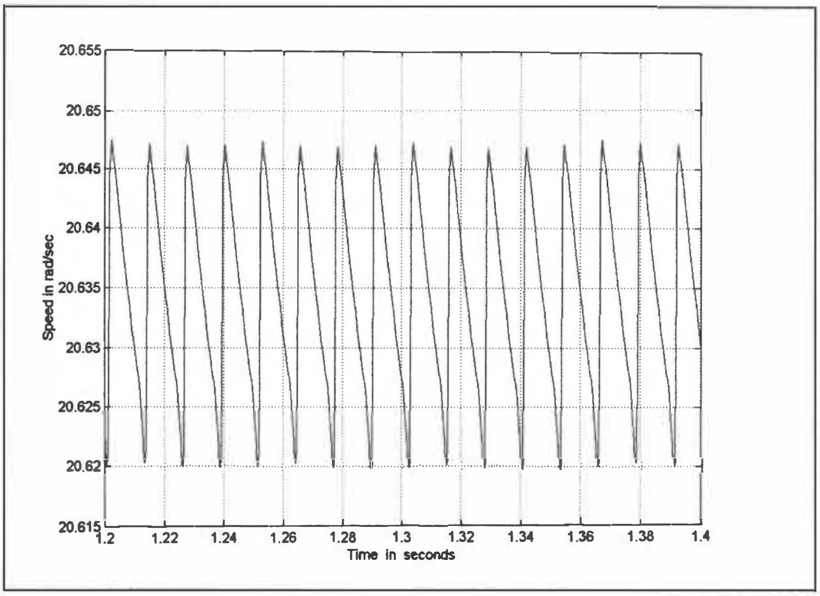

Figure 45. Speed ripple of simulation of tracking a constant torque command by the reduced torque ripple controller

Figure 46 plots the current of phase A in the motor model and its reference current versus time and their difference, respectively.

As a comparison, the square wave control method described in section 3.1 is used to track the constant torque command in the same simulation environment as a comparison. The square wave torque lookup table shown in Figure 47 is derived from the obtained torque profile $\tau(\theta, i)$ by setting the amplitude of the square wave for each current the average value of the measured torque at that current. The commutation angle is fixed as $\theta_c = 3.6°$.

Keeping all the simulation settings the same except that the obtained look-up table of the torque profile $\tau(\theta, i)$ is substituted by the square wave look-up table, the above simulation is repeated. Figure 48 and Figure 49 plot the torque ripple and the current tracking results, respectively. Figure 50 plots the recorded speed ripple. The motor speed is 20.62 rad/sec..The calculated torque ripple τ_{ripple} is 0.77% and the calculated torque ripple index τ^* is 0.34%.

The simulation results show that the square wave control method even has lower torque ripple than the reduced torque ripple control method. The reason is due to the current tracking performance. Comparing Figure 46 and Figure 49, one can see that the peak tracking error of the reduced torque ripple control method is about 32 times that of the square wave control method.

The simulation results indicate that the performance of the current command tracking effects the torque ripple of the SR motor substantially. Poor current tracking performance would even impair the advantage of the constructed reduced torque ripple controller totally.

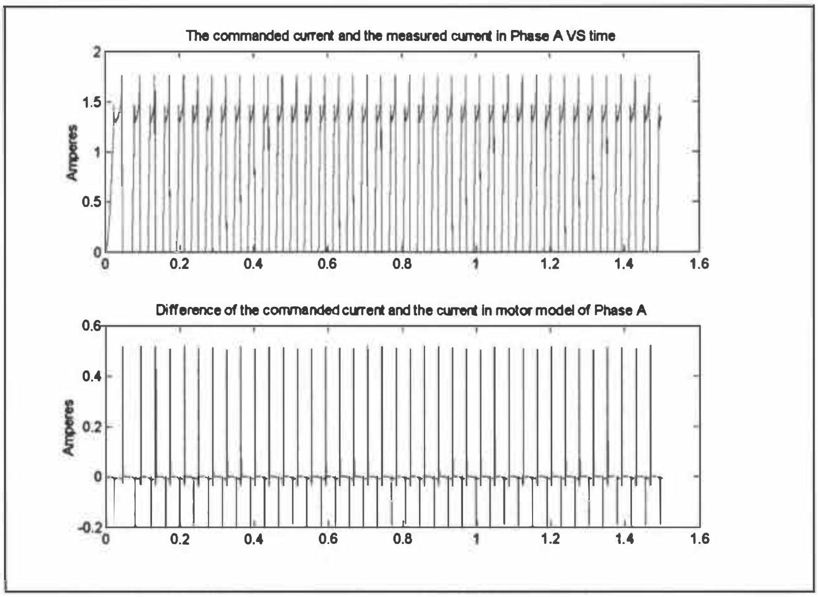

Figure 46. Current tracking of simulation of tracking a constant torque command by the reduced torque ripple controller

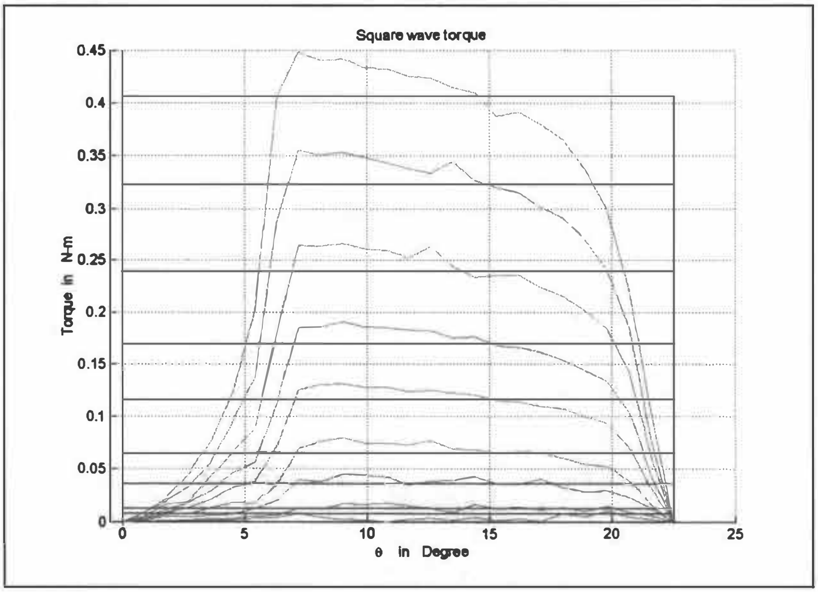

Figure 47. Square wave reference current

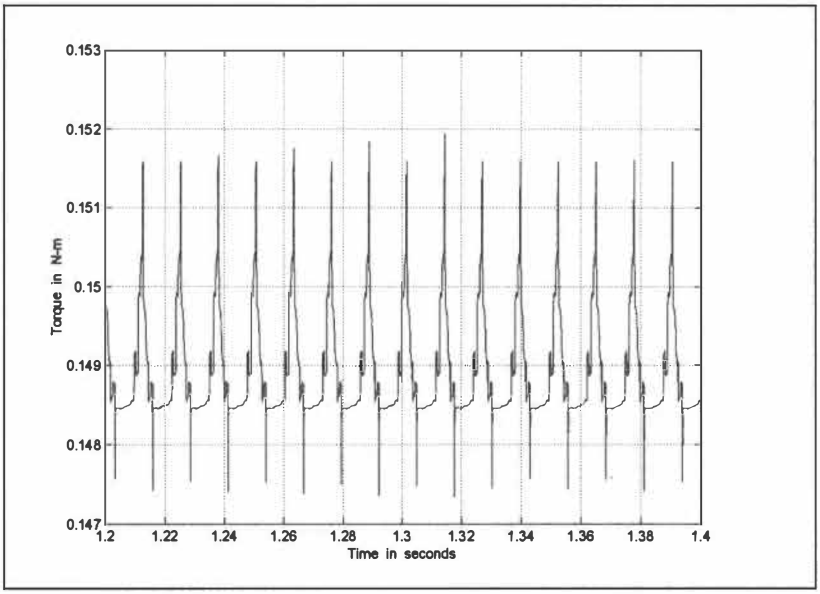

Figure 48. Simulation of tracking of a constant torque command by the square wave excitation

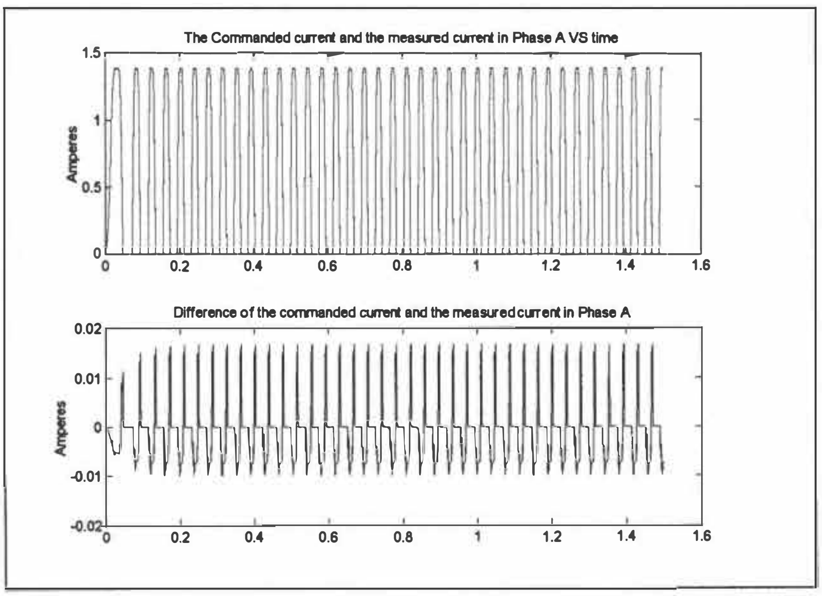

Figure 49. Current tracking of simulation of tracking a constant torque command by the square wave excitation

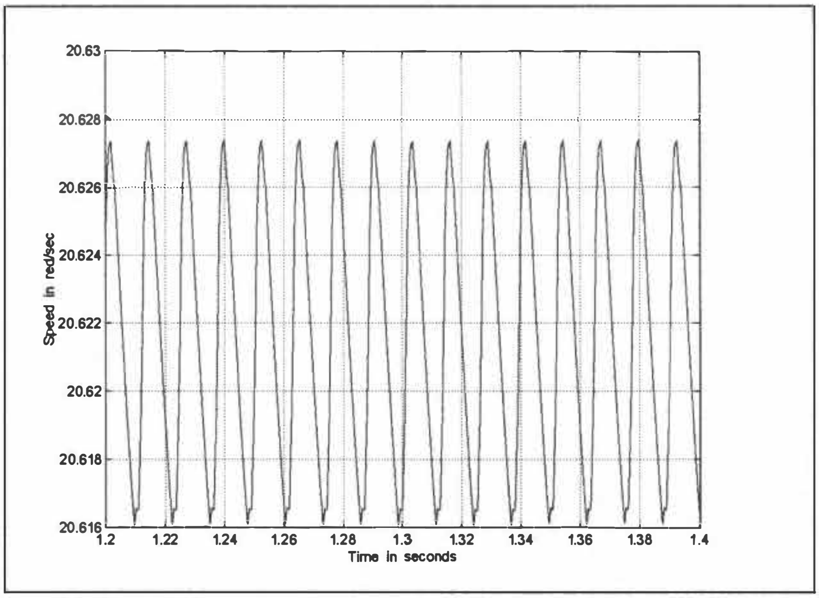

Figure 50. Speed ripple of simulation of tracking a constant torque command by the square wave excitation

Chapter 6
Implementation of the Reduced Torque Ripple Control

In this chapter, the reduced torque ripple controller is implemented through the real-time control platform described in section 4.1. The experimental SR motor that is tested in Chapter 4 is controlled by this implemented controller and a trajectory tracking control experiment is done. Also, constant torque command tracking experiment is done to assess the torque ripple numerically. For these two experiments, square wave control method described in section 3.1 is also implemented as a comparison.

Section 6.1 describes the implementation procedure of the trajectory tracking control. The experiment results are presented in section 6.2.

In section 6.3, a constant torque command is tracked by both the reduced torque ripple controller and the square wave torque controller. Torque ripples are calculated separately and compared.

6.1 Implementation of the Trajectory Tracking Control

To implement the reduced torque ripple controller through the real-time control platform, the motor model block *SR_motor* in Figure 40 is taken out. The A/D, D/A and encoder icons are inserted into the Simulink diagram to integrate the controller with the hardware. Figure 51 shows the top level of the Simulink block diagram for the implementation.

In Figure 51, the *Trajectory* block generates a reference trajectory which is defined by Equation 5.40 (see Figure 39), with the parameters given by

$$\begin{aligned} \omega_{max} &= 50\, rad/\sec. \\ t_1 &= 2 \sec. \\ t_2 &= 6 \sec. \\ t_3 &= 8 \sec. \\ t_d &= 1 \sec. \end{aligned} \tag{6.43}$$

A PID feedback controller is used to track the reference trajectory, which is defined by Equation 5.42. It is embedded in the *Traj_Tracking_PID_Controller* block. The resulting torque command τ^d is fed into the *Reduced Torque Ripple Controller* block that has been updated with the experimental data. The resulting reference currents are then sent out to the D/A module directly through the I/O icon *OpIP230-8AnalogOut* provided by RTLAB as is shown in Figure 51. The three BA-series amplifiers connected to the SR motor receive the reference current commands from the D/A module and undertake the task of current tracking .

The shaft position is detected by the encoder mounted on the load motor. The encoder signal is read into the control blocks through the icon *Opquad_Decoder*, which represents the position in counts with 4000 counts per revolution. The rotor speed is then computed by the difference equation $\omega_{ref}(nT_s) = [\theta(nT_s) - \theta((n-1)T_s)]/T_s$. The sample time T_s is set to be 0.001 sec.

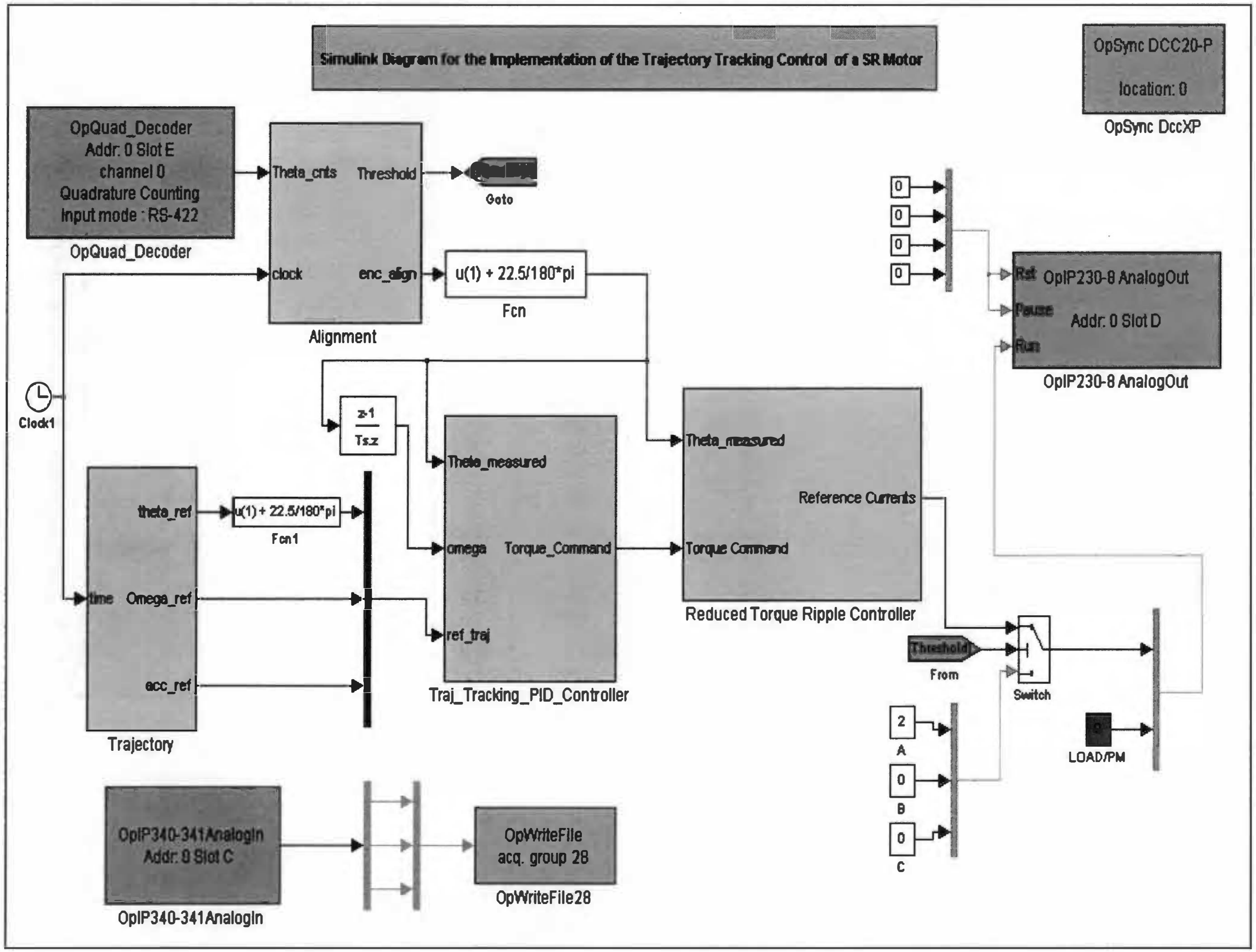

Figure 51. Simulink Diagram for the Implementaion of the Trajectory Tracking Control

As discussed in section 4.2, the aligned position for phase A is chosen to be the starting position. To achieve this, the starting of the trajectory is delayed by t_d. During the delay, 2 amperes are commanded to phase A to force the rotor to align with it, as is shown in Figure 51. The internal signal *Threshold* changes from 0 to 1 when the delay ends, which switches the current commands from the alignment status (2 amperes in phase A) to the trajectory tracking status (current references generated by the Reduced Torque Ripple Controller). The *Alignment* block resets the encoder to zero when the trajectory starts and sends out the internal signal *Threshold* to switch the current commands.

According to the convention used for all the equations and look-up tables in this thesis, the unaligned position for phase A is defined to be 0°. Consequently, the starting position chosen in the last paragraph is 22.5° using this convention. Therefore, the position signal that comes from the $Alignment$ block after the delay times $t_{d,}$ is set to be 22.5°. As a result, the reference position starts from 22.5° too, instead of 0°.

The $OpIP340 - 341AnalogIn$ icon represents the A/D module, which reads in the phase current measured by the current transducers. The data is saved in real time on the target PC through the storage icon $OpWriteFile$.

The whole program is synchronized by the timer module installed on the target PC. By inserting the *OpSync Dccxp* icon in the Simulink block diagram, the timer module is activated. In the experiment, the computing step size of the whole trajectory tracking program is set to be $200\mu s$.

6.2 Experiment Results

The measured data of the trajectory tracking is shown in Figure 52 and Figure 53. In Figure 52, the starting position value 22.5° was deducted from both the measured position and its reference. The error of the position tracking is small enough that it is not discernible in the plot. Figure 54 plots the position tracking error separately. The largest error is 0.075 $radians$. Figure 53 plots the actual speed which was computed by backward differentiation of the measured positions. The granularity in the calculated speed is simply due to the resolution of the encoder which is $4000/rev$.

As shown in Figure 52 and Figure 53, the performance of the experimental position and speed tracking demonstrates the capability of the SR motor being used for servo systems. However, the experimental position tracking error is 0.075 $radians$ which is much bigger than the simulation result, 0.0028 $radians$. Also, the maximum speed of the speed trajectory could not be set bigger than 50 $rad/\sec$ in the experiment due to the ability of the amplifiers in tracking the commanded currents. The reason of the bigger position tracking error and tracking speed limit is due to the unsatisfying reference current tracking in the experiment. As described in section 4.1, the current tracking in the experiment is done by three amplifiers which regulate the phase currents through its built-in current feedback controller. Therefore, one has no direct control on the phase currents. The current tracking performance is only determined by the tracking ability of the amplifier.

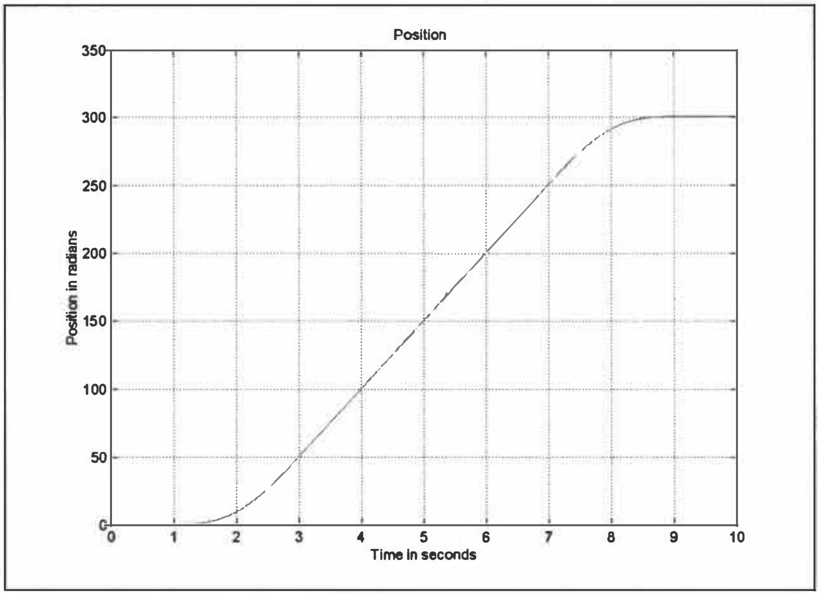

Figure 52. Experimental result of the position tracking by the reduced torque ripple controller

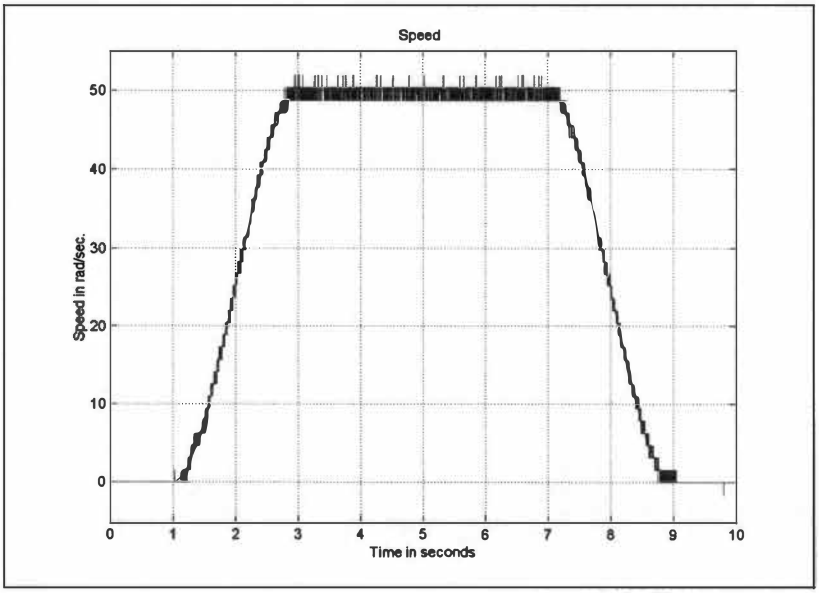

Figure 53. Experimental result of the speed tracking by the reduced torque ripple controller

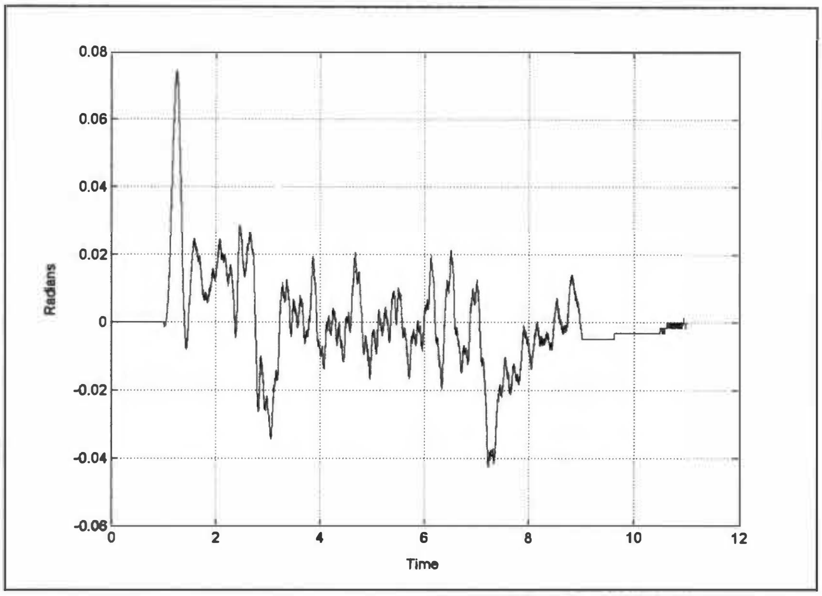

Figure 54. Position error of the trajectory tracking experiment by the reduced torque ripple controller

The BA series amplifiers used in the experiment are PWM inverters with a switching frequency $20KHz$. The rated tracking bandwidth is $2KHz$. However, the recorded data show that the tracking bandwidth is far below the rated frequency. The non-sinusoidal reference current could be the reason of the degradation of the tracking bandwidth of such general purpose amplifiers. Figure 55 and Figure 56 show the recorded current tracking data at speed of 50 $rad/\sec$ and 75 $rad/\sec$, respectively (The speed 75 $rad/\sec$ is achieved by commanding a constant torque into the *Reducec Torque Ripple Controller* block in Figure 51, instead of doing trajectory tracking control).

In Figure 55, the frequency of the reference current is 66.6 Hz. One can see that the tracking current in Figure 55 is much worse than the simulation result, which was plotted in Figure 43. First, considerable phase lagging is observed. Second, the current could not be regulated to zero quickly, but has high magnitude oscillations. Because the reference current is generated for different positions to produce desired torque, current phase lagging will result in inaccurate torque production. The oscillations that occurs when the reference current goes to zero will produce unwanted torque, which introduces unpredictable torque components, hence impairs the trajectory tracking performance.

Figure 56 plots the data recorded for a constant torque command where the speed was 75 rad/sec. The corresponding reference current frequency is $100Hz$. Heavier phase lagging and oscillations at zero current are shown in Figure 56 due to the high frequency. The poor performance of the current tracking resulted in the failure of the trajectory tracking control at this speed.

As a comparison, the same trajectory reference is tracked by the square wave excitation control method. The square wave controller is implemented using the same Simulink diagram shown in Figure 51 except that the look-up table of $\tau(\theta, i)$ is the square wave shown in Figure 47 and the commutation angle is 3.6° fixed.

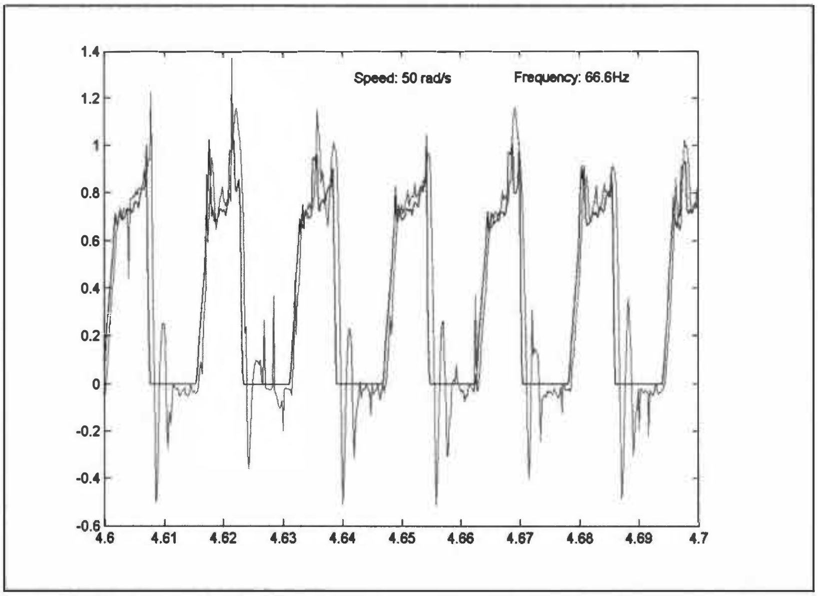

Figure 55. Reference current tracking at speed of 50 rad/sec by the reduced torque ripple controller

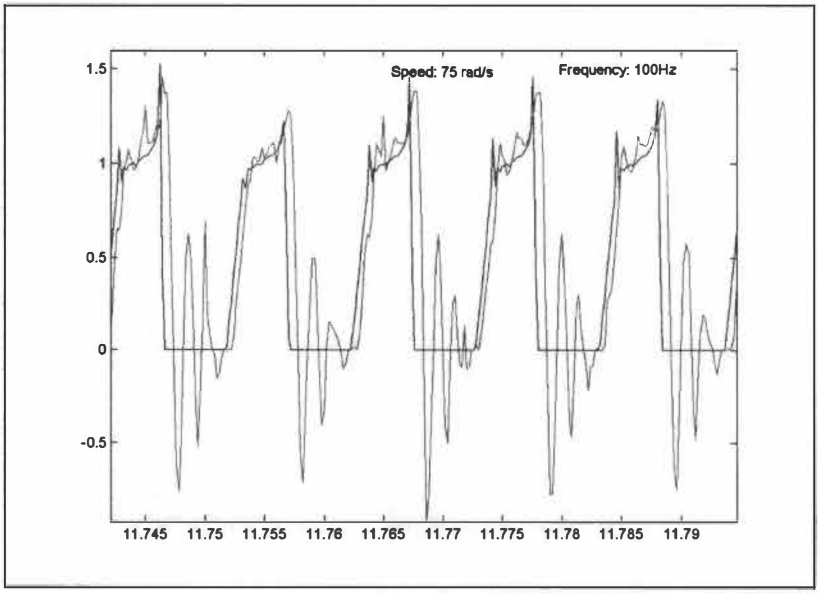

Figure 56. Reference current tracking at speed of 75 $rad/$ sec by the reduced torque ripple controller

The measured data of the trajectory tracking is shown in Figure 57 and Figure 58. The error of the position tracking is plotted in Figure 59. The largest error is 0.175 $radians$ which is more than two times the value 0.075 $radians$ indicated in Figure 54. Figure 58 plots the actual speed which was computed by backward differentiation of the measured positions. Comparing Figure 53 and Figure 58, one can see that the tracking performance of the reduced torque ripple controller is better than the square wave torque controller.

6.3 Torque Ripple Analysis

To assess the torque ripple numerically, as is done in the simulations in Chapter 6, a constant torque command $\tau^d = 0.15\ N - m$ is fed into the *Reduced Torque Ripple Controller* block in Figure 51 directly. By using the PM synchronous motor to add load torque on the shaft (see Figure 23), the shaft speed is controlled to reach a steady-state. The speed is controlled to be lower than 50 rad/sec so that the phase currents tracking performance is prevented from being intolerable (refer to the previous section). The actual torque is reconstructed by feeding the phase currents and rotor position into the look-up table of the torque profile $\tau(\theta, i)$ in real time because the torque transducer is not available for the experiment. Figure 60 plots the reconstructed torque. The average value of the reconstructed torque is $0.17\ N - m$. The average shaft speed is $20.2\ rad/sec$. The torque ripple calculated using method I is $\tau_{ripple} = 29.46\%$. The torque ripple index calculated using method II is $\tau^* = 234.4\%$. The shaft speed is calculated from the recorded position data by backward differentiation. Figure 61 and Figure 62 give the calculated speed and its zoomed view, respectively.

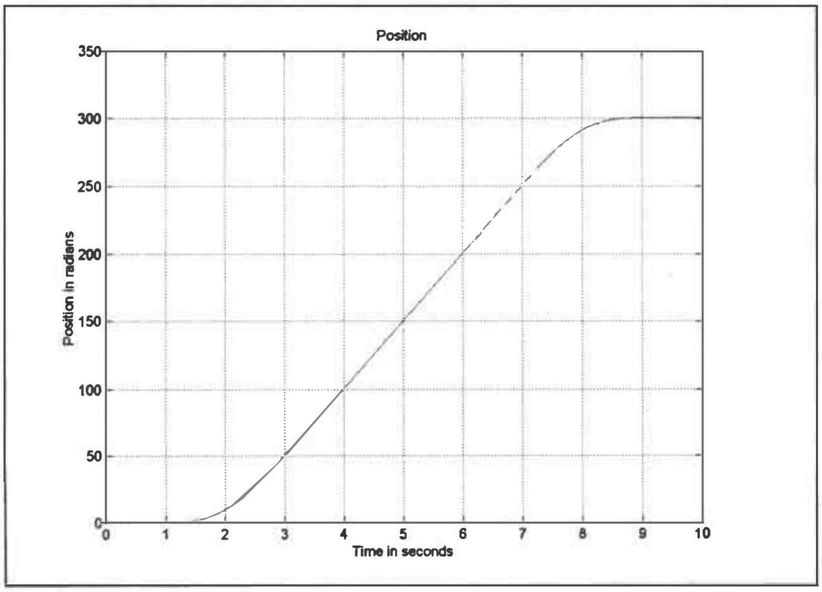

Figure 57. Experimental result of the position tracking by the square wave excitation

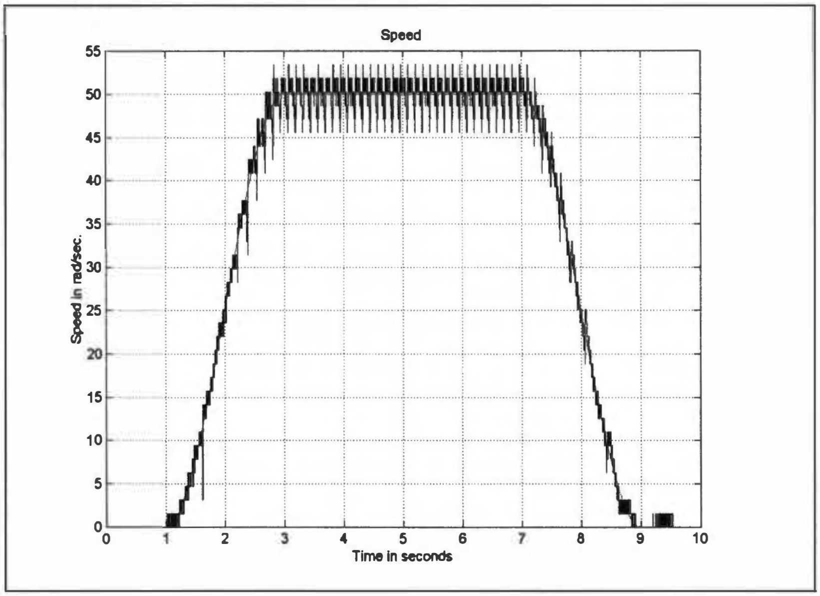

Figure 58. Experimental result of the speed tracking by the square wave excitation

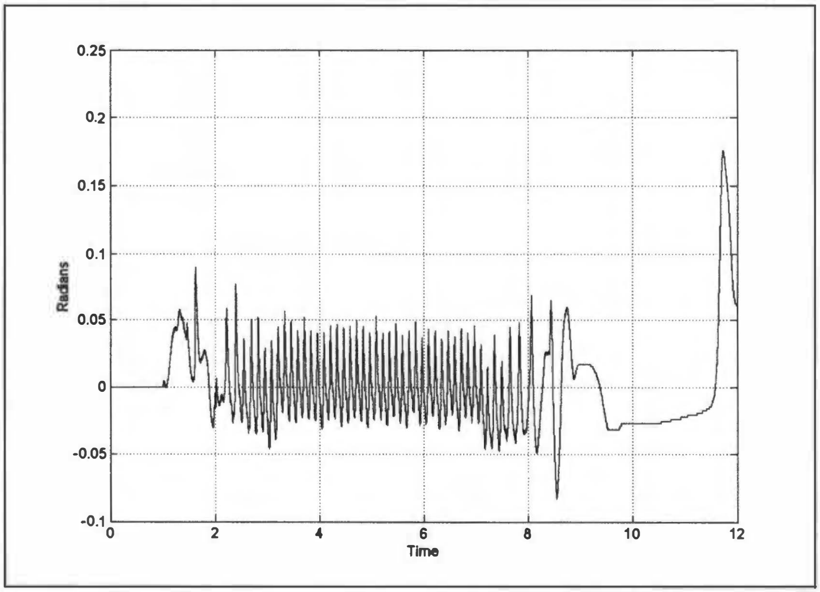

Figure 59. Position error of the position tracking by the square wave excitation

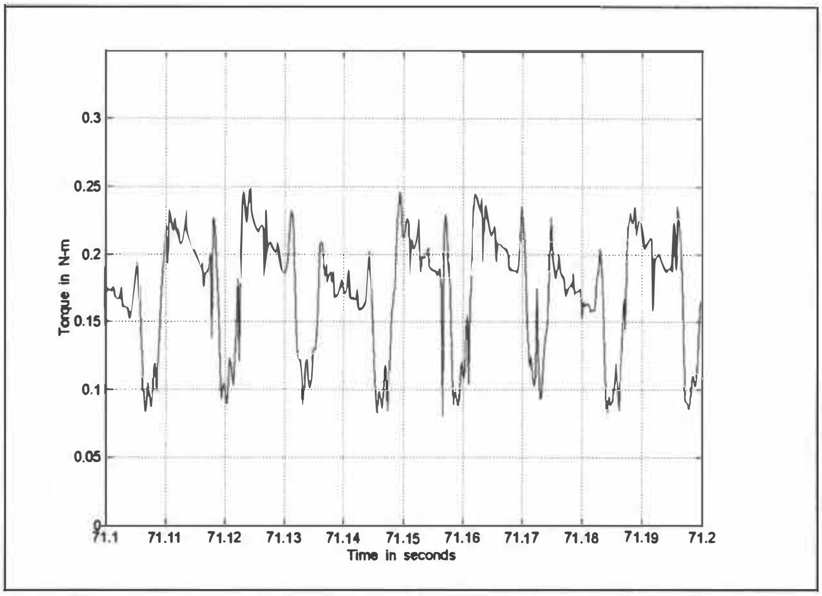

Figure 60. Tracking of a constant torque command by the reduced torque ripple controller

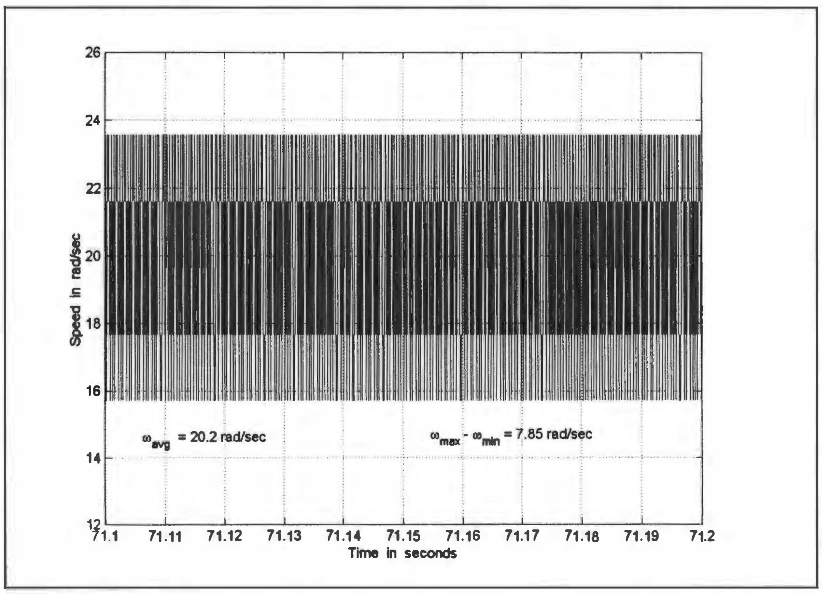

Figure 61. Calculated shaft speed from the recorded position data by back differentiation (under reduced torque ripple control)

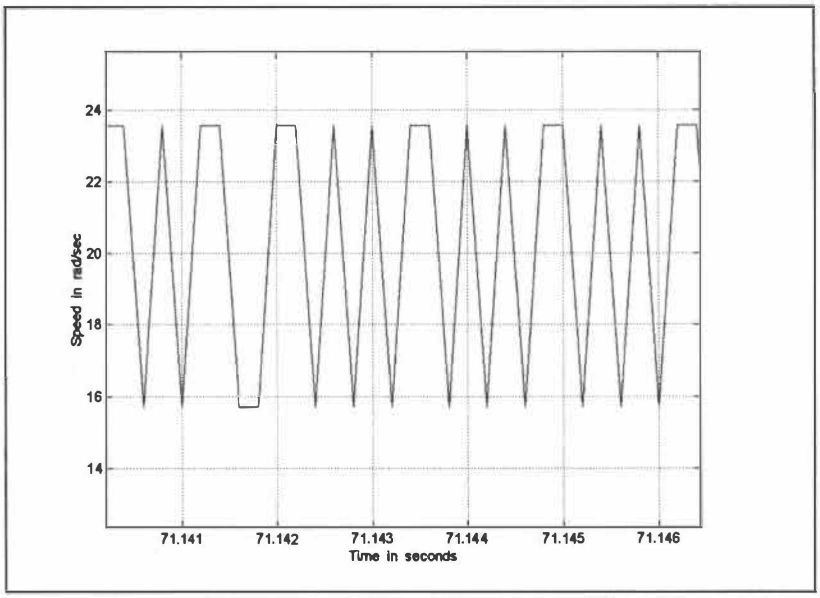

Figure 62. Zoomed view of the calculated shaft speed from the recorded position data by back differentiation (under reduced torque ripple control)

Keeping all the experimental settings the same except that the *Reduced Torque Ripple Controller* block in Figure 51 is replaced by the square wave torque controller, the experiment was repeated. Figure 63 plots the reconstructed torque under the square wave torque control. The average value of the reconstructed torque is 0.18 $N-m$. The average shaft speed is 21.1 rad/sec. Figure 64 and Figure 65 give the calculated speed and its zoomed view, respectively. The torque ripple calculated using method I is $\tau_{ripple} = 31.1\%$. The calculated torque ripple index using method II is $\tau^* = 244.7\%$.

The fluctuations of the calculated speeds shown in Figures 62 and 65 are due to the errors of the position sensor and backward differentiation. Therefore, the torque ripples calculated using the method II may not reflect the actual torque ripple. The values of τ^* are presented only for the purpose of documentation.

The performance of the current tracking is the main reason that the torque ripples are higher in the experiments than in the simulations for both the reduced torque ripple controller and the square wave controller. Figures 66 and 67 plot the measured current of phase A and the reference current of phase A for the reduced torque ripple controller and the square wave torque controller, respectively. Comparing them with Figure 46 and 49, one can see that substantial steady-state error and phase delay exist in the experimental current tracking.

On the other hand, under the similar current tracking performance in the experiments (comparing Figure 66 and Figure 67), the torque ripple of the reduced torque ripple controller is also similar to that of the square wave torque controller (no substantial torque ripple reduction is observed). In other words, the torque reduction of the reduced torque ripple controller is not distinct when the tracking of the reference current is poor.

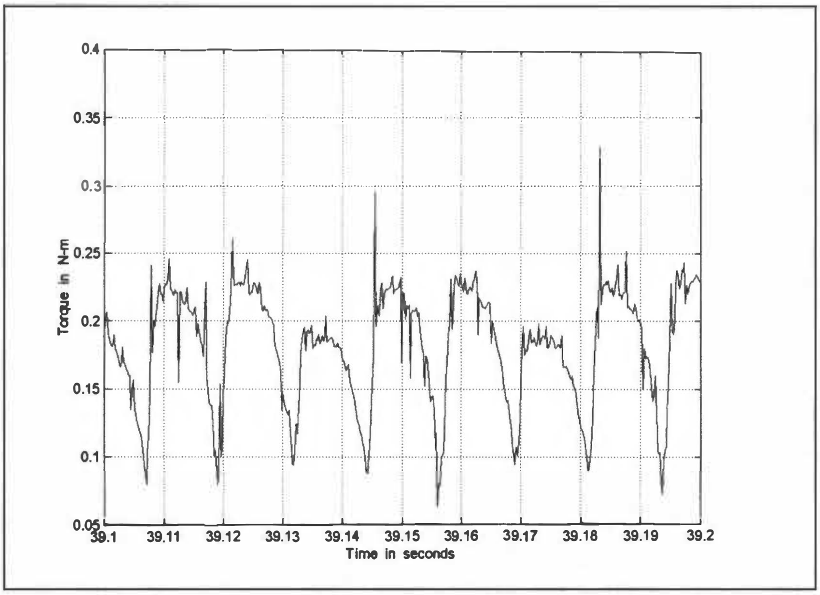

Figure 63. Tracking of a constant torque command by the square wave excitation

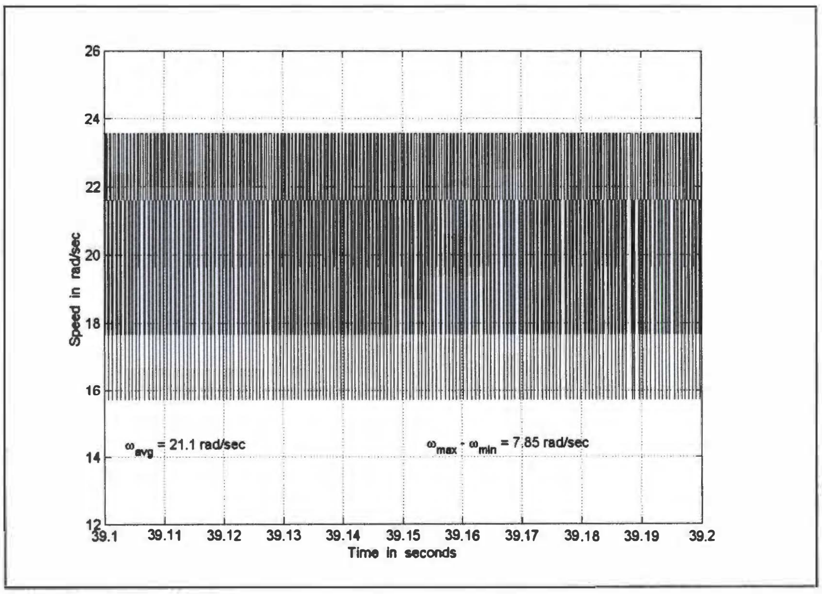

Figure 64. Calculated shaft speed from the recorded position data by back differentiation (under square wave excitation)

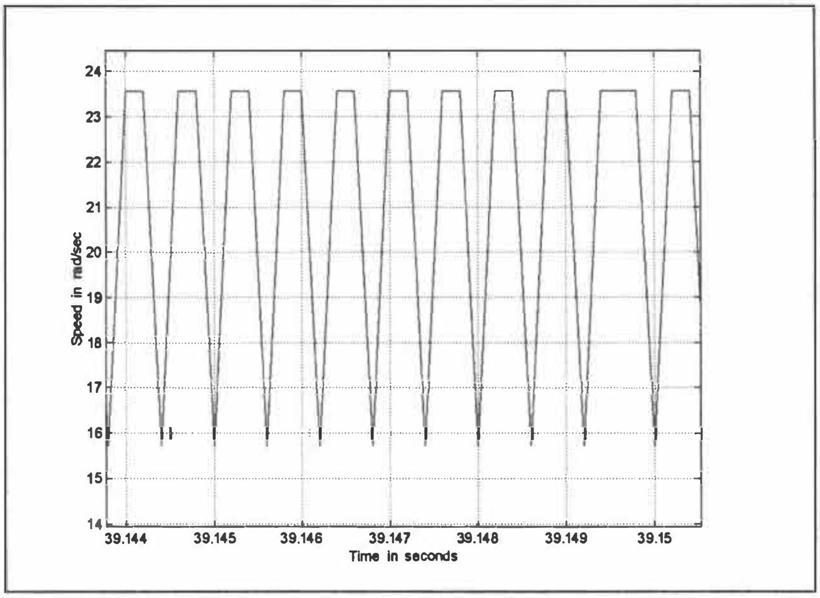

Figure 65. Zoomed view of the calculated shaft speed from the recorded position data by back differentiation (under square wave excitation)

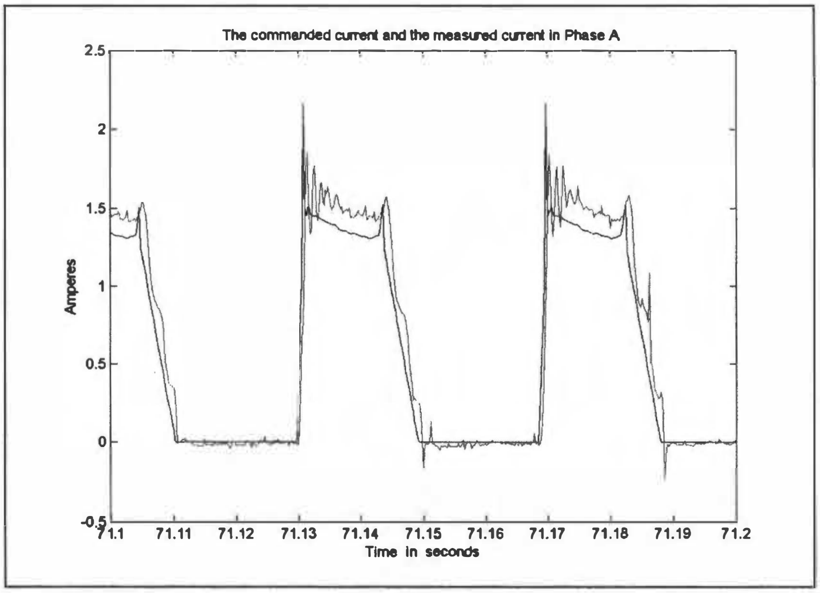

Figure 66. Reference current tracking by the reduced torque ripple controller under a constant torque command

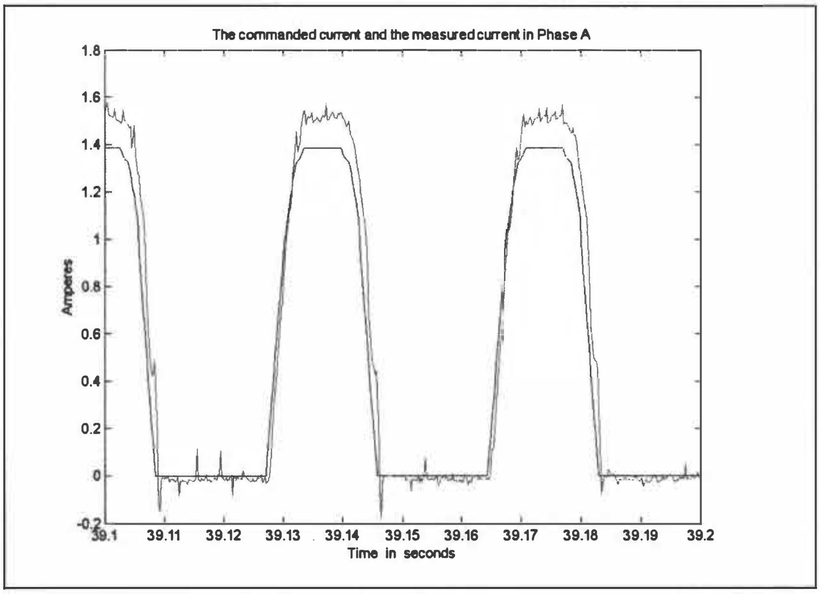

Figure 67. Reference current tracking by square wave excitation under a constant torque command

Chapter 7
Conclusion

The torque ripple of the SR motor is due to the doubly salient structure of the machine. The existence of the torque dip between two subsequent phases dictates the existence of torque ripples. Figure 68 illustrates the torque profiles of SR motors with different phase numbers as a constant current is applied. The torque dip indicated in Figure 68 implies that the higher the phase numbers, the smaller the torque dip, hence easier to minimize the torque ripple. However, even with high phase numbers, a special control method is needed to overcome the inherent torque dip in order to reduce the resulted torque ripple [2].

The idea of the control method implemented in this thesis is to define the commutation angle θ_c, at which two adjacent phases can produce the same torque for same current. Based on the defined θ_c, specific current references for commutation are designed, which is theoretically able to eliminate the torque ripple due to the torque dip. Because the control method assigns the *strong* phase to produce desired torque as much as possible, it assures low currents in phases other than the strong phase, which achieves a secondary objective of minimizing the copper losses.

The trajectory tracking performance of the implemented reduced torque ripple controller is proved by the trajectory tracking experiment described in Chapter 6. The reduced torque ripple control method shows better tracking performance compared to the simple square wave control method.

However, the torque ripple reduction of this control method is not distinct based on the results of the simulations and experiments presented in this thesis. The reason is that such a control method, like other advanced control methods, assumes good tracking of the reference currents, while the current tracking is poor in the experiments due to the capability of the amplifiers used in the experiments.

The simulation results in this thesis show that with comparatively poor current tracking, the torque ripple under the reduced torque ripple control is even higher than the simple square wave control.

In the experiments of this thesis, because of the unsatisfying current tracking, the experimental torque ripple is much higher than that of the simulations. When compared to the square wave control method in the experiments, the torque ripple reduction by using the reduced torque ripple controller is not distinct too. Only slight reduction is observed.

In the implementation of the reduced torque control method, there are several issues other than the current tracking that may degrade the actual performance of such a control method.

First, this control method leads to a reduction in the average torque. The maximum commanded torque of the strong phase must be less than a certain level which is less than the peak of the torque profile, to avoid the torque ripple due to the shape of the torque profile (see Figure 26 and 68). Therefore, the average torque under this controller has to be less than the rated average torque.

Second, the commutation method requires the phase current to built up or be extinguished quickly before or after commutation, respectively. This demands high flux derivatives, which often leads to voltage saturation at high speed. In other words, it will restrict the upper speed limit of SR motor operation.

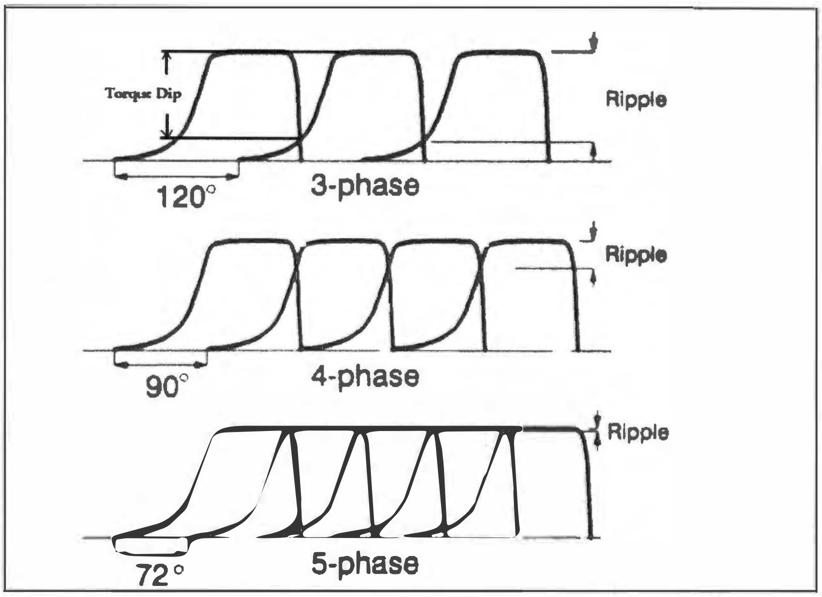

Figure 68. Illustration of the torque dip of SR motors with different phase numbers. Courtesy Magna Physics Publishing

Third, the performance of the control method depends on the accuracy of the motor model, i.e. the accuracy of the motor identification. According to [9], an inaccurate motor model may even lead to unstable response.

Forth, there are high computational requirement for this control method. For example, the step size in the experiment in this thesis can only be set as small as $200\mu s$ for the speed $\omega = 50\ rad/sec$. Smaller step size will result in overrun. Therefore, the hardware computing ability will also restrict the upper speed limit of operation.

In conclusion, the control method implemented in this thesis is theoretically appealing because it is theoretically able to eliminate the torque ripple resulted by the structure and operation method of the SR motor. However, there are several prerequisites that must be met to guarantee the performance of such a controller, in which the performance of the current tracking, the accuracy of the motor identification and the precision of the motor itself are the most important issues.

References

References

[1] Honghua Wang, *Variable Speed Control Technologies of the SR Motor*, Mechanical Engineering Publishing, China, 1999.

[2] T.J.E. Miller, *Switched Reluctance Motors and their Control*, Magna Physics Publishing, 1993.

[3] T.J.E. Miller, "Optimal design of switched reluctance motors," *IEEE Transactions on Industrial Electronics*, vol. 49, no. 1, pp. 15–26, February 2002.

[4] David A. Torrey, "Switched reluctance generator and their control," *IEEE Transactions on Industrial Electronics*, vol. 49, no. 1, pp. 3–13, February 2002.

[5] Robert B. Inderka, Marcus Menne, and Rik W.A.A. De Doncker, "Control of switched reluctance drives for electric vehicle applications," *IEEE Transactions on Industrial Electronics*, vol. 49, no. 1, pp. 48–52, February 2002.

[6] Mehrdad Ehsani and Babak Fahimi, "Elimination of position sensors in switched reluctance drives: State of the art and future trends," *IEEE Transactions on Industrial Electronics*, vol. 49, no. 1, pp. 40–46, February 2002.

[7] Chang-Hwan Kim and In-Joong Ha, "A new approach to feedback-linearizing control of variable reluctance motors for direct-drive applications," *IEEE Transactions on Control Systems Technology*, vol. 4, no. 4, pp. 348–362, July 1996.

[8] Patrick L. Chapman and Scott D. Sudhoff, "Design and precise realization of optimized current waveforms for an 8/6 switched reluctance drive," *IEEE Transactions on Power Electronics*, vol. 17, no. 1, pp. 76–83, January 2002.

[9] Iqbal Husain, "Minimization of torque ripple in srm drives," *IEEE Transactions on Industrial Electronics*, vol. 49, no. 1, pp. 28–38, February 2002.

[10] R.S. Wallace and D.G. Taylor, "A balanced commutator for switched reluctance motors to reduce torque ripple," *IEEE Transactions on Power Electronics*, vol. 7, no. 4, pp. 617–626, October 1992.

[11] T.J.E. Miller, *Electronic Control of Switched Reluctance Machines*, Newnes, 2001.

[12] B. Fahimi K.M. Rahman, G. Suresh, A.V. Rajarathnam, and M. Ehsani, "Advantages of switched reluctance motor applications to ev and hev: Design and control issues," *IEEE Transactions on Industrial Applications*, vol. 36, no. 01, pp. 111–121, Jan.-Feb. 2000.

Vita

Lu, Yinghui was born in The People's Republic of China in January, 1975. He received his Bachelor of Science degree in Electrical Engineering from Zhejiang University, China, in 1996. Upon graduation, he worked for the China Petroleum & Chemical Corporation as an electrical engineer. In August of 2000 he entered The University of Tennessee, studying toward a Master's degree in Electrical Engineering. He officially received his Master's degree in August, 2002.